Laboratory Measurements of Three-Dimensional Breaking Waves

by

Chin-Hsien Wu

B. S. National Taiwan University (1989)

M. S. National Taiwan University (1991)

Submitted to the Department of Civil and Environmental Engineering
in Partial Fulfillment of Requirements for the Degree of

Doctor of Philosophy
in Civil and Environmental Engineering

at the

Massachusetts Institute of Technology

August 1999

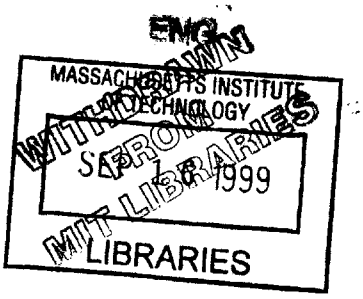

Signature of Author _____
Chin-Hsien Wu
Civil and Environmental Engineering Department

Certified by _____
Associate Professor Heidi M. Nepf
Thesis Supervisor

Accepted by _____
Daniele Veneziano
Chairman, Departmental Committee on Graduate Studies

Laboratory Measurements of Three-Dimensional Breaking Waves

by

Chin-Hsien Wu

Submitted to the Department of Civil and Environmental Engineering on August 6, 1999
in partial fulfillment of requirements for the Degree of Doctor of Philosophy
in Civil and Environmental Engineering

Abstract

Oceanic breaking waves provide an important conduit for the exchange of momentum, energy, water vapor and gases between the atmosphere and the ocean. Because ocean waves in nature are three-dimensional and their evolution is influenced by wave directionality, it is important to understand how directionality affects wave breaking. A series of laboratory experiments were designed to explore the impact of wave directionality on kinematic and dynamic processes associated with breaking. The experiments demonstrate that directionality of the waves can change the geometric breaking criterion and enhance breaking severity. In contrast, the directionality of waves does not alter the up-frequency energy transfer associated with wave steeping. In addition, the directionality of waves has little effect on the kinematic criterion. The ratio of local particle velocity and phase velocity is shown to be larger than unity at breaking. The spatially focusing and diffracting wave-packets lose 34% and 18% of their energy, respectively, as a result of plunging breakers and lost 12% and 9%, respectively, as a result of spilling breakers. Short-crested plunging breakers also produce non-uniform induced currents. The magnitude of the induced currents is $0.12C$ (where C is the characteristic phase speed) at the center and -0.01 C at the edge of breaking, and decays to $0.02C$ and -0.003C, respectively, after 30 wave periods from breaking. The induced mean flow includes strong rotational motion with lateral vorticity, f_c (characteristic central frequency), at the center and 0.3-0.4 f_c at the edge of breaking. Vertical vorticity is also produced at the flanks of the breaking crests. Turbulent kinetic energy of magnitude $2.5\times10^{-3}C^2$ is generated near the surface and penetrated to a depth of $3 \sim 4$ wave heights at the centerline of the breaker. In addition, as the short-crested breaker evolves the wake widens downstream, creating a teardrop shaped turbulent cloud. The wake volume grows as $t^{0.64}$. The dissipation rate within the three-dimensional breaking decays as $t^{-2.62}$, which is more rapid than that of two-dimensional breaking.

Thesis Advisor: Heidi M. Nepf
Title: Associate Professor of Civil and Environmental Engineering

Acknowledgments

"When you drink the water, remember the spring."

This laboratory study of three-dimensional breaking waves will not be materialized without the funding support of Office Naval Research (Contract N00014-94-1-0610) and Professor Heidi M. Nepf's NSF Career Award.

This research has been a challenge to my experimental skills and personal endurance. The final results have been greatly indebted to my advisor Professor Heidi M. Nepf for her continuous support, invaluable advice and endless patience to me, particularly during the difficult times. Besides, my gratitude goes to the committees Professor Chiang C. Mei and Dr. James B. Edson (from Woods Hole Institution) whose insightful comments and suggestions have added strength to the content throughout this work. Furthermore I often get enlightened from the constructive feedback of Professor Ole Madsen, Dr. Eric Adams, and Dr. Eugene Terray.

I am thankful for the pleasant opportunity to collaborate with Professor Todd Cowen at Cornell University whose expertise in DPIV technique has extended the depth of the analysis of the research.

To me, the unsung heroes and heroines (UROPS) of the work are Laura DePaoli, Shu-Fen Tung, Chris Resto, Ethan Fode, Robert who helped me set up the wave tank, built the horse-hair beach, cleaned up the wave basin, collected the massive amount of data days, nights and weekends. Without their sweats and dedications, I would surely have to stay for another decade to graduate.

In addition, I like to share my cheers to my friends Laura, Ben Cook and Jacquie, Paul Fricker, Roxy Liao, Chiu-On Ng, Ling Tang, Bruce Jacobs, Marco Ghisalberti, Zhu Qiang, Kirsten Findell, Kuang-An Chang, Enrique Vivoni, Richard Camilli, Hrund Andradottir, Scott Socolofsky, Gordon Ruggaber, Auroop Ganguly, Paulo Salles, Janni Moselsky-Hansen, Vicky Murphy, Sheila Frankel, and many other unnamed friends, associates and professors in Parson Laboratory. Your friendship, laughter, stories, American culture, and jokes made my life at M.I.T. unforgettable. Thank all of you for tirelessly listening to my speeches over and over again. You are all invited to the "Chin Fan Club" for your great qualification!

Outside of academic arena, I have privately benefited from my mentor Professor Lynn Gelhar and my godfather Mr. Freddie Tofu. When life is tough or when things seem confused, I have been fortunate to receive the sagacious guidance and light of hope from these two special people.

Last but not least, this thesis has been a dedication to my beloved father, mother, brother, and sister for their wholehearted supports to me all these years. Most of all, I thank my great wife Lai with all my heart for sharing this adventure day and night with me. My achievement, if any, is a product of their love.

Table of Contents

List of Figures

List of Tables

Chapter 1: Introduction

1-1 Background

Oceanic wave breaking is believed to play an important role in air-sea interaction (Banner and Peregrine 1993). It provides a significant conduit for the exchange of momentum, energy, gas and water vapor between the atmosphere and the ocean. Phillips (1977) suggested that breaking is the most important mechanism for dissipating wave energy and limiting the height of ocean waves. Breaking may be a principle mechanism for converting wind momentum flux into surface current (Longuet-Higgins 1969, Melville 1996). Currently, it is believed that breaking wave activity can enhance the near surface turbulence (Kitaigorosdkii *et al.*1983, Gargett 1989, Agrawal 1992, Terray *et al.*1996). Air entrainment, bubbles and sea sprays due to breaking waves can augment both the transfer of energy (Thorpe 1993, Melville 1994), heat (Ling 1993) and water vapor (Okuda 1982, Wallace and Wirick 1992) across the air-sea interface. Evidence has shown that breaking waves may retard global warming by increasing CO_2 fluxes to the ocean (Bryan and Spelman 1985, Csanady 1990a). For practical applications, breaking activity can be used to distinguish synthetic aperture radar images in remote sensing. (Jessup *et al.*1991a,b, Mellville 1996). The sound generated by breaking at the ocean surface can be used as a diagnostic tool in the study of acoustical oceanography (Loewen and Melville 1991a,b, Lamarre and Melville 1994). Breaking associated with freak or steep asymmetric waves can capsize ships (Greenhow and Vinje 1982, Myrhaug and Dahle 1994) and create tremendous hydrodynamic loads on offshore marine structures (Kjeldsen and Myrhaug 1979, Kjeldsen 1981, Chan 1985). In view of the many

important consequences of wave breaking, it is crucial to have a fundamental understanding of the breaking processes.

Field visual observations provide the most direct way to understand breaking waves. Breaking may occur in shallow water near the coastal zone as well as in deep water offshore. Breaking also covers a wide range of scales and intensities from violent plunging to micro-breaking (Banner and Phillips 1974). Field Observations indicate that deep water breaking is unsteady (Csanady 1990b) and intermittent (Thorpe 1992). Donelan *et al.* (1972) observed that in deep water the recurrence interval between observable whitecapping is nearly twice the wave period, suggesting that breaking occurs in wave groups. Later field observations confirmed that almost seventy percents of deep-water breaking take place within wave groups, and that the first breaker occurs slightly ahead of the center of the group (Thorpe and Humphries 1980, Holthuijsen and Herbers 1986, Tulin and Li 1992). Using a side-scan sonar, Thorpe and Hall (1983) found that the ratio of the breaking crest length to the distance of wave advance during breaking is 0.7, indicating that wave breaking is a strongly three-dimensional phenomenon. Furthermore, Su *et al.* (1984) showed photographs of bubble streamers left behind breaking events in the field and suggested that these streamers were evident for a circulation pattern produced by three-dimensional breaking.

Although field observations of deep-water breaking have provided qualitative information, little quantitative knowledge of deep-water, three-dimensional breaking has been amassed. In addition, the limited success in predicting intermittent, three-dimensional breaking (Tulin and Li 1992, Easson 1997) has been a major impediment to the development of better wind-wave and mixed-layer models applicable to the field.

Therefore, there is a need for further basic understanding of the three-dimensional breaking process before, during, and after the onset of breaking. The motivations for this study are to provide this quantitative analysis and to examine the detailed geometric evolution and kinematic and dynamic processes associated with unsteady, strongly three-dimensional breaking waves within a deep-water wave group.

1-2 Literature Review

The evolution of breaking waves can be classified into three stages. First, the pre-breaking stage is characterized by the steeping and overturning motions of the wave during which potential flow is still valid. Second, the breaking stage is characterized by the impact of the wave, the generation of splash up, and the introduction of turbulence and vorticity. Third, the post-breaking stage is characterized by turbulent energy dissipation and coherent vortical structure within the breaker wake. A summary of the theoretical, numerical, and experimental studies of breaker's evolution approaches is reviewed as below.

1-2-1 Theories

Stokes (1847) examined the weakly nonlinear effects on surface waves and made the first theoretical study of steep gravity waves. It took almost a century before the subject was extended to an investigation of nonlinear resonant interactions between surface waves (Phillips 1960, Longuet-Higgins 1962, Hasselmann 1962, Benny 1962, Longuet-Higgins and Smith 1966, McGoldrick *et al.* 1966). A subsequent contribution came from the introduction of the concept of a slowly varying wave train and the framework of averaged Lagrangian principles introduced by Whitham (1965, 1967, and

1970). It is noted that the Whitham theory requires the variations in time and space to be slow, but that there is no limitation on the cumulative amount of variations. Following Whitham's theory, it was shown that the solution of weakly nonlinear, two-dimensional and uniform deep-water waves yields a singularity for finite time, which is called a modulational instability (Lighthill 1965). The exponential growth of this modulational instability at an early time was verified experimentally by Feir (1967). Today, it is well documented as the Benjamin-Feir instability (Benjamin and Feir 1967) or Type I instability (McLean *et al.* 1981). The later stage of instability evolution doesn't lead to wave-train disintegration, but exhibits the Fermi-Pasta-Ulam recurrence (FPUR) phenomena (1955).

Effort was continuously directed toward the derivation of two-dimensional equations that are valid for longer times. The resulting equation is now well known as the cubic, nonlinear Schrödinger equation (NLS), which was first discussed in a general context by Benney and Newell (1967). For deep-water waves, the NLS equation can be derived using the multiple-scales method (Chu and Mei 1970, Davey 1972), the derivative-expansion method (Hasimoto and Ono 1972), and the Hamiltonian formulation (Zakharov 1968). To reconcile the above approaches, Yuen and Lake (1975) derived the NLS equation using Whitham theory. The NLS equation can provide quantitatively correct results of the FPUR phenomena but cannot predict the asymmetric growth of upper and lower sidebands and frequency downshift that have been observed in experiments (Lake *et al.* 1977, Melville 1982).

The modification of the NLS equation to fourth-order accuracy (NLS4) was derived by Dysthe (1979), and by Lo and Mei (1985), and later was extended to include

an empirical breaking wave term by Trulsen and Dysthe (1990). This NLS4 equation can predict the frequency downshift. However, it should be noted that the application of both the NLS equation and the NLS4 are limited by two assumptions: (1) small wave-steepness, *weakly* nonlinear waves, *i.e.* steepness $k_o a = O(\varepsilon)$ and (2) a *narrow-banded* spectrum, $\Delta k / k_o = O(\varepsilon)$: both of which are unrealistic in the field. Therefore, the nonlinear Zakharov (1968) differential-integral equation valid to broad-banded spectrum was developed. Unfortunately, the cost of the computation time for Zakharov's equation is very high. Some improvements have been undertaken to increase calculation efficiency (Krasitskii 1994). Alternatively, Truslen and Dysthe (1996) relaxed the bandwidth constraint to $\Delta k / k_o = O(\varepsilon^{1/2})$ and developed a broader-bandwidth NLS4 (BNLS4) equation that keeps the same accuracy of nonlinearity and holds the simplicity of computation.

For larger but finite values of wave steepness, $k_o a = 0.3 \sim O(\varepsilon)$, the wave trains may evolve to three-dimensional waves by Type II instability (McLean 1982). Specifically, an initial two-dimensional wave train with large wave steepness may evolve into a series of three-dimensional crescent-shape spilling breakers due to subharmonic instability (Longuet-Higgin 1978). This interesting phenomenon, observed by Su (1982) and Melville (1982), has attracted tremendous interests for the past three decades. As pointed out by Shivamoggi and Debnath (1986), the properties of the three-dimensional NLS equation (Davey and Stewartson 1974) are very different from those of the corresponding two-dimensional NLS equation. Specifically, the energy contained in the narrow banded spectrum eventually spreads out to arbitrarily high wave number modes, suggesting that the NLS equation is not adequate for the description of long time

evolution of weakly nonlinear wave packets. Lo and Mei (1987) investigated type II instability and found that the NLS4 can suppress the energy leakage. Trulsen and Dysthe (1996, 1997) used the BNLS4 to investigate frequency downshift in three-dimensional wave trains. Furthermore, to relax the constraint of small wave steepness and narrow bandwidth, the Type I and II instabilities were examined by the Zakharov equation (Crawford *et al.* 1981) and numerical computations of the fully deep-water equation (Longuet-Higgins 1978a,b, McLean 1982). Recently, Shrira *et al.* (1996) have investigated the horseshoe patterns of steady three-dimensional waves which are symmetric about the direction of wave propagation but with front-back asymmetry.

Three-dimensional short crested waves that result from the superposition of two obliquely travelling steady waves are different from the spontaneous three-dimensional waves that result from the modulated two-dimensional waves described above (Saffman and Yeun 1985). The stability of short-crested waves was investigated by Ioualalen and Kharif (1993, 1994, 1996). Generally speaking, they found that the short-crested waves are more stable than Stokes waves. The steep short-crested waves are unstable to type I instability (four wave interactions) near the two-dimensional standing wave limit, and are unstable to type II instability (five wave interactions) near the two-dimensional progressive wave limit. The fully three-dimensional waves vary smoothly between the two-limits of standing and progressive waves. These results were subsequently confirmed by Badulin *et al.* (1995) using a weakly nonlinear formulation. Recently, by improving the numerical procedures developed by Ioualaen and Kharif (1994), Kimmoun *et al.* (1999) extended weakly nonlinear waves to steeper waves, as close as possible to the maximum steepness (Roberts 1983). It should be noted that the stability problem

investigated by Kimmoun *et al.* (1999) consists of a *steady* short crested wave and small two-dimensional perturbations. More details of short-crested waves can be found in an excellent review by Dias and Kharif (1999).

So far, theories have been developed for three-dimensional *weakly* nonlinear wave evolution with broader-banded spectra. The evolving wave trains still need to *slowly* vary with time or space. In other words, the complex envelope amplitude slowly modulates compared with the associated phase function. These features of *weakly* nonlinear and *slowly* varied wave evolution are distinctly different from the *strongly* nonlinear and *rapidly* varied wave evolution associated with wave breaking.

1-2-2 Numerical Simulations

Numerical simulations of the pre-breaking stage for strongly nonlinear, unsteady, two-dimensional deep water waves were first performed by Longuet-Higgins and Cokelet (1976) and Dold and Peregrine (1986) using the boundary integral method based on potential flow. More efficient and robust numerical codes were later developed to verify the potential flow results through comparison with experiments (Dommermuth *et al.* 1987, Wang *et al.* 1993, and Skyner 1996). Recently, numerical simulations of the entire two-dimensional breaking process, through the breaking and post-breaking periods, were achieved by Lin and Liu (1998) using the $k-\varepsilon$ turbulent model, and by Chen *et al.* (1999) using the Navier-Stokes equations.

As to three-dimensional breaking waves, numerical descriptions of breaking onset are now feasible (Xü and Yue 1992, Miyata *et al.* 1996), but the full computations of strongly nonlinear, viscous, three-dimensional, breaker evolution remain a challenging

task (Tsai and Yue 1996). Thus, coherent vortical structures, the cascade to smaller scales, and energy dissipation for three-dimensional wave breaking are important issues that must still be addressed through physical experiments.

1-2-3 Experiments

To perform a well-controlled experiment in a laboratory wave flume or wide basin, it is crucial to understand the wave breaking mechanisms. In general, breaking may result from (1) intrinsic instability, (2) wave shoaling, (3) constructive interference, (4) direct wind forcing, or (5) wave-current interaction. The literature survey of the study of deep-water breaking through experimental approaches is listed in Table 1.1.

For the intrinsic instability, Melville (1982) and Su *at al.* (1982, 1984) showed that the two-dimensional Benjamin-Feir (type I) instability and the three-dimensional (type II) instability may occur in the laboratory for different ranges of wave steepness. From the application viewpoint, these results are useful for comparison with the theories, but the focus on narrow-banded spectral wavetrains may be too restrictive for comparison to real ocean conditions. To examine wave shoaling, a steady spilling breaker has been generated by towing a hydrofoil in a wave tank (Ducan 1981, 1983). However, the breaking we see in the open ocean is unsteady so that the extrapolation from steady conditions may be limited. In view of this, Van Dorn and Pazan (1975) and Ramberg (1987) used a convergent channel to generate unsteady breaking waves by spatially constructive interference. It was found that multiple breaking events continuously occurred throughout the measurement interval and energy/momentum loss rarely reached stable value. This method cannot generate a repeatable and isolated breaker, making

quantitative analysis difficult. The temporally constructive interference proposed by Longuet-Higgins (1974) and Rapp and Melville (1990) can be used to generate a very repeatable, unsteady breaking wave. Wave-current interaction (Longuet-Higgins and Stewart 1964, Skyner *et al.* 1998) is a limiting case of constructive interference and deserves an independent study. Although wind forcing (Banner and Melville 1976) appears to play a role in provoking breaking in the field, it is difficult to bring this field condition back to laboratories. Moreover, if the time-scale for overturning the sea surface is short compared to the time scale of energy input by wind or the momentum flux from the wind in one wavelength is less than the flux carried by the waves, then wind forcing is not the main mechanism causing wave breaking (Longuet-Higgins 1988). The previous studies descried above lead us to the temporally constructive interference, which is believed to be the single most important cause of breaking near the peak of the wind-wave spectrum (Rapp and Melville 1990).

Table 1.1 shows the geometric, kinematic, and dynamic properties of deep- water wave breaking investigated by many researchers. Specifically, breaking wave criteria, momentum/energy losses, induced current, vorticity, turbulence, and mixing are listed. Although three-dimensional breaking wave criteria have been investigated by She *et al.* (1994, 1997) and Kolaini and Tulin (1995), as far as we are aware, no detailed investigations of unsteady, strongly three-dimensional and short-crested breaking waves in the laboratory have been made. These important issues include:

(1) How does the wave directionality influence *unsteady* three-dimensional wave breaking?

(2) What are the energy/momentum losses associated with three-dimensional breaking?

(3) What is the magnitude of the currents generated by three-dimensional breaking?

(4) Does three-dimensional breaking generate the vertical vorticity as conjectured by theories?

(5) What are the turbulent mixing characteristics of three-dimensional breaking waves?

(6) What is the dissipation rate in the three-dimensional breaking wake?

1-3 Thesis Outlines

The objectives of this study are to provide detailed measurements and address the above six issues. These measurements include surface displacements, velocity, and mixing rate for three-dimensional breaking waves. In this dissertation, the breaking wave criteria and energy losses are addressed in Chapter 2 using the surface displacement measurements. In Chapter 3, the induced currents and vorticity generated by a three-dimensional plunging breaker are described using ensemble averaging of the detailed velocity measurements. In Chapter 4, turbulence, mixing, and dissipation rate due to three-dimensional breaking wakes are presented. The dissertation closes with Chapter 5, a summary of the results and suggestions for future work.

In Appendix A, the importance of wave directionality is shown by a comparison of the two- and three-dimensional wave breaking (Nepf *et al.* 1998).

1.4 References

Agrawal, Y.C., Terray, E.A., Donelan, P.A., Hwang, A.J., and Williams, W.M., Drennan, K.K. Kahma and Kitaigorodskii, S.A., "Enhanced dissipation of kinetic energy beneath surface waves," *Nature*, **359**, pp. 219-220, 1992.

Banner, M. L. and Phillips, O. M., "On the incipient breaking of small scale waves," *J. Fluid Mech*, **65**, pp. 647-656, 1974.

Banner, M. L. and Melville, W. K., "On the separation of air flow over water waves," *J. Fluid Mech.*, **77**, pp. 825-842, 1976.

Banner, M. L. and Peregrine, W. K., "Wave breaking in deep water," *Annu. Rev. Fluid Mech.*, **25**, pp.373-379, 1993.

Badulin, Shrira, V., Kharif, C., Ioualalen M., "On two approaches to the problem of instability of short-crested water waves," *J. Fluid Mech.*, **303**, pp. 297-326, 1995.

Benjamin, T.B. and Feir, J.E., "The disintegration of wavetrains in deep water, part I," *J. Fluid Mech.*, **27**, pp. 417-430, 1967.

Benny, D. T., "Nonlinear gravity waves interaction," *J. Fluid Mech.*, **14**, pp. 577-584, 1962.

Benny, D. J. and Newell, A. C., "The propagation of nonlinear wave envelope," *J. Math Phys.*, **46**, pp. 133-139, 1967.

Bonmarin, P.J., "geometric properties of deep water breaking waves," *J. Fluid Mech.*, **209**, pp. 405-433, 1989.

Bryan K. and Spelman M.J., "The ocean's response to a CO_2-induced warming," *J. Geoph. Res.*, **90** (C6) , pp. 11678-11688, 1985.

Chan, E.S., *Deep water breaking wave forces on structure*, Sc.D. thesis, Massachusettss Institute of Technology, 1985.

Chen, G., Kharif, C., Zaleski, S., and Li J., "Two-dimensional Navier-Stokes simulation of breaking waves," *Phys. Fluid,* **11 (1)**, pp. 121-133, 1999.

Chu, V.H. and Mei, C. C., "On slowly varying Stokes waves," *J. Fluid Mech.*, **41**, pp. 873-887, 1970.

Conite, R. and Tulin, M. P., "A theory of steady breaker," *J. Fluid Mech.*, **276**, pp. 1-20, 1994.

Crawford, D.K., Lake, B. M., Saffman, P.G., and Yuen, H.C., "Stability of weakly nonlinear deep-water waves in two and three dimensions," *J. Fluid Mech.*, **105**, pp. 177-191, 1981.

Csanady G.T., " The role of breaking wavelets in air-sea gas transfer," *J. Geoph. Res.*, **95** (C1), pp. 749-759, 1990a.

Csanady G.T., " Momentum flux in breaking wavelets," *J. Geoph. Res.*, **95** (C8) pp. 13289-13299, 1990b.

Davey, A., " The propagation of weak nonlienar waves," *J. Fluid Mech.*, **53,** pp. 769-781, 1972.

Davey, A. and Stewartson, K., "On the three-dimensioal packets of surface waves," *Proc. E. Soc. London,* **A 338,** pp. 101-110, 1974.

Dias, F. and Kharif, C, "Nonlinear gravity and capillary-gravity waves," *Annu. Rev. Fluid Mech.*, **31**, pp. 301-346, 1999.

Dold, J.W. and Peregrine, D. H., "Water Wave Modulation," *Proc. 20th Intl. Conf. Coastal Engng.*, Taipei, **1**, pp. 163-175, ASCE.

Dommermuth, D. G., Yu, D. K. P, Rapp, R. J. Chan, F. S. and Melville, W. K., "Deep water breaking waves: a comparison between potential theory and experiments," *J. Fluid Mech.*, **89**, pp. 432-442, 1987.

Donelan, M.A., Longuet-Higgins, M.S., and Turner J.S., "Periodicity in whitecaps," *Nature*, **239**, pp 449-451, 1972.

Duncan, J. H. (1981), "An experimental investigation of breaking waves produced by a towed hydrofoil," *Proc. R Soc. London*, **A377**, pp. 331-348, 1981.

Duncan, J. H. (1983), "The breaking and non-breaking wave resistance of a two-dimensional hydrofoil," *J. Fluid Mech.*, **126**, pp. 507-520, 1983.

Duncan, J.H., Philomin, V., Behres, M., and Kimmel, J., "The formation of spilling breaking water waves," *Phys Fluid*, **6**, pp. 2558-2560, 1994.

Dysthe. K. B. (1979), "Note of a modification to nonlinear Schödinger equation for application to deep water waves," *Proc. R Soc. London.*, **A369**, pp. 105-114, 1979.

Easson, W. J., "Breaking waves," *Offshore Technology Report*, OTO-96-035, 1997.

Feir J. E., (1967), "Discussion: Some result from wave pulse experiments," *Proc. R Soc. London*, **A299**, pp. 54-58, 1967.

Fermi, E., Pasta., J., and Ulam., S., "Studies of nonlinear problem I," Los Alamos Report LA 1940, Lectures in Applied Mathematics, (Ed. A. C. Newell), *Amer. Math Soc.* (1974), **15**, pp. 143-156, 1955.

Gargett, A., "Ocean turbulenece," *Annu. Rev. Fluid Mech.,* **20**, pp 12-485, 1989.

Greenhow, M. and Vinje T., "A theoretical and experimental study of the capsize of Salter's duck in extreme waves," *J. Fluid Mech.*, **118**, pp. 221-239, 1982.

Hasimoto, H. and Ona, H., "Nonlinear modulation of gravity waves," *J. Physical Soc. Japan*, **33**, pp. 805, 1972.

Hasselmann K. (1962), "On the nonlinear energy transfer in a gravity wave spectrum, Part I: General Theory," *J. Fluid Mech.*, **12,** pp. 481-500, 1962.

Holthuijsen L.H. and Herbers T.H.C., "Statistics of breaking waves observed as whitecaps in the open sea," *J. Phys. Oceanogr.,* **16,** pp. 290-297, 1986.

Ioualalen, M. and Kharif, C, "Stability of three-dimensional progressive gravity waves on deep water to subharmonic disturbances," *Eur. J. Mech., B/Fluids*, **12,** pp. 401-414, 1993.

Ioualalen, M. and Kharif, C, "Stability of subharmonic instabilities of steady three-dimensional deep water waves," *J. Fluid Mech.*, **262,** pp. 265-291, 1994.

Ioualalen, M. and Kharif, C, "On the observability of finite-depth short-crested water waves," *J. Fluid Mech.*, **322,** pp. 1-19, 1996.

Jessup, A. T., Melville, W.K., Keller, W.C., "Breaking waves affecting microwave backscatter 1.Detection and verification," *J. Geoph. Res.,* **96**, pp 20547-20559, 1991a.

Jessup, A. T., Keller, W. C., Melville, W. K. "Breaking waves affecting microwave backscatter 2.Dependence on wind and wave conditions," *J. Geoph. Res,* **96**, pp 20561-20569, 1991b.

Kimmoun O, Ioualalen, M. and Kharif, C, "Instabilities of steep short-crested surface waves in deep water," *Phys. Fluid,* **11(6)**, pp. 1679-1681, 1999.

Kitaigorosdkii, S.A., Donelan, M.A., Lumley, J.L.,Terray, E.A., "Wave turbulence interactions in the upper ocean (II)," *J. Phys. Oceanogr.,* **13,** pp. 1988-1999, 1983.

Kjeldsen, S.P., "Shock pressure from deep water breaking waves," *Proc. Int. Symp. on Hydrodyn.*, Trondheim, pp. 567-584, 1981.

Kjeldsen, S.P., and Myrhaug, D., "Breaking waves in deepwater and resultant wave forces," *Proc. 11th Offshore Technology Conf.*, Houston, Texas, Paper 3646, 1979.

Kjeldsen, S.P., and Myrhaug, D., "Whitecapping and wave crest lengths in directional seas," *Symp. on Description and Modeling of Directional Seas*, Danish Hydraulics Inst., Paper B, **6**, 1984.

Kolaini, A. and M. Tulin, "Laboratory measurements of breaking inception and post-breaking dynamics of steep short-crested waves," *Int. J. of Offshore and Polar Engng.*, **5**, pp. 212-218, 1995.

Krasitskii, V. P., "On the reduced equations in the Hamiltonian theory of weakly nonlinear surface waves," *J. Fluid Mech.*, **272,** pp. 1-20, 1994.

Lake, B. M., Yuen, H. C., Rundgaldier, H., and Ferguson, W. E., "Nonlinear deep water waves: theory and experiment, Part 2, evolution of a continuous wave train," *J. Fluid Mech.*, **83,** pp. 49-74, 1977.

Lamarre, E. and Melville, W.K., "Void-fraction measurements and sound speed fields in bubble plumes generated by breaking waves," *J. Acous. Soc. Am.*, **95**, pp. 1317-1328, 1994.

Lighthill M. J., "Contribution to the theory of waves in nonlinear dispersive system," *J. Inst. Math Appl.*, **2**, pp269-306, 1965.

Lin, P. and Liu, P. L.-F., "A numerical study of breaking waves in the surf zone," *J. Fluid Mech.*, **359**, pp. 239-264, 1998.

Lin, J.C. Rockwell, D., "Instantaneous structure of a breaking wave," *Phys. Fluids*, **6**, pp. 287-2879, 1994.

Lin, J.C. Rockwell, D., "Evolution of a quasi-steady breaking waves," *J. Fluid Mech.*, **302,** pp. 29-44, 1995.

Ling, C. S., "Effect of breaking waves on the transport of heat and vapor fluxes from the ocean," *J. Phys. Oceanogr.*, **23,** pp. 2360-2372, 1993.

Lo. E. and Mei., C. C., "A numerical study of water-wave modulation based upon a higher-order nonlinear Schrödinger equation," *J. Fluid Mech.*, **150**, pp. 395-416, 1985.

Lo. E. and Mei. C. C., "Slow evolution of nonlinear deep water waves in two horizontal directions: a numerical study," *Wave Motion*, **9**, pp.245-259, 1987.

Loewen, M. R. and Melville, W. K., "Microwave backsactter and acoustic radiation from breaking waves," *J. Fluid Mech.*, **224**, pp. 601-623, 1991a.

Loewen, M. R. and Melville, W.K., "A model of the sound generated by breaking waves," *J. Acous. Soc.*, **90**, pp 2075-2080, 1991b.

Longuet-Higgins, M. S., "Resonant interaction between two trains of gravity waves," *J. Fluid Mech.*, **12,** pp. 321-332, 1962.

Longuet-Higgins, M. S., "On wave breaking and equilibrium spectrum of wind generated waves," *Proc. R. Soc. London*, **A310**, pp. 151-159, 1969.

Longuet-Higgins, M. S., "Breaking waves in deep and shallow water," *Proc. 10th Conf. in Naval Hydrodyna.*, pp. 597-605, 1974.

Longuet-Higgins, M. S., "The stability of gravity waves of finite-amplitude in deep water I, Superharmonics," *Proc. R. Soc. London,* **A360,** pp 471-488, 1978a.

Longuet-Higgins, M. S., "The stability of gravity waves of finite-amplitude in deep water I, Subharmonics," *Proc. R. Soc. London,* **A360,** pp 489-505, 1978b.

Longuet-Higgins, M. S., "Mechanics of waves in deep water," in *Sea Surface Sound-Nature Mechanisms of Surface Generated Noise in the Ocean*, edited by Kerman, B.R., (Dordrecht: Kluwer), pp. 1-30, 1988.

Longuet-Higgins, M. S. and Smith, N. D., "An experiment on third order resonant waves interaction," *J. Fluid Mech.*, **25**, pp. 417-435, 1964.

Longuet-Higgins, M. S. and Stewart, R. W., "Radiation stress in water waves, a physical discussion with application," *Deep Sea Res.*, **11**, pp.529-562, 1964.

Longuet-Higgins, M. S. and Cokelet, E. D., "The deformation of steep surface wave in water. I. A numerical method for computation," *Phil. Trans. R. Soc. London,* **A358**, pp. 1-26, 1976.

McGoldrick, L. F., Phillips, O. M., Huang, N. and Hodgson T., "Measurement on resonant interaction," *J. Fluid Mech.*, **25**, pp. 437-456, 1966.

McLean, J. W., Ma, Y.C., and Martin, D.U., Saffman, P.G., and Yuen, H.C., "Three-dimensional instability of finite-amplitude water waves," *Phys. Rev. Lett.*, **115**, pp. 817-820, 1981.

McLean, J. W., "Instabilities of finite-amplitude water waves," *J. Fluid Mech.*, **114**, pp. 315-330, 1982.

Melville, W. K., " The instability and breaking of deep-water waves," *J. Fluid Mech.*, **115**, pp. 165-185, 1982.

Melville, W. K., " Wave modulation and breakdown," *J. Fluid Mech.*, **128**, pp. 489-506, 1983.

Melville W. K., " Energy dissipation by breaking waves," *J. Phys. Oceanogr*, **24**, pp 2041-2049, 1994.

Melville W. K., "The role of surface wave breaking in air-sea interaction," *Annu. Rev. Fluid Mech.*, **28**, pp. 279-321, 1996.

Melville, W. K. and Rapp R.J., "Momentum Flux in Breaking Waves," *Nature*, **317**, pp. 514-516, 1985.

Miller, M., Nennstiel, T., Duncan, J.H., Dimas, A., and Prostler S., "Incipient breaking of steady waves in the presence of surface wakes," *J. Fluid Mech.*, **383**, pp. 285-305, 1999

Miyata, H, Kanai, A., Kawamura T. and Park, J.-C., "Numerical simulation of three-dimensional breaking waves," *J. Marine Sci. and Tech.*, **1**, pp183-197, 1996.

Myrhaug and Dahle, " Ship capsize in breaking waves,"*Fluid Structure Interaction in Offshore Engng.*, edited by Chakrabarti (Comp. Mechanics Publications, pp. 44-84, 1994.

Nepf, H. M., Wu, C. H. and Chan, E. S., "A comparison of two- and three-dimensional wave breaking," *J. Phys. Oceanogr.*, **28**, pp.1496-1510, 1998.

Okuda, K., "Internal flow structure of short wind waves, on the internal vorticity structure," *J. of Oceanogr. Soc. Japan*, **38**, pp. 28-42, 1982.

Perlin, M., Bernal, L. and He, J., "Vorticity generation and energy dissipation in transient breaking waves progress toward a deep-water breaking wave criteria," *ONR Conference Free Surface Turbulence,* Pasadena. 1995.

Perlin, M., He, J. and Bernal, L. P., "An experimental study of deep water plunging breaker," *Phys. Fluid,* **8**, pp. 2365-2374, 1996.

Phillip, O. M., "On the Dynamics of unsteady gravity waves of finite amplitude, Part 1," *J. Fluid Mech.*, **9**, pp. 193-217, 1960.

Phillip, O. M., *The dynamics of upper ocean*, Cambridge University Press, 336 pp. 2nd ed., 1977.

Ramberg, S. E. and Griffin, Owen M., "Laboratory study of steep and breaking deep water waves," *J. of Waterway, Port, Coastal, and Ocean Engng.*, **113**, pp. 493-507, 1987.

Rapp, R. J., *Laboratory measurements of deep water breaking waves*, Ph.D. thesis, Massachusetts of Institute of Technology, USA, 1986.

Rapp, R. J. and Melville, W. K., "Laboratory measurement of deep water breaking waves," *Phil. Trans. R. Soc. London*, **A442**, pp. 735-800, 1990.

Robert, A. J., "Highly nonlinear short-crested water waves," *J. Fluid Mech.*, **135**, pp. 301-321, 1983.

Saffman, P. G. and Yuen H.C., "Three-dimensional waves on deep water," in Advances in Nonlinear Waves, edited by Debnath, L., **111**, London: Pitman, pp. 1-30, 1985.

She, K., Greated, C. A., and Easson W. J. "Experimental study of three-dimensional wave breaking," *J. of Waterway, Port, Coastal, and Ocean Engng.*, **120 (1)**, pp. 20-36, 1994.

She, K., C. A. Created, and W. J. Easson, "Experimental study of three-dimensional breaking waves kinematics," *Applied Ocean Res.* **19**, pp. 329-324, 1997.

Shivamoggi, B. K. and Debnath, L., "Three-dimensional nonlinear Schrödinger equation for finite-amplitude gravity fluid in a fluid," *Il Nuovo Cimento,* **94B**, pp. 140-148, 1986.

Shrira, V. I., Badulin, S. I., and Kharif, C., "A model of water wave 'horse-shoe' patterns," *J. Fluid Mech.*, **318**, pp. 375-404, 1996.

Skyner, D. J., "A comparison of numerical predictions and experimental measurements of internal kinematics of a deep-water plunging wave," *J. Fluid Mech.*, **315**, pp. 51-64, 1996.

Skyner, D. J. and Easson, W. J., "Wave kinematics and surface parameters on steep waves traveling on sheared currents," *J. of Waterway, Port, Coastal, and Ocean Engng.*, **124 (1)**, pp. 1-6, 1998.

Stokes, G. G., "On the theory of oscillatory waves," *Trans. Camb. Phil. Soc. Trans.*, **8**, pp441-455, 1847.

Su, M. Y., "Three-dimensional deep water-waves, Part I. Experimental measurement of skew and symmetric wave pattern," *J. Fluid Mech.*, **124**, pp. 73-108, 1982.

Su, M. Y., Bergin, M.T., Marler, P., Myrick, R., "Experiment on nonlinear instabilities and evolution of steep-gravity trains," *J. Fluid Mech.*, Vol. 124. pp 45-72, 1982.

Su, M. Y., Green A.W. and Bergin M.T., "Experimental studies of surface wave breaking and air entrainment," *Gas Transfer at Water Surface*, edited by Brutseart W. and Jirka G.K., editors, Reidel D., Publishing Company, Dordrecht, pp 211-219, 1984.

Terray A. M., Agrawal, Y.C., Drennan, W.M., Kahma, K.K., Williams, A.J., "Esitmates of kinetic energy dissipation under breaking waves," *J. Phys.Oceanogr.*, **262,** pp. 792-807, 1996.

Thorpe, S. A., "Bubble clouds and the dynamics of the upper ocean," *Quarterly J. of Royal Metereologial Soc.*, **118**, pp 1-22, 1992.

Thorpe, S. A., "Energy loss by breaking waves," *J. Phys. Oceanogr.*, **23**, pp. 2498-2502, 1993.

Thorpe, S. A. and Humphries, P. N., "Bubbles and breaking waves," *Nature*, **283**, pp. 463-465, 1980.

Thorpe, S. A. and Hall A. J., " The characteristics of bubble clouds, breaking waves and near surface currents observed using side-scan sonar," *Continental Shelf Res.*, **1**, pp. 353-384, 1983.

Trulsen, K. and Dysthe, K. B., "Action of windstress and breaking on the evolution of a wave-train," in *Breaking Waves*, edited by Banner, ML and Grinshaw, R.H. J, Springer-Verlag, pp. 243-249, 1990.

Trulsen, K. and Dysthe, K. B., "A modified nonlinear Schrödinger equation for broader bandwidth gravity waves on deep water, " *Wave Motion*, **24**, pp. 281-289, 1996.

Trulsen, K. and Dysthe, K. B., "Frequency downshift in three-dimensional wave trains," *J. Fluid Mech.*, **352**, pp. 359-373, 1997

Tsai, W. T. and Yue, D. K. P., "Computation of nonlinear free-surface flows," *Annu. Rev. Fluid Mech.*, **28**, pp.249-278, 1996.

Tulin, M. P. and Li, J. J., "On the breaking of energetic waves," *Int. J. of Offshore and Polar Engng.*, **2 (1)**, pp. 46-53, 1992.

Tulin, M. P. and Waseda, "Laboratory observations of wave group evolution, including breaking effects," *J. Fluid Mech.*, **378**, pp. 197-232, 1999.

Van Dorn, W. G. and Pazan, S. E. (1975), "Laboratory investigation of wave breaking," Scripps Inst. of Ocean Report, **75-21**, AOEL Rep. No. 71, 1975.

Wallace, D.W.R. and Wirick, C. D., "Large air-sea gas flux associated with breaking waves," *Nature*, **356**, pp 694-696, 1992.

Wang, P., Yao Y., and Tulin, M. P., "Wave groups, wave-wave interaction and wave breaking, result of numerical experiments," *Proc. of 3rd Int. Offshore and Polar Engng,, III*, pp. 27-33, Singapore, 1993.

Whitham G. B., "A note on group velocity," *J. Fluid Mech.*, **9**, pp. 347-352, 1960.

Whitham G. B., "Mass, momentum and energy flux in water waves," *J. Fluid Mech.*, **12**, pp. 135-147, 1962.

Whitham G. B.,"A general approach to linear and nonlinear dispersive waves using a Lagrangian," *J. Fluid Mech.*, **22**, pp. 273-283, 1965.

Xü H., and Yue, D.K.P., "Computations of fully nonlinear three-dimensional water waves," *Proc.19th Symp.on Naval Hydrodyn.*, Seoul, Korea, pp. 177-201, 1992.

Yuen, H. C. and Lake, B. M., "Nonlinear deep water waves: theory and experiment," *Phys Fluids*, **18**, pp. 956-960, 1975.

Zakharov, V. E., "Stability of periodic wave of finite amplitude on the surface of a deep fluid," *Zh. Prilk. Mekh. Fiz.*, Vol. 9, pp. 86, 1968.

Table 1.1. The literature survey of the study of deep-water wave breaking through experimental approaches.

Author	Dimension Types	Breaking Wave Mechanism	Breaking Criteria	Energy Loss	Induced Current	Vorticity	Generated Turbulence	Mixing	Others
Benjamin and Feir (1967)	2D evolution	intrinsic instability							growth rate
Lake *et al.* (1977)	2D evolution	intrinsic instability							growth rate, frequency downshift
Melville (1982,1983, 1988)	2D evolution spiller	intrinsic instability	ak<0.29 2D ak>0.32 3D kinematic U/C						growing continuous spectrum
Su (1982) Su *et al.* (1984)	2D and 3D evolution spiller	intrinsic instability	skew 0.16< ak < 0.18 symmetric 0.25<ak<0.34						
Tulin and Waseda (1999)	2D evolution spiller, plunger	intrinsic instability	ak<0.1 2D						growth rate, frequency downshift
Ducan(1981, 1983), Ducan &Dimas (1996) Miller *et al.* (1999)	2D steady spiller	wave shoaling	H/L=0.1 larger steepnes				Dissipation Drag Stress		crest profile drift flow effect
Battjes and Sakai (1981)	2D steady spiller	wave shoaling				vorticity generation (velocity)			
Lin and rockwell (1994,1995)	2D steady spiller	wave shoaling				Shear layer + vorticity (PIV)			
Dabiri and Gharib (1997)		Honeycome pressure drop				Shear layer + vorticity (PIV)			

Author	Dimension Types	Breaking Wave Mechanism	Breaking Criteria	Energy Loss	Induced Current	Vorticity	Generated Turbulence	Mixing	Others
Van Dorn / Pazan (1975) Ramberge *et al.* (1987)	2D unsteady spiller, plunger	spatially constructive interference	(H/L)ave= 0.11 ak=0.31-0.38 ak=0.33-0.38	twice the result of Melville's					
Bliven (1984)	2D	wind wave spectrum (irregular waves)					Reynolds stress (velocity)		
Cheung *et al* (1988)	2D	wind + wind wave spectrum (irregular waves)			wave affect veloicty mean		eviden ce ripple and tubulence		
Banner, and Melville (1976)	2D	wind wave	mechanism of breaking waves						flow separtion
Bonmarin (1989)	2D spiller, plunger	intrinsic instability *temporally constructive interference	(H/L)=0.016 parameters vary						
Rapp and Melville (1985,1990)	2D unsteady incipient spiller plunger	temporally constructive interference constant a	(ak)in=0.25 (ak)in=0.30 (ak)in=0.39	dS/So= 0.05-0.10 0.18-0.25 0.25-0.30	0.02-.03C after 60T, 0.005C		90%Energy is lost during 4T		wideband spectrum
Duncan *et al* (1994)	2D parasite spiller	temporally constructive interference -- constant a and envelope				find the onset of breaking			
Perlin *et al.* (1995, 1996) (LIF)	2D incipient spiller plunger	*intrinsic instabilities *temporally constructive interference	breaking criteria			find the onset of breaking	energy		
Lamarre and Melville (1993,1994)	3D incipient spiller plunger	temporally constructive interference -- constant ak							bubbles acoustic

Author	Dimension Types	Breaking Wave Mechanism	Breaking Criteria	Energy Loss	Induced Current	Vorticity	Generated Turbulence	Mixing	Others
Lowen and Melville (1991,1994)	3D incipient spiller plunger	temporally constructive interference -- constant ak							acoustic
She *et al.* (1994,1997)	3D	constructive interference	geometric and kinematic criteria						Frequency Spectrum
Kolaini and Tulin (1995)	3D	spatial modulation	higher breaking steepness						

Submitted to Journal of Geophysical Research
April 16, 1999

Chapter 2: Breaking Criteria and Energy Losses for Three Dimensional Wave Breaking

Chin H. Wu and H. M. Nepf

Abstract. Laboratory experiments were used to explore the influence of spatial focusing and diffraction on the evolution of unsteady, three-dimensional, deep-water wave-packets with a constant-steepness spectrum. The wave-packets were generated by thirteen independently programmed paddles and evolved to breaking near the midpoint of a 4m x 11m test section. Detailed measurements of surface displacements were made across the entire test section and used to examine energy losses and breaking criteria. Three forms of breaking criteria were considered: (1) geometric criteria based on local and global wave steepness, (2) a kinematic criterion based on particle and phase velocities, and (3) a dynamic criterion based on higher harmonic energy evolution. The results indicate that directionality of the waves can either increase (focusing waves) or decrease (diffracting waves) the geometric breaking criterion as well as breaking severity. In contrast, the directionality of waves did not alter the up-frequency energy transfer associated with wave steepening. In addition, the directionality of waves had little effect on the kinematic criterion. At breaking, the ratio of local particle velocity and phase velocity was shown to be larger than unity for both focusing and diffracting waves. Indeed, the robustness and simplicity of the kinematic criterion make it an excellent choice for field application. The three-dimensional, spatially focusing and diffracting wave-packets lost 34% and 18% of their energy, respectively, as a result of plunging breakers and lost 12% and 9%, respectively, as a result of spilling breakers. Comparable two-dimensional breakers with the same spectral shape lost 16 % for plunging and 12% for spilling.

2.1 Introduction

Breaking waves are universally present over the ocean surface and play an important role in the exchange of gas, water vapor, momentum, and energy between the atmosphere and the ocean (*e.g.* Kerman, 1988, Melville 1996). These exchanges affect the growth of wind waves, the generation of sea sprays and bubbles, the formation of surface currents, and the distribution of near-surface turbulence (Longuet-Higgins 1969). The significance and study of wave breaking are excellently reviewed in Peregrine (1983), Banner and Peregrine (1993), Thorpe (1995), Melville (1996), and Longuet-Higgins (1996). In view of the many important consequences of wave breaking, it is crucial to have a fundamental understanding of the breaking processes, in particular, to be able to predict the onset of breaking and its energy losses. While we have gained significant insight into the breaking process from two-dimensional laboratory experiments (Benjamin and Feir 1967, Kjeldsen and Myrhaug 1980, Duncan 1981, Bonmarine 1989, Rapp and Melville 1990, Baldock *et al.* 1996, Kway *et al.* 1998), ultimately we must consider directionality to understand the process of breaking in the ocean, which is fully three-dimensional (Thorpe 1995, Peregrine 1998). The primary purpose of this paper is to explore the effects of wave directionality (spatial focusing and diffraction) on three-dimensional breaking wave criteria and energy losses. Through comparison to other studies, the effects of spectral shape are also discussed.

Many criteria have been proposed to predict the onset of wave breaking. Generally, they can be classified into three categories: (1) geometric criteria based on local wave shape (Kjeldsen and Myrhaug 1980) and global wave steepness (Rapp and Melville 1990); (2) kinematic criteria based on particle and phase velocities (Longuet-

Higgins 1969); and (3) dynamic criteria based on acceleration at the crest (Longuet-Higgins 1969), momentum and energy growth rate (Banner and Tian 1998), and higher harmonic energy evolution (Rapp and Melville 1990, Kway *et al.* 1998). A detailed review of these breaking criteria can be found in Tulin and Li (1992), Easson (1997), and Nepf *et al.* (1998).

A handful of laboratory experiments have already pointed to the influence of wave dimensionality on the evolution and onset of breaking. Through instability two-dimensional wave crests with initial steepness greater than 0.31 have been shown to evolve into three-dimensional crests which eventually begin to spill (Su 1982, Su et al. 1982, and Melville 1982). For steady, short-crested, monochromatic waves, Kolaini and Tulin (1995) suggested that three-dimensional effects can elevate the wave steepness of breaking. In addition, unsteady, short-crested breaking has also been shown to be influenced by directionality, with higher breaking steepnesses and greater breaking severity observed for spatially focusing waves (She *et al.* 1994, 1997) than for diffracting waves (Nepf *et al.* 1998). In this paper, we expand on these results by assessing the sensitivity of multiple breaking criteria to wave directionality. We find that the geometric criteria are strongly affected by both directionality and spectral shape. In contrast, the kinematic and dynamic criteria appear insensitive to both directionality and spectral shape. Finally, the kinematic criterion is shown to be the most robust and the most promising criteria for field applications.

The loss of wave energy due to breaking is a source of energy for turbulent mixing and air entrainment, which can enhance air-sea gas and heat transfer (Jessup *et al.* 1997). Most laboratory studies for energy loss are limited to two-dimensional waves, *e.g.*

quasi-steady breaking (Duncan 1981,1983) and unsteady breaking (Rapp and Melville 1990) with the estimated energy loss ranging from 10% for a spilling breaker to 25% for a plunging breaker. These laboratory results have been used to estimate the energy dissipation for wave breaking in the field (Thorpe 1993, Melville 1994). Recently, Kway *et al.* (1998) observed that the breaking losses increase as the spectral shape shifts toward the higher frequency components, *i.e.* moving from the constant-steepness spectrum (14%) to Pierson-Moskowitz spectrum (20%) and finally to the constant-amplitude spectrum (22%). This trend is consistent with the fact that most of the energy lost in breaking comes from the high frequency end of the spectrum (Rapp and Melville 1990). In this paper, we show that wave directionality can also impact the loss of wave energy due to breaking.

2.2 Experimental Methods

The study was conducted in a 4 m x 11 m test section (Figure 2.1) within the Gunther Family Three-dimensional Wave Basin at the Massachusetts Institute of Technology. The mean water depth was h = 0.6 m. A coordinate system was chosen with x as the longitudinal (wave propagation) direction and x = 0 at the mean paddle position; y as the lateral direction and y = 0 at the mid-point of test section; z = 0 at the mean water level and positive upwards. The test section contained thirteen hydraulically driven wave-makers controlled by a central computer that can generate single frequency or spectral waves from 0.4 Hz to 3.0 Hz. The transfer function between the wave-maker and the observed surface displacement was determined using an impulse response method. The variation in transfer function due to temperature change was negligible.

The wooden frame beach had a slope of 1:5 and was covered with 4 inches (10 cm) of horsehair material. The maximum beach reflection was 5 % for monochromatic waves, based on the three-wave gauge method described in Rosengaus-Moshinsky (1987). Extrapolating these results to the multi-frequency wave-packets, beach reflection should contribute less than 5 % error to the estimation of local wave-packet energy.

The surface displacement was recorded using an array of 4-mm diameter, resistance-type wave gauges with 0.2 mm accuracy. The wave gauge signals were amplified and recorded at 200 Hz by a DAS1602 data acquisition board (Keithley Metrabyte) that was synchronized to the wave-maker system by external analog triggering. Wave records of 80 seconds were measured at 210 grid positions using an aluminum carriage system that straddled the measurement area (6 m x 4 m). The carriage system held seven wave gauges at the lateral positions y = 0, 15, 30, 45, 60, 90, 150 cm; and was traversed longitudinally in 20 cm increments from x =90 to 670 cm (Figure 2.1). A tighter lateral spacing was chosen near the centerline to capture the local details of the short-crested waves. Measurements between x = 0 and 90 cm were not considered because of interference from wave modes associated with the paddles (Dean and Dalrymple, 1984). Allowing for symmetry across the centerline, the entire measurement area was scanned using 30 repeatable runs. Before each experimental run, several tests were made to verify symmetry and repeatability, and to calibrate the wave gauges. Details of these tests are given in Nepf *et al.* (1998).

To compare the surface displacement measurements to the observed breaking locations, a CCD camera (COHU 4910) was used to acquire visual records of the breaking events from two viewing positions: (1) sideview and (2) backview, *i.e.* from

atop the paddles. The camera was synchronized to the wave gauge data acquisition and the wave maker system. A PCI frame grabber board (Bitflow Inc.) was used to acquire the images with 640 x 480 pixels for 20 seconds at 10Hz. A reference grid was constructed from a 1 cm rope strung across the test section at x = 200, 250, 300, 350, 400, 450 cm, and y = 0, 50, 100, 150 cm (gray lines in Figure 2.1). After correcting for parallax, these images provided spatial resolution with 5 cm accuracy. Finally, image contrast was enhanced to identify the spatial extent of the white-capping breaking region.

2.2.1 Wave Generation

A single, two-dimensional unsteady breaker can be generated using the constructive interference of dispersive wave components, a technique introduced by Cummins (1962), and Davis and Zarnick (1964) for testing ship models. Longuet-Higgins (1974), Greenhow and Vinje (1982), and Rapp and Melville (1990) extended this technique to generate an isolated breaker within a wave packet. The technique mimics the wave-wave interaction process that dominates the unsteady breaking associated with white-capping around the peak of the wind-wave spectrum in the field (Rapp and Melville 1990, Tulin and Li 1992). Indeed, previous laboratory results for two-dimensional breaking generated by this technique have been linked to field observations of energy dissipation (Melville 1994). In this study, we build on the frequency focusing technique by adding directionality, *i.e.* spatial focusing and diffraction, to the wave evolution producing three-dimensional, short-crested breakers. It is important to note that other mechanisms such as wave-current interaction (Longuet-Higgins and Stewart 1961, Kjeldsen and Myrhaug 1980), direct wind forcing (Banner and Phillips 1974),

intrinsic instability (Benjamin and Feir 1967), and wave shoaling (Duncan 1982, 1983) can also affect the breaking processes in the field. However, these mechanisms are not considered here.

The free surface displacement, $\eta(x,y,t)$, can be described by

$$\eta(x,y,t) = \sum_{n=1}^{N} a_n \cos[(k_n \cos\theta_n)x + (k_n \sin\theta_n)y - 2\pi f_n t + \phi_n], \qquad (2.1)$$

where a_n, k_n, ϕ_n, and θ_n are the amplitude, wave number, phase and propagation angle, respectively, for each of N wave components; and f_n is the nth frequency component given by the linear relationship

$$(2\pi f_n)^2 = k_n g \tanh(k_n h), \qquad (2.2)$$

where g and h are the gravitational constant and water depth, respectively. The surface displacement is thus described by the variables $N, f_n, a_n, \phi_n, \theta_n, h$, and the global parameter g.

To create a two-dimensional wave packet, the paddles were moved in unison so that the variables in (2.1) were the same for each paddle. Following Rapp and Melville (1990), the number of wave components, N, was chosen as 32, a number large enough to approximate a continuous spectrum. The thirty-two components, f_n, were equi-spaced across a bandwidth of $\Delta f = 0.789$ Hz and centered at frequency $f_c = (f_1 + f_{32})/2 = 1.08$ Hz. Each component amplitude was chosen to produce a constant wave steepness

$$a_n = \frac{G}{k_n}, \tag{2.3}$$

where G is the gain factor used to vary the overall intensity of the wave packet (Loewen & Melville 1991). In contrast to a constant-amplitude spectrum, *i.e.* a_n = constant, this condition inhibits premature breaking, because all components maintain similar scale with regard to steepness. In addition, the constant-steepness spectrum more closely mimics the wind-wave spectrum, *i.e.* $\propto f^{-5}$ (Phillip 1958). Finally, each phase component ϕ_n was determined using linear theory to achieve a theoretical focusing point at $x_f = 330$ cm (see Figure 2.2) and focusing time at $t_f = 12$ seconds. Applying the above constraints and setting the propagation angle, θ_n, to zero, the surface displacement required at each paddles, x_P, is then given by

$$\eta(x = x_P, t) = \sum_{n=1}^{N=32} \frac{G}{k_n} \cos[-k_n x_f - 2\pi f_n (t - t_f)]. \tag{2.4}$$

The time series of the input signal and the corresponding spectrum are shown in Figure 2.3. The input signal was tapered over its first and last second to eliminate abrupt paddle movement.

Two methods were introduced to generate short-crested waves by varying individual paddle motion. First, we consider a spatially focusing crest which may occur in the field when obliquely traveling wave-packets meet, *e.g.* after passing around an

island or due to wave generation by spatially varied wind direction. To produce this wave in the laboratory, the propagation angle θ_{mn} was varied at each paddle, m, and was selected such that the wave train from each paddle converged at position (x_f, y_f) at time $t_f = 12$ seconds (Figure 2.2). From geometry, the propagation angle, θ_{mn}, for the m th paddle was determined as

$$\theta_{mn} = \tan^{-1}(\frac{x_f}{|m|b}), \tag{2.5}$$

where b is the width of each paddle and m is an integer from -6 to 6. The maximum propagation angle, $\theta_{\max} = \theta_{6n}$,was used to characterize the total degree of wave focusing. The remaining parameters $N, a_n,$ and f_n were kept the same as the two-dimensional case. To produce a frequency and spatially focusing crest, the surface displacement required at each paddle was then given by

$$\eta(x = x_P, y = mb, t) = \sum_{n=1}^{N=32} \frac{G}{k_n} \cos[-k_n(|mb|\sin\theta_{mn} + x_f \cos\theta_{mn}) - 2\pi f_n(t - t_f)]. \tag{2.6}$$

Because the paddle width and the total number of paddles were fixed by the facility, the maximum propagation angle $\theta_{\max}$ could only be varied only through, x_f, the distance between the paddles and the focusing point. In this study, we considered a fixed angle, $\theta_{\max} = 31^o$, prescribed by $x_f = 330$ cm, the same focusing distance used for the two-

dimensional waves. For reference, She *et.al* (1994) investigated $\theta_{\max} = 0^o \sim 89^o$ and found that breaking height and severity increase as $\theta_{\max}$ increases.

The second type of short-crested breaking considered here is a diffracting wave. This wave mimics field conditions in which small-scale heterogeneity within the wind field produces small-scale heterogeneity within the wave field, specifically spatial amplitude variation. To create this type of wave, a lateral variation in wave amplitude was introduced. The central paddles were moved together at the maximum amplitude and the remaining paddles were tapered down to 10% using a cosine window (Figure 2.2). This transverse tapering produced passive directional spreading during wave evolution. The surface displacement of the m th paddle was then described by

$$\eta(x = x_P, y = mb, t) = \begin{cases} \sum_{n=1}^{N=32} \frac{G}{k_n} \cos[-k_n x_f - 2\pi f_n (t - t_f)], & |m| < \frac{L_o}{2b} \\ \sum_{n=1}^{N=32} \frac{G}{k_n} \cos[-k_n x_f - 2\pi f_n (t - t_f)][0.1 + 0.9\cos^2(\frac{m\pi}{12})], & |m| > \frac{L_o}{2b} \end{cases} \quad (2.7)$$

where L_o is the length of central paddles without tapering. The degree of diffraction depends on both L_o as well as the distance to focusing location, x_f, yielding a dimensionless diffraction parameter, x_f / L_o. For a two-dimensional wave, L_o is effectively infinite such that $x_f / L_o = 0$ for all values of x_f, indicating that the two-dimensional breaking dynamics is insensitive to x_f, as demonstrated by Rapp and Melville (1990). As x_f / L_o increases, the effects of diffraction also increase, as shown

by Nept *et al.* (1998). In this study, L_o was chosen to be 90 cm, *i.e.* three paddles long, resulting in a fixed $x_f / L_o = 3.67$.

The full range of three-dimensional wave packet evolution in the basin can now be described by the non-dimensional set:

$$\eta k_c = \eta k_c [\theta_{\max} \text{ or } x_f / L_o ,\ \Delta f / f_c ,\ k_c h ,\ a k_c], \tag{2.8}$$

where the central wave number, $k_c = 4.73$ m^{-1}, corresponds to the central frequency , f_c, using (2.2). The maximum focusing angle $\theta_{\max}$ and diffracting parameter x_f / L_o were selected as described above. A fixed frequency bandwidth ratio, $\Delta f / f_c$=0.73, was selected because it produced the most distinct transition between the two-dimensional spilling and plunging cases as defined by Rapp and Melville (1990). Moreover, the frequency bandwidth ratio was not varied in this study because Rapp and Melville (1990, Figure 17) showed that it has little influence on breaker onset and severity. It should also be noted that for a broad-banded spectrum, as used in this study, nonlinear wave modulations (second order effects) are not important in long-crested breaking and even less pronounced for directional short-crested breaking (Stansberg, 1992, 1995) so that the linear theory is a reasonable approximation for non-breaking waves. The depth parameter $k_c h$ was chosen to produce deep-water waves, eliminating the dependence of wave evolution on water depth. For a central wave number k_c, the value of $\tanh(k_c h) = 0.99$, indicating that the deep-water wave condition was met at the scale of the wave packet.

Finally, the intensity of breaking, from incipient to plunging waves, was varied through the gain, G, and parameterized by the global, spectrum-based wave-steepness ak_c (Rapp and Melville 1990), *i.e.*

$$ak_c = (\sum_{n=1}^{32} a_n)k_c = G(\sum_{n=1}^{32} \frac{1}{k_n})k_c, \tag{2.9}$$

where a_n is defined by (2.3). The classifications of an incipient wave, spiller, and plunger are defined as in Rapp and Melville (1990). Photographs depicting waves at each of these breaking condition were presented in Rapp and Melville (2D waves, 1990) and Nepf *et al.* (3D diffracting waves 1998). Here, the plungers of spatially focusing, diffracting and two-dimensional waves are shown to demonstrate the differences of the spatial signature (Figure 2.4). The two-dimensional plunger broke uniformly across the wave crest (Figure 2.4a). Of the short-crested waves, the spatially focusing plunger (Figure 2.4b) was more localized and energetic than the diffracting plunger (Figure 2.4c).

2.2.2 Breaking Wave Criteria

Breaking wave criteria can be classified into three major categories. First, geometric criteria are based on the geometry of wave shape. Second, kinematic criteria are based on the characteristics of wave motions, *e.g.* particle velocity and wave phase speed. Third, dynamic criteria are based on the characteristics of wave energy. In this study, we compare representative criteria from each category and assess their performance in directional wave fields.

2.2.2.a Geometric Criterion

Two types of wave shape parameter were considered here: (1) global wave steepness, ak_c, which characterizes the maximum potential steepness based on the sum of spectral components, and (2) local wave steepness and asymmetry. The later includes the crest front steepness (ε), the crest rear steepness (δ) the vertical asymmetry factor (λ), and the horizontal asymmetry factor (μ), each of which is defined in Figure 2.5. These parameters are frequently used to characterize steep asymmetrical waves or breaking waves. Following Kjeldsen and Myrhuag (1979, 1980), these parameters were estimated from the temporal records of surface displacement using zero-downcross analysis and assuming that time- and length- scales are related by the dispersion relationship for deep-water waves, *i.e.* $L = gT^2 / 2\pi$.

2.2.2.b Kinematic Criterion

The most common kinematic criterion is the ratio of particle velocity, $|\bar{U}|$, and phase speed, C, with breaking predicted for $|\bar{U}|/C \geq 1$ (Longuet-Higgins 1969, Tulin and Li 1992). To obtain the particle velocity and the phase speed from the measured surface displacements, we extended the Hilbert transform technique, previously applied to two-dimensional waves (Melville 1983, Hwang *et al.* 1989, and Huang *et al.* 1992), to directional wave fields as follows. Suppose that the surface fluctuations can be described as

$$Z(x,y,t) = \eta(x,y,t) + i\zeta(x,y,t), \tag{2.10}$$

where $\eta(x,y,t)$ is the measured vertical surface displacement and $\zeta(x,y,t)$ is its conjugate part. The conjugate is related to η through the Hilbert transform as

$$\zeta(x,y,t) = -\frac{1}{\pi}\int_{-\infty}^{\infty}\frac{\eta(x,y,\tau)}{\tau - t}d\tau, \tag{2.11}$$

and can be interpreted as the horizontal surface displacement. To first order, the local horizontal particle velocity can then be evaluated as

$$|\vec{U}| = [u(x,y,t)^2 + v(x,y,z)^2]^{1/2} = |\frac{\partial \zeta}{\partial t}|, \tag{2.12}$$

where $u(x,y,t)$ and $v(x,y,t)$ are the local velocity components along the longitudinal x and transverse y directions, respectively. The local phase speed, C, is defined as

$$C = \frac{2\pi f(x,y,t)}{|k(x,y,t)|}, \tag{2.13}$$

where $f(x,y,t)$ and $k(x,y,t)$ are the local frequency and the local wave-number, which are estimated as follows. Note that (2.10) can be expressed in polar form as

$$Z(x,y,t) = A(x,y,t)e^{i\phi(x,y,t)}, \tag{2.14}$$

where $A(x,y,t)=[\eta(x,y,t)^2+\zeta(x,y,t)^2]^{1/2}$ and $\phi(x,y,t)=\tan^{-1}[\zeta(x,y,t)/\eta(x,y,t)]$ are the instantaneous envelope and the local phase function, respectively. The local frequency is thus obtained by

$$f(x,y,t)=\frac{1}{2\pi}\frac{\partial\phi(x,y,t)}{\partial t}=\frac{\frac{\partial\varsigma}{\partial t}\eta-\frac{\partial\eta}{\partial t}\varsigma}{2\pi(\eta^2+\varsigma^2)}, \tag{2.15}$$

and the local wave number is evaluated by (2.2), *i.e.*, $|k(x,y,t)|=2\pi/gf^2(x,y,t)$ for the deep-water condition. In this study, (2.12) and (2.13) were used to evaluate the parameter $|\vec{U}|/C$ for each time interval and spatial position. Threshold values of $|\vec{U}|/C$ were then assessed through comparisons to visual observations of breaking recorded on digital video images.

2.2.2.c Dynamic Criterion

Wave focusing and breaking are manifested by up-frequency energy shifts and subsequent losses, respectively (Rapp and Melville 1990). This suggests that the evolution of the higher harmonic frequency band may be used as a dynamic criterion for breaking. The energy content of the higher harmonic frequency range was examined as follows. First, the surface displacement records were windowed for 40 seconds. Second, the spectrum, $S_{\eta\eta}$, associated with the windowed wave packet was calculated using an 8192 point FFT with a three-point moving-average filter. Third, the spectrum was divided into two frequency bands: the primary frequency band, 0.68 ~1.5 Hz, that

corresponded to the input signal, and the higher frequency band, above 1.5 Hz. The energy content of each frequency band, E_1 and E_2, respectively, was estimated by integrating the spectrum over the corresponding frequency range. The evolution of E_2 reflects the intra-wave energy exchange associated with changes in wave steepness and asymmetry that occur as the wave focuses and approaches breaking. As with the kinematic parameter described above, visual observations of breaking were compared with the evolution of E_2.

2.2.3 Energy losses

Energy losses were estimated following a method developed for two-dimensional waves by Rapp and Melville (1990) and extended to short-crested waves by Nepf et al. (1998). Rapp and Melville (1990) showed that, except near the point of breaking where the assumption of energy equipartition breaks down, the momentum and energy fluxes of a wave-packet can be estimated from the surface displacement variance, $\overline{\eta^2}$, defined as

$$\overline{\eta^2} = \frac{1}{T}\int_0^T \eta^2 dt \ , \tag{2.16}$$

where the integration time, T, is chosen to be long enough to capture the passage of the wave-packet through the test section, here 40 seconds. The loss of wave energy within the test section is then given by the difference in the energy flux observed at the up- and downstream ends. For the two dimensional waves considered by Rapp and Melville (1990) this loss represents viscous dissipation in the wall- and bottom-boundary layers

and the effects of wave breaking. When the waves are short-crested additional changes in local wave energy arise from diffraction and spatial focusing. These directional effects, however, only reflect a lateral redistribution of wave energy that contributes no net loss to the laterally-averaged packet. Thus, the directional effects can be eliminated by applying a lateral average between the basin boundaries, *i.e.* between $y = \pm 6b$. Assuming that the group velocity is constant, the total loss of wave energy between an upstream (subscript 'o') and downstream (subscript 'd') position is the given by

$$D = \frac{\Delta \int_{-6b}^{6b} \overline{\eta^2}\, dy}{\left(\int_{-6b}^{6b} \overline{\eta_o^2}\, dy \right)} = \frac{\int_{-6b}^{6b} \overline{\eta_o^2}\, dy - \int_{-6b}^{6b} \overline{\eta_d^2}\, dy}{\left(\int_{-6b}^{6b} \overline{\eta_o^2}\, dy \right)}. \tag{2.17}$$

The lateral integration is evaluated using the wave gage records at the grid positions shown in Figure 2.1, and assumes symmetry across the centerline. The loss of wave energy, D, observed for the incipient (non-breaking) condition is assumed to represent the viscous dissipation. Losses observed for the breaking wave-packets that are in excess of those observed for the incipient case are then attributed to the breaking process. To properly compare the short-crested waves with the two-dimensional waves, the breaking loss is normalized by the observed breaking-crest length. The additional details of this technique can be found in Nepf *et al.* (1998) and Rapp and Melville (1990).

2.3. Results

2.3.1 Surface Displacement Time Series

Figure 2.6 compares the surface displacement record at the centerline of each wave-packet considered. For the incipient condition (Figure 2.6a), the two-dimensional and short-crested waves are similar. In each case dispersion was observed with the shorter waves leading before the theoretical focusing location, $x_f = 330$ cm, and trailing after, as prescribed by linear theory. For the spilling wave (Figure 2.6b), breaking was initiated on the leading crest at $x = 370$ cm (based on video observation) causing the wave height to decrease from $x = 370$ cm to 450 cm. The short-crested spilling waves began to deviate from the two-dimensional waves after $x = 370$ cm, reflecting that the differences in breaking intensity and that the effects of wave directionality had reached the centerline. The plunging breaker (Figure 2.6c) occurred one wavelength upstream, at $x = 270$ cm. For the spatially focusing wave higher frequency oscillations appeared after plunging, *e.g.* at $x = 290$ cm, $t = 10.5$ seconds. These oscillations are attributed to the splashing and/or small random waves generated by the impact of the localized and highly energetic jet. These oscillations were absent from the two-dimensional and diffracting plungers because their jet structure was laterally more uniform and less energetic.

The distinctive crest shape of each wave type is best observed by comparing the surface displacement records at different lateral positions (Figure 2.7). The two-dimensional wave-packet produced a laterally uniform crest that broke simultaneously in space and time across the entire test section (Figure 2.7a, see also Figure 2.4). In contrast, both short-crested wave-packets exhibited lateral variation in crest position and in breaking intensity (I, S, P), which was defined by visual observations. The diffracting

wave crest was crescent-shaped with the centerline leading (Figure 2.7c). The focusing wave crest was narrower with more synchronous peak arrival across its crest (Figure 2.7b). In addition, this crest cupped forward reflecting the focusing of wave energy toward a single point

.

3.2 Geometric Breaking Criterion

2.3.2.a Local Wave Shape parameters

The crest-front steepness, ε, measured along the crest at the onset of a plunging breaker is shown in Figure 2.8 for each of the wave types considered. While the two-dimensional crest exhibited a uniform steepness, $\varepsilon = 0.82$, the steepness of both directional crests decreased away from the centerline. Note that plunging was not precipitated for the focusing crest until the centerline steepness reached $\varepsilon = 1.22$. This is consistent with the previous spatial focusing experiments that observed an increase in both ε and breaking severity as the angle of wave interaction increased (She *et al.* 1994, Kolaini and Tulin 1995). In contrast, the centerline criterion for the diffracting wave is comparable to the two-dimensional crest. For both directional waves, once plunging is precipitated at the centerline it occurs off-center at less than critical steepnesses. This suggests that the introduction of turbulence and/or surface instabilities by the centerline breaking provokes breaking off-center at less than the critical steepness, *i.e.* reduces the effective breaking criteria. Similarly, Ramberg and Griffin (1987), Kolaini and Tulin (1995), and Nepf *et al.* (1998) observed lower breaking steepnesses in the presence of turbulence left by previous breaking events. These observations suggest that oceanic turbulence may lower breaking criteria in the field relative to values observed in pristine

tanks or predicted by theory. The spilling condition also exhibited trans-crest variation in ε, which was similar to that observed for the plunging criteria (Figure 2.8).

Table 2.1 summarizes observations of ε, δ, λ, and μ from several laboratory and field experiments. First, note that for each of the two-dimensional wave conditions, breaking is initiated at comparable steepness. These steepnesses are less than that of the Stokes limiting wave, confirming that unsteady waves are more sensitive to breaking (Longuet-Higgins 1996). Second, consistent with the previous results (She *et al.* 1994, Nepf *et al.* 1998), the present experiments show that the local wave shape parameters observed at the onset of breaking (left-hand columns) are strongly influenced by wave directionality. Specifically, the wave steepnesses increase monotonically from conditions of diffraction (negative focusing) through planar wave (two-dimensional) crests to positive spatial focusing. This sensitivity to wave directionality, along with trans-crest variation in breaking steepness (Figure 2.8), may explain the range of local wave steepness observed in the field, *e.g.* $\varepsilon = 0.32 \sim 0.78$ (Kjeldsen and Myrhaug 1979, 1980). The crest rear steepness, δ, and vertical asymmetry factor, λ, have similar characteristics to those described for ε. Finally, the wave parameters for spiller reported in Table 2.1 suggest that the horizontal asymmetry factor $\mu = 0.67$, based on Stokes limiting waves, may be a good indicator for breaking. But the present experiments observed $\mu = 0.74$ for incipient waves without breaking, *i.e.* higher than that observed for spilling breakers. This suggests that μ is not sufficient to characterize the onset of breaking. Overall, we conclude that the local wave shape parameters may not be used as robust indicators for oceanic wave breaking.

2.3.2.b Spectrum-Based Global Wave Steepness

Table 2.2 summarizes the spectrum-based global wave steepness, ak_c, under conditions of different spectral shape and wave directionality. A comparison of the two-dimensional experiments (Rapp and Melville 1990, Lamarre 1993, Chaplin 1996, Kway *et al.* 1998) shows that the breaking criteria are shifted upward as the spectral components are shifted downward, *i.e.* as relatively greater energy resides in the lower frequency components from constant-amplitude through Pierson-Moskowitz to constant-steepness spectra. This suggests that wave fields consisting of relatively greater contributions of low frequency energy are more stable, *i.e.* have higher thresholds for breaking. The present experiments show that the global wave steepness is also sensitive to wave directionality, with the incipient criteria decreasing from the diffracting wave, to the two-dimensional wave, and then to the focusing wave (Table 2.2). The same trends are observed for the spilling and plunging criteria. Since both spectral shape and wave directionality affect the global wave steepness criteria, one should be cautious when extrapolating specific laboratory results to oceanic wave fields.

2.3.3. Kinematic Breaking Criterion

When particle velocity $|\vec{U}|$ exceeds the phase speed C, breaking should occur (Longuet-Higgins 1969). Based on the two-dimensional, numerical wave-tank simulations, Wang *et al.* (1993), Yao *et al.* (1994) and Tulin (1996) alternatively suggested that for deep-water waves breaking is initiated when $|\vec{U}|$ exceeds the local wave group velocity, $C_g = 0.5C$, *i.e.* $|\vec{U}|/C = 0.5$. Two explanations can be offered for this discrepancy. First, the concept of group velocity is not well defined for nonlinear

unsteady conditions such that the estimate of group velocity may vary significantly in deep water (Longuet-Higgins 1996). Second, the condition $|\vec{U}|/C = 0.5$ may differentiate a wave that will eventually evolve to breaking, but the actual breaking event doesn't occur until $|\vec{U}|/C = 1$ (Wang *et al.* 1993). Observations from the present experiments can be used to resolve the above issues. Using (2.12) and (2.13), the ratios of particle velocity, $|\vec{U}|$, and wave phase speed, C, are calculated and shown as the solid lines in Figure 2.9, 2.10, and 2.11 for the incipient wave, spiller, and plunger, respectively. The dashed lines represent the threshold value of the proposed kinematic breaking criterion, $|\vec{U}|/C = 1$.

For the incipient wave, we consider the longitudinal position $x = 330$ cm because it is the location at which the maximum particle velocity occurs. All three incipient waves (Figure 2.9) reach $|\vec{U}|/C > 0.5$ at some location along the wave crests but no breaking is initiated, suggesting that the criterion $|\vec{U}|/C = 0.5$ is not appropriate for detecting unsteady breaking waves. In addition, the ratio $|\vec{U}|/C$ remains less than one for all three incipient wave crests, consistent with the breaking criterion $|\vec{U}|/C \geq 1$.

The criterion for a spilling breaker, as suggested by Longuet-Higgins (1969), is that the particle velocity must be slightly larger than the phase speed, *i.e.* $|\vec{U}|/C \geq 1$. For the two-dimensional spiller the ratio $|\vec{U}|/C$ exceeds one at all lateral positions and $t = 12$ seconds (Figure 2.10a). This is consistent with video observations that spilling occurred uniformly and simultaneously across the test section at $x = 370$ cm and $t = 12$ seconds. For the spatially focusing spiller (Figure 2.10b), $|\vec{U}|/C \geq 1$ occurs at the lateral positions y = 0, 15, 30, and 45 cm but not at positions y = 60, 90 and 150 cm,

consistent with video observations of breaking. Similarly, $|\vec{U}|/C \geq 1$ occurs along the crest of the diffracting spiller (Figure 2.10c) except at the lateral positions y = 90 and 150 cm, where again, based on video observations, the crest was not breaking. The above examination proves that the condition $|\vec{U}|/C \geq 1$ is a good indicator for detecting spilling breakers.

For a plunger to occur, the kinematic ratio should increase beyond that for the spiller. For example, using a Particle Image Velocimetry (PIV) technique, Perlin *et al.* (1996) and Chang and Liu (1998) showed that the particle velocity at the tip of a two-dimensional overturning jet reached 1.3 ~ 1.6 times of the wave phase speed. She *et al.* (1997) observed $|\vec{U}|/C \approx 1$ for spatially focusing plungers, but they cautioned that their measurement of particle velocity at the crest may have suffered from reduced image quality. In the present experiments, $|\vec{U}|/C > 1.5$ occurs at all lateral positions and at $t = 10.2$ seconds for the two-dimensional plunger (Figure 2.11a), consistent with video observations. For the spatially focusing (Figure 2.11b) and diffracting (Figure 2.11c) waves, $|\vec{U}|/C \geq 1.5$ occurs at the lateral positions for which the breaking was observed (video images, *e.g.* as in Figure 2.4).

The above observations demonstrate that the ratio $|\vec{U}|/C$ not only detects breaking but also reveals variation in breaking intensity along a wave crest, *i.e.* the ratio robustly distinguishes plunger ($|\vec{U}|/C \geq 1.5$), spiller ($|\vec{U}|/C \geq 1$) and incipient wave ($|\vec{U}|/C < 1$) along a single crest (Figure 2.11b, 2.11c). In addition, these observations indicate that this kinematic criterion is insensitive to wave directionality. This kinematic

criterion using the Hilbert transform analysis is thus a promising method for detecting oceanic breaking.

2.3.4. Dynamic Breaking Criterion

Up-frequency shifts in wave energy associated with wave focusing have been observed for two-dimensional (Rapp and Melville 1990, Kway *et al.* 1998) and three-dimensional (She *et al.* 1994, Nepf *et al.* 1998) wave packets of different spectral shape. In the present experiments we investigate the effects of spatial focusing on the E_2 signature. The energy content of the higher harmonic band, E_2, for the incipient wave (Figure 2.12) exhibits periodic behavior, increasing as the wave focuses and subsequently decreasing with little net change in energy downstream of the focal point. With breaking (the spiller and plunger), the wave energy was shifted to the higher harmonic band and subsequently lost to the turbulent field. These results are consistent with similar observations made for two-dimensional and diffracting wave crests (Nepf *et al.* 1998), indicating that wave directionality does not influence the E_2 signature. However, the observed evolution of E_2 is very sensitive to the choice of reference position. In addition, multiple measurement positions are needed to construct the spatial evolution of E_2. For these reasons, the dynamic breaking criterion based on the evolution of E_2 is not as convenient or robust as the single-point kinematic criterion for detecting oceanic breaking.

2.3.5. Energy losses

Following the procedure described in Section 2.2.3, the wave energy dissipation for the incipient wave, spiller, and plunger is calculated using (2.17). For each wave condition, *i.e.* the two-dimensional, focusing, and diffracting waves, the incipient wave-packet lost 10% of its energy. This loss is associated with viscous dissipation in the boundary layer and error in the lateral integration of wave energy. The energy loss observed for spilling and plunging wave-packets beyond that observed for the incipient wave is attributed to the breaking process. The breaking loss is normalized by the breaking crest length, which is (1.5 $\pm$ 0.3) m for the focusing plunger and is (2.2 $\pm$ 0.3) m for the diffracting plunger. The same procedure is applied for the spilling breakers.

Table 2.3 summarizes the energy loss per crest length due to breaking under conditions of different spectral distribution and wave directionality. As suggested by Kway *et al.* (1998), the breaking loss increases as the spectral shape shifts toward the higher frequency components. The trend is similar, but less pronounced, for the spillers. This trend is consistent with the fact that most of the energy lost in the breaking process comes from the high frequency end of the spectrum (Rapp and Melville 1990, Lammare 1993). The present experiments demonstrate that the wave directionality can also influence the fractional energy loss associated with wave breaking. With the same spectral shape (constant-steepness spectrum), the spatially focusing wave (34%) lost about twice as much energy as the two-dimensional wave (16%). The energy loss for the diffracting wave, which was visibly milder than the focusing wave, was comparable to its two-dimensional counter-part. Since both wave directionality and spectral shape are shown to influence wave energy dissipation due to breaking, one should be cautious

when extrapolating two-dimensional laboratory results to the spectrally evolving and directional wave fields in the open ocean.

2.4 Summary

In this study, we generated fully three-dimensional breaking waves, *i.e.* spatially focusing and diffracting waves, by building on the two-dimensional, frequency-focusing technique for wave generation (Rapp and Melville 1990). The new wave generation technique was used to examine the effects of wave directionality on breaking wave criteria and energy losses associated with wave breaking.

The experimental results show that wave directionality, spectral shape and the introduction of turbulence by the antecedent breaking (*e.g.* at the centerline) can all affect the local wave shape parameters at the onset of breaking. These effects may explain the range of local wave shape parameters observed in the field (Kjeldsen and Myrhaug 1979, 1980) and why geometric local wave shape parameters have not proved to be stable limits for ocean wave breaking. A similar conclusion can be reached with regard to the global steepness parameter, ak_c.

Using single-point surface displacement measurements and the Hilbert transform, Hwang *et al.* (1989) showed that the kinematic criterion $|\bar{U}|/C \geq 1$ is a good indicator for breaking for two-dimensional wind-generated waves. In this study, a spatial mapping of surface displacement measured by an array of wave gauges is used to extend this method and to verify this criterion for directional breaking waves. The present experiments show that the ratio $|\bar{U}|/C$ not only detects breaking locations along a single crest but also reveals variation in breaking intensity. Specifically, the ratio differentiates

directional plunging and spilling with $|\vec{U}|/C \geq 1.5$ and $|\vec{U}|/C \geq 1$, respectively. Combining this promising result with previous studies for two-dimensional breaking (Huang *et al.* 1992, Griffin *et al.* 1996, and Seymour *et al.* 1998), we believe that this single-point kinematic criterion using the Hilbert transform can be used as a robust indicator for ocean breaking waves.

The present experiments show that spatial focusing and diffraction do not alter the up-frequency transfer associated with wave steeping. However, we conclude that the dynamic criterion based on the evolution of E_2 is fairly qualitative and very sensitive to the choice of reference location. In addition, multiple-point measurements are required to interpret the evolution of E_2, which may not be feasible in the field.

Finally, the energy loss for the spatially focusing plunger is found to be about two times higher than that for the two-dimensional plunger, consistent with the suggestion that breaking severity increases with increasing spatial focusing angle (She *et al.* 1994). This observation suggests that wave directionality can play an important role in determining breaking losses. More measurements are required to resolve the relationship between energy loss and focusing angle across a wider parameter range.

Acknowledgments. This research was supported by Office of Naval Research under Contract N00014-94-1-0610. We would like to thank Paul Fricker for his assistance with taking the photographs, and Dr. Jame B. Edson and Dr. Ole Madsen for their valuable discussions on breaking wave criteria.

2.5 References

Baldock, T., Swan, C., and Taylor, P., "A laboratory study of nonlinear surface waves on water," *Phil. Trans. R. Soc. Lond.,* **A452**, pp. 649-676, 1996.

Banner, M. L. and Peregrine, D. H., "Wave Breaking in deep water," *Annu. Rev. Fluid Mech.,* **25**, pp. 373-397, 1993.

Benjamin, T. and Feir, J., "The disintegration of wave trains in deep water," *J. Fluid Mech..,***27**, pp. 373-397, 1967.

Bonmarin, P., "Geometric properties of deep water breaking waves," *J. Fluid Mech.,***209**, pp.405-433, 1989.

Chang, K. A. and Liu, P. L. F., "Velocity, acceleration and vorticity under a breaking wave," *Physics of Fluids*, **10 (1)**, pp. 327-329, 1998.

Chaplin, J., "On frequency-focusing unidirectional waves," *Int. J. Offshore Polar Eng.*, **6**, pp. 131-137, 1996.

Cummins, W., "The impulse response function and ship motion," *Schiffstechnik Forschungsh. Schiffbau Schiffsmaschineubau,* **9**, pp. 101-109, 1962.

Davis, M. and Zarnick, E., "Testing ship models in transient waves," *5th Symp. on Naval Hydrodynamics*, ACR-**112**, pp. 509-540, ONR, Washington, D.C., 1964.

Duncan, J., "An experimental investigation of breaking waves produced by a towed hydrofoil," *Proc. Royal Soc. Lond.,* A, **377**, pp. 331-348, 1982.

Duncan, J., "The breaking and non-breaking wave resistance of a two-dimensional hydrofoil," *J. Fluid Mech.,* **126**, pp. 507-520, 1983.

Easson, W. J., "Breaking waves," *Offshore Technology Report*, **OTO-96-035**, 1997.

Griffin, O. M., Peltzer, R. D., and Wong, Henry T., "Kinematic and dynamic evolution of deep water breaking waves," *J. Geophys. Res.* **101** (C7), pp. 16515-16531, 1996.

Greenhow, M. and Vinje, T., "A theoretical and experimental study of the capsize of Salter's Duck in extreme waves," *J. Fluid Mech.*, **118**, pp. 221-239, 1982.

Huang, N. E., Long, S. R., Tung, C.C., Donelan, M. A., Yuan, Y., and Lai, R. J., "The local properties of ocean waves by phase-time method," *Geophys. Res. Lett.,* **19(7)**, pp. 685-699, 1992.

Hwang, P. A., Xu, D., Wu Jin, and J., "Breaking of wind-generated waves, measurements and characteristics," *J. Fluid Mech.*. **202**, pp.177-200, 1989.

Kerman, B.R. (Ed.), "*Sea Surface Sound - Natural Mechanics of Surface Generated Noise in the Ocean*," Kluwer Acad., Norwell, Mass, **639**, 1988.

Kway, J. H. L., Loh, Y. S., and Chan, E. S., "Laboratory study of deep-water breaking waves," *Ocean Eng.* **25**, 8, pp.657-676, 1998.

Kjeldsen, S. P. and Myrhaug, D., "Kinematics and dynamics of breaking waves," *Rep. STF60 A78100, Ships in the Rough Sea*, Part **4**, Norwegian Hydrodynamic Laboratories, Trondheim, Norway, 1978.

Kjeldsen, S. P. and Myrhaug, D., "Breaking waves in deep water and resulting wave forces," *Proc. 11 Offshore Tech. Conf.*, **3646**, Houston, Texas, 1979.

Kjeldsen, S. P. and Myrhaug, D., "Wave-wave interactions, current-wave interactions and resulting extreme waves and breaking waves," *Proc.17th Conf. on Coastal Engineering, ASCE, Sydney,* **3**, pp. 2277-2303, 1980.

Kolaini, A. and Tulin, M., "Laboratory measurements of breaking inception and post-breaking dynamics of steep short-crested waves," *Int. J. of Offshore and Polar Engineering,* **5**, pp. 212-218, 1995.

Lamarre, E. (1993), "*An experimental study of air entrainment by breaking waves*," Ph.D. Thesis, Massachusetts Institute of Technology, 1993.

Longuet-Higgins M. S. and Stewart, R. W., "The changes in amplitude of short gravity waves on steady non-uniform current," *J. Fluid Mech.*, **10**, pp. 529-549,1961.

Longuet-Higgins, M. S., "On wave breaking and equilibrium spectrum of wind," *Proc. R. Soc. Lond.*, **A 310**, pp. 151-159, 1969.

Longuet-Higgins, M. S., "Breaking waves in deep and shallow water," *Proc. 10th Conf. in Naval Hydrody*, pp. 597-605, 1974.

Longuet-Higgins, M. S., "Progress towards understanding how wave breaks," *Proc. 21th Symposium on Naval Hydrodynamics*, Tronheim, Norway, 1996.

Melville, W. K., "The instability and breaking of deep-water waves," *J. Fluid Mech.*, **115**, pp. 163-185, 1982.

Melville, W. K., "Wave Modulation and breakdown," *J. Fluid Mech.*, **128**, pp. 489-506, 1983.

Melville, W. K., "Energy dissipation by breaking waves," *J. Phys. Oceanogr.*, **24**, pp. 2041-2049, 1994.

Melville, W. K., "Wave breaking in air-sea interaction," *Ann. Rev. of Fluid Mechanics,* **28**, pp. 279-321, 1996.

Nepf, H. M., Wu, C. H., and Chan, E. S., "A comparison of two- and three-dimensional wave breaking," *J. Phys. Oceanogr.*, **28**, pp. 1496-1510, 1998.

Peregrine, D. H., "Breaking waves on beaches," *Ann. Rev. of Fluid Mech.*, **15**, pp. 149-178, 1983

Perlin, M., He, J., and Bernal, L. P., "An experimental study of plunging breakers," *Phys. Fluids,* **8 (9),** pp. 2365-2374, 1996.

Phillips, O. M., "The equilibrium range in spectrum of wind-generated wave," *J. Fluid Mech.*,**4**, pp. 89-99, 1958.

Rapp, R. J. and Melville, W. K., "Laboratory measurements of deep water breaking waves," *Phil. Trans. R. Soc. London,* **A, 331**, pp. 735-780, 1990.

Rosengaus-Moshinsky, M., "*Experimental study of wave generated bedforms and resulting wave attentuation*," Ph.D. Thesis, Massachusetts Institute of Technology, 1987.

Seymour, R., Zimmermann, C.A. and Zhang, J., "Discriminating breaking in deep water waves," pp. 305-313, *Ocean Wave Kinematics, Dynamics and Loads on Structures*, 1998.

She, K., Greated, C. A. and Easson, W. J., "Experimental study of three-dimensional wave breaking," *J. of Waterway, Port, Coastal, and Ocean Eng.* **120**, pp. 20-36, 1994.

She, K., Greated, C. A. and Easson, W. J., "Experimental study of three-dimensional breaking waves kinematics," *Applied Ocean Res.* **19**, pp. 329-324, 1997.

Stansberg, C. T., "Effects from directionality and spectral bandwidth on non-linear spatial modulation of deep water surface gravity wave trains," *Proc. of 24th ASCE Int. Conf. on Coastal Eng.*, **1**, pp. 579-593, Kobe, Japan, 1995.

Stansberg, C. T, "On spectral instabilities and development of non-linearities in deep-water propagation wave trains," *Proc. of 23rd Int. Conf. on coastal Eng.*, **1**, pp. 658-671, 1992.

Stokes, G., "Supplement to a paper on the theory of oscillatory waves," *Mathematical and Physical Papers,* **1**, pp. 314-326, 1880.

Su, M. Y., "Three-dimensional deep-water waves, Part 1: Experimental Measurements of skew and symmetric wave pattern," *J. Fluid Mech.*, **124**, pp. 73-108, 1982.

Su, M. Y., Bergin, M., Marler, P., and Myrick R., "Experiment on nonlinear instabilities and evolution of steep gravity-wave trains," *J. Fluid Mech.* **124**, pp. 45-72, 1982.

Su, M. Y. and Green, A., "Wave breaking and nonlinear instability coupling," *The Ocean Surface: Wave Breaking, Turbulent Mixing, and Radio Probing* , edited by Y. Toba and H. Mitsuyasu, Kluwer Academic., pp. 31-38, 1985.

Thorpe, S. A., "Dynamical process of transfer at the sea surface," *Progress Oceanog.*, **35**, pp. 315-352, 1995.

Thorpe, S. A., "Energy loss by breaking waves," *J. Phy Oceanogr.*, **23**, 2498-2502, 1993.

Tulin, M. P. and Li, J., "On the breaking of energetic waves," *Int. J. of Offshore and Polar Eng.*, **2**, pp. 46-53, 1992.

Wang, P., Yao, Y., and Tulin, M. P., "Wave groups, wave-wave interaction and wave breaking, result of numerical experiments," *Proc. of 3rd Int. Offshore and Polar Eng,, III,* pp. 27-33, Singapore, 1993.

Yao, Y., Wang, P. and Tulin, M. P., "Wave groups, wave-wave interaction and wave breaking, result of numerical experiments," *Proc. 20th Symp. on Naval Hydrodynamics*, Santa Barbara, CA, National Academic Press, 1994.

Table 2.1. Comparison of geometry breaking criteria based on local wave shape parameters.

		ε		δ		λ		μ	
Stokes limiting wave 2D		0.48		0.48		1.00		0.67	
Kjeldsen and Myrhaug (1979, 1980) 2D, Field+		0.32	0.78	0.26	0.39	0.90	2.18	0.84	0.95
Bonmarin (1989) 2D periodic or dispersive waves		0.31	0.85	0.26	0.33	0.72	3.09	0.60	0.93
She *et al.* (1994) 3D focusing angle Skyner's Spectrum (1990)	Single-Frequency	0.82	1.52	0.66	0.96	1.16	1.68	0.62	0.65
	Multi-frequency	0.51	1.02	0.30	0.68	1.10	2.25	0.65	0.67
Present Experiments constant-steepness spectrum	2D	0.38	0.84	0.24	0.41	1.33	2.00	0.71	0.82
	3D Diffracting	0.39	0.84	0.24	0.45	0.74	1.80	0.69	0.80
	3D Focusing	0.41	1.26	0.27	0.52	1.34	2.60	0.70	0.86

In each geometric criterion, the left-hand column indicates parameter value at the onset of spilling. The right-hand column indicates the parameter value for the largest plunger breaker observed in that study.

+ The parameters are calculated with reference to mean water level (MWL), different from still water level (SWL) in all the others.

Table 2.2. Comparison of global spectrum-based wave steepness for breaking

Breaking type	Spectrum	Rapp & Melville (1990) 2D	Lamarre (1993) 2D	Chaplin (1996) 2D	Kway *et al.* (1998) 2D	Present Experiments 3D Diffracting	2D	3D Focusing
incipient wave	constant-amplitude	0.25		0.265				
	constant-steepness		0.35	0.30		0.36	0.32	0.21
spiller	constant-amplitude	0.30						
	constant-steepness		0.40		0.59	0.43	0.40	0.26
plunger	constant-amplitude	0.39			0.25			
	constant-steepness		0.45		0.73	0.66	0.50	0.47
	Pierson-Moskowitz				0.38			

Table 2.3. Comparison of energy loss per crest length due to breaking

Breaking type	Spectrum	Rapp &Melville (1990) 2D	Lammare (1993) 2D	Kway *et al.* (1998) 2D	Present Experiments + 3D Diffracting	2D	3D Focusing
plunger	constant-amplitude	25		22			
	constant-steepness		15	14	17 ± 2	16	32 ± 8
	Pierson-Moskowitz			20			
spiller	constant-amplitude	10		4			
	constant-steepness		8		9 ± 1	10	12 ± 3

+ The uncertainty of energy loss is due to the uncertainty of evolving breaking-crest length that is used to normalize the energy loss.

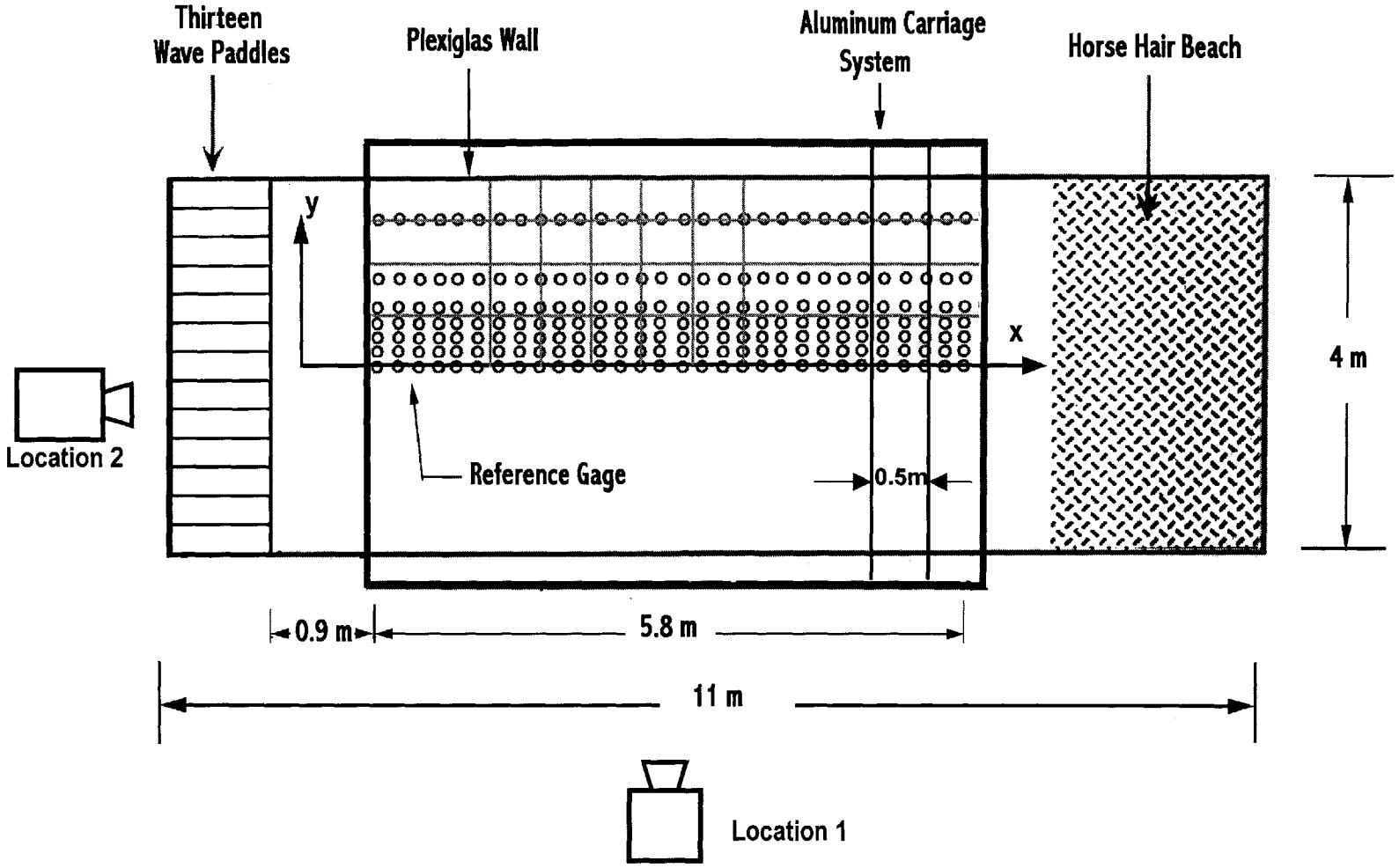

Figure 2.1. Top view of the test section. Circles indicate the locations of the surface displacement measurement. To verify the repeatability of waves for different runs, a reference wave gauge was kept at (x=120, y=0) cm. The CCD camera was positioned at location 1 (side view) and location 2 (back view). The gray lines correspond to the position of the reference grid constructed from 1cm ropes.

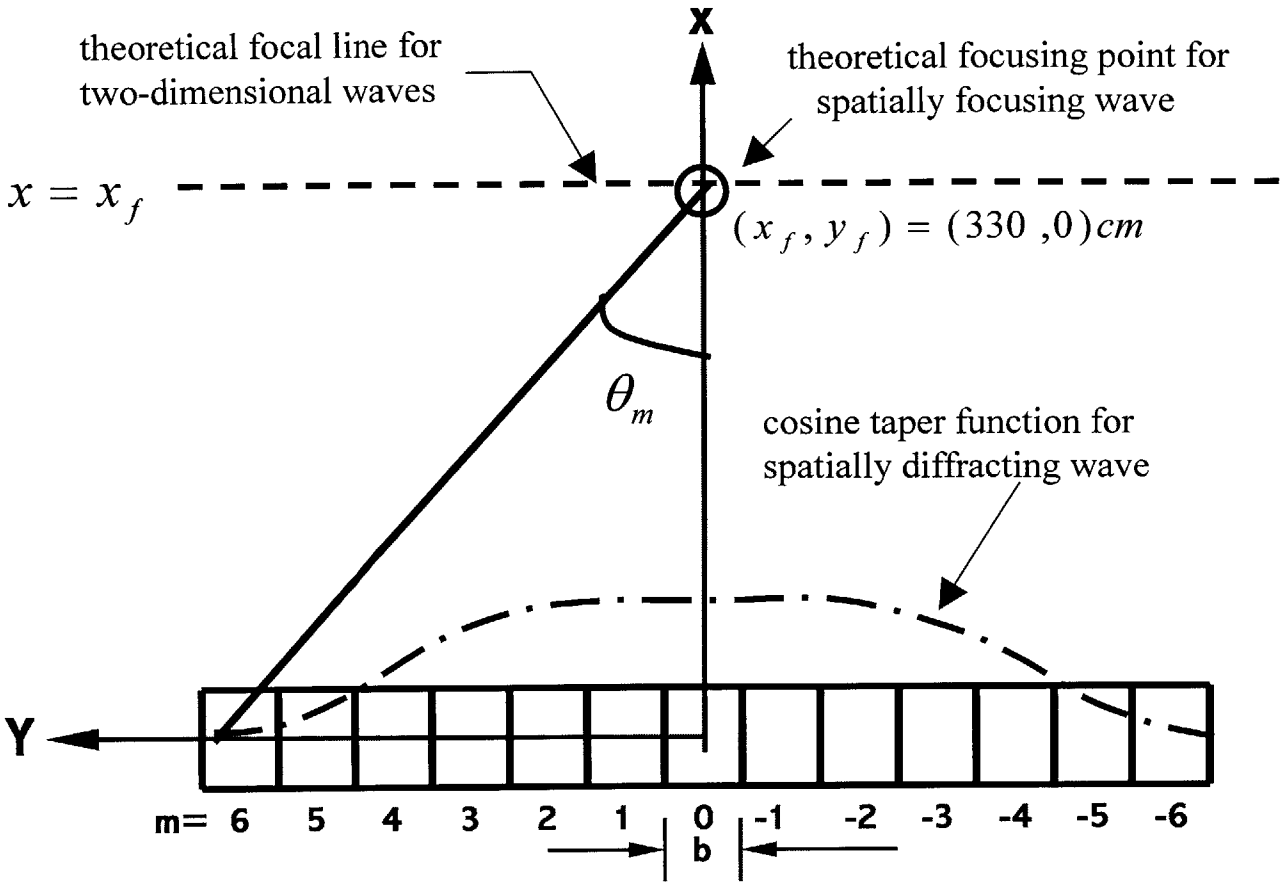

Figure 2.2. Schematic of thirteen paddles. The dashed line is the theoretical focusing line, $x = x_f$, for the two-dimensional wave. The circle at the centerline is the theoretical focusing point, (x_f, y_f),for the three-dimensional spatially focusing wave. The dot-dashed line is the cosine taper function for the three-dimensional spatially diffracting wave.

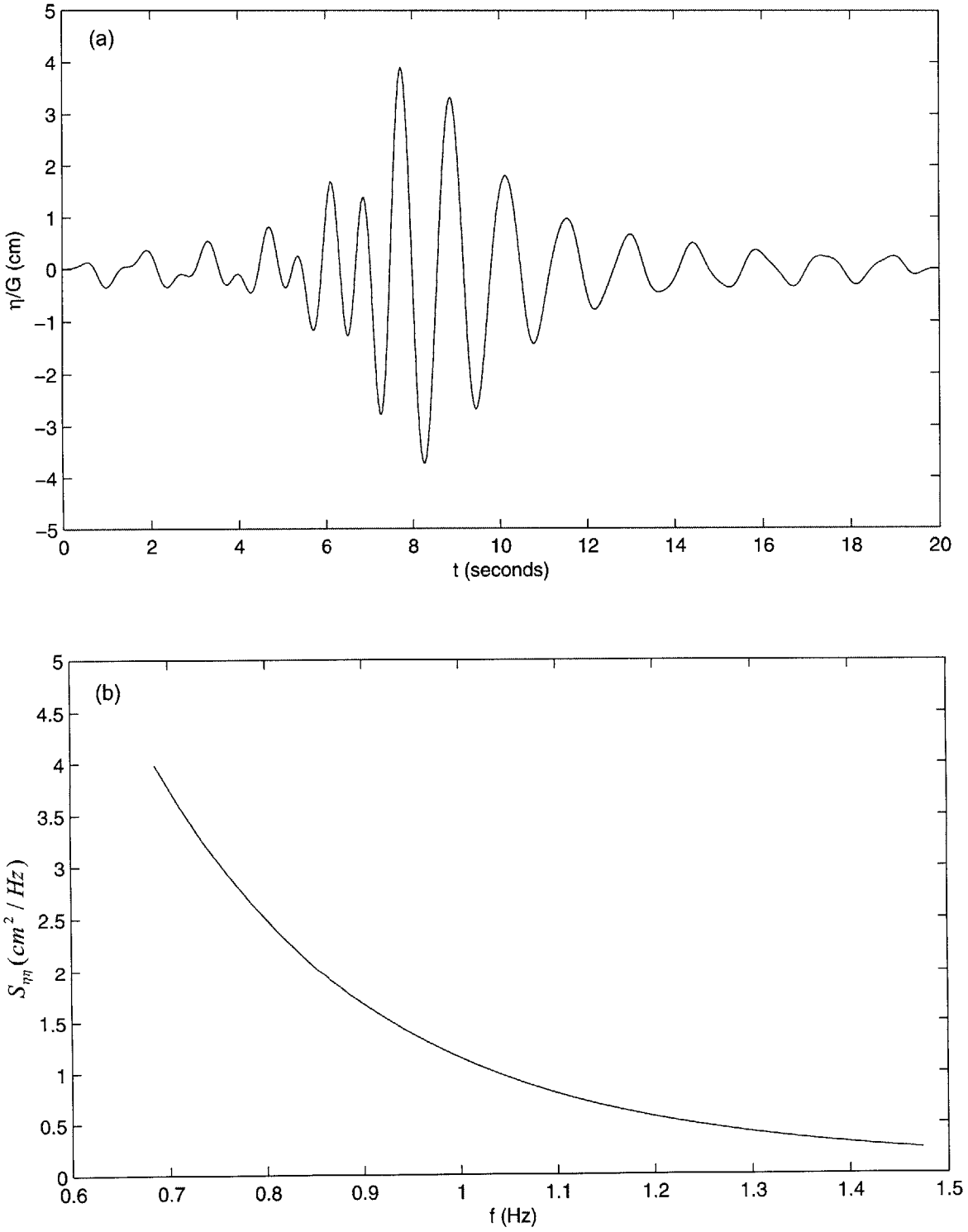

Figure 2.3. (a) Time series of input signals scaled by gain factor G. (b) Consant-steepness spectrum

(a) two-dimensional plunger

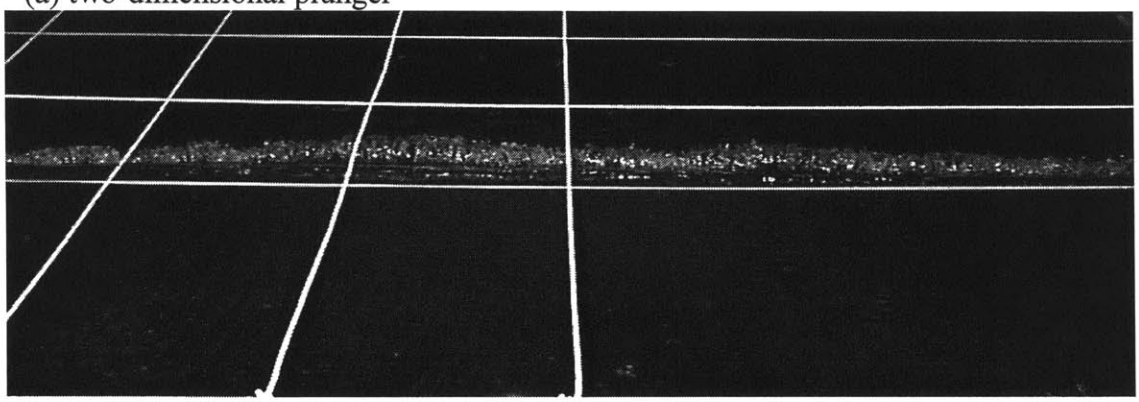

(b) spatially focusing plunger

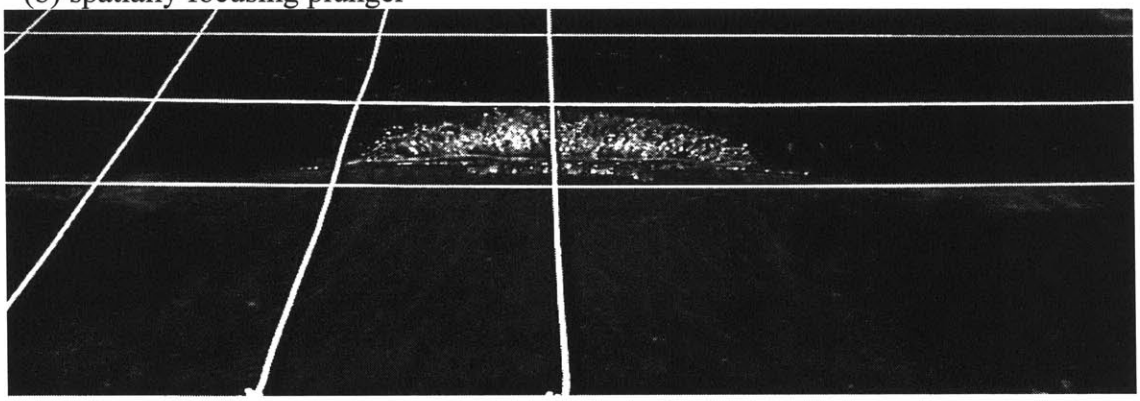

(c) spatially diffracting plunger

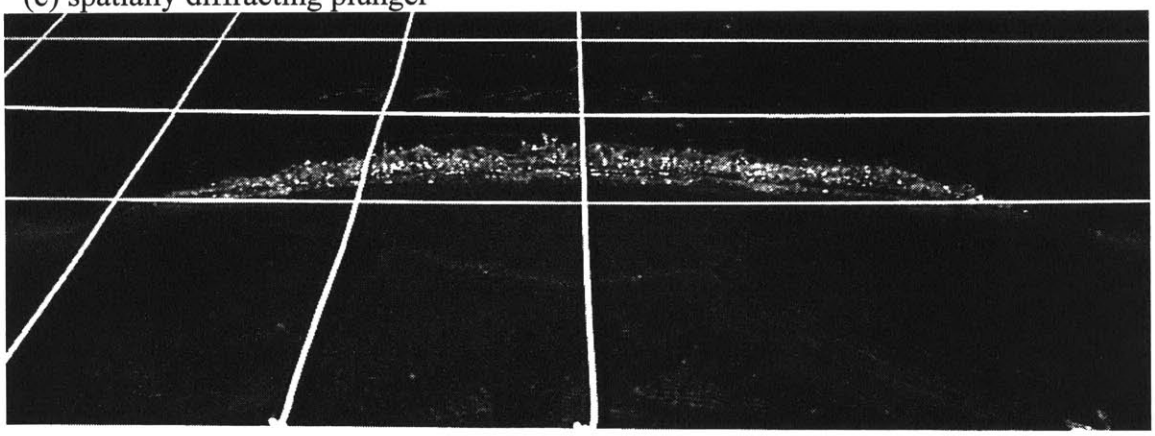

Figure 2.4. Photograph of plunging breaker taken at the camera location 2 (backview): (a) two-dimensional plunger, (b) spatially focusing plunger, and (c) spatially diffracting plunger. Each lateral grid interval on the photograph corresponds to 50 cm. Image contrast is enhanced to identify the whitecapping breaking regions.

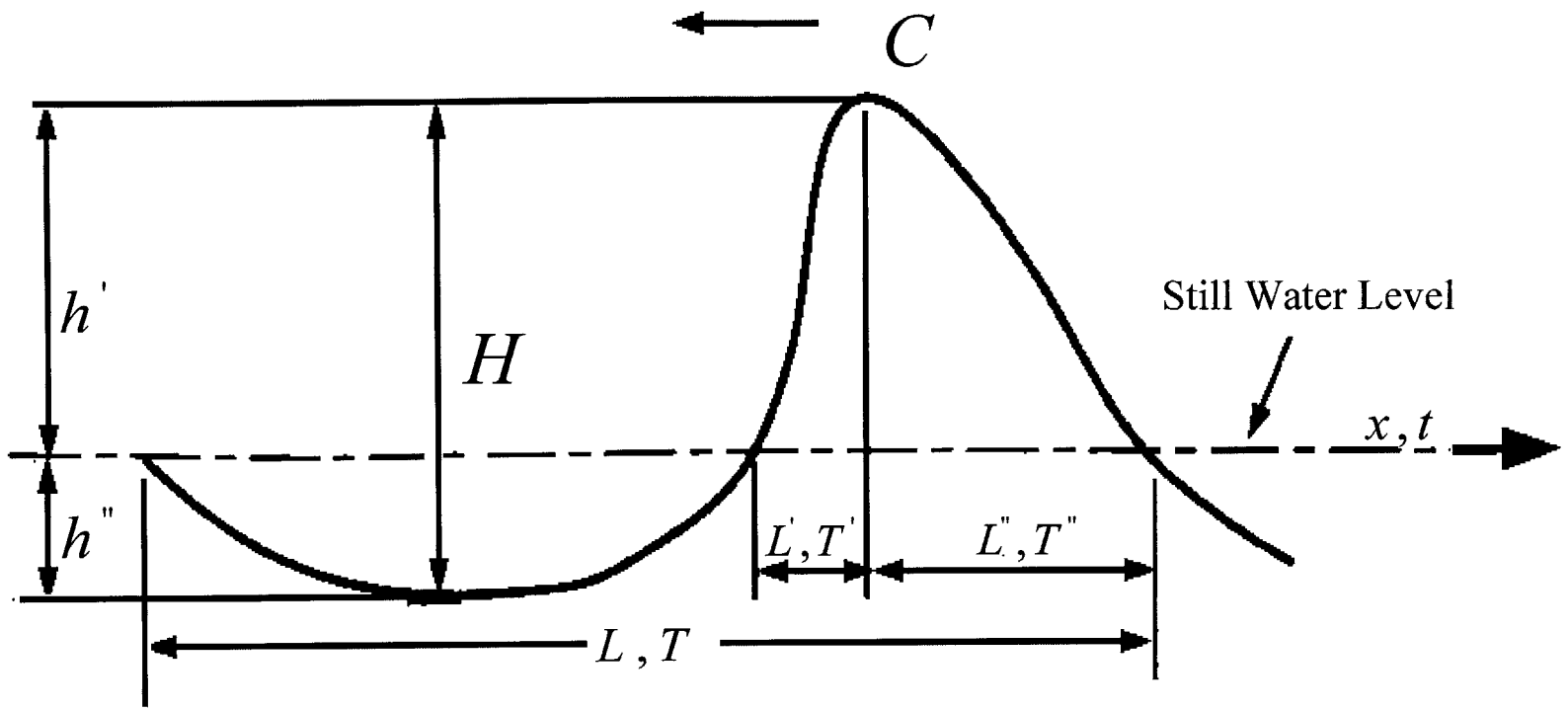

$$\varepsilon = \frac{\eta'}{L'} = \frac{\eta'}{(T'T'g/2\pi)} \qquad \delta = \frac{\eta'}{L''} = \frac{\eta'}{(T''T''g/2\pi)} \qquad \lambda = \frac{L''}{L'} = \frac{T''}{T'} \qquad \mu = \frac{\eta'}{H}$$

Figure 2.5. Definition of local wave parameters for steep asymmetric waves taken from Kjeldsen and Myhuang (1979). The crest front steepness ε and the crest rear steepness δ are used to characterize wave height steepness. The vertical asymmetry factor λ and the horizontal asymmetry factor μ are used to characterize crest asymmetry.

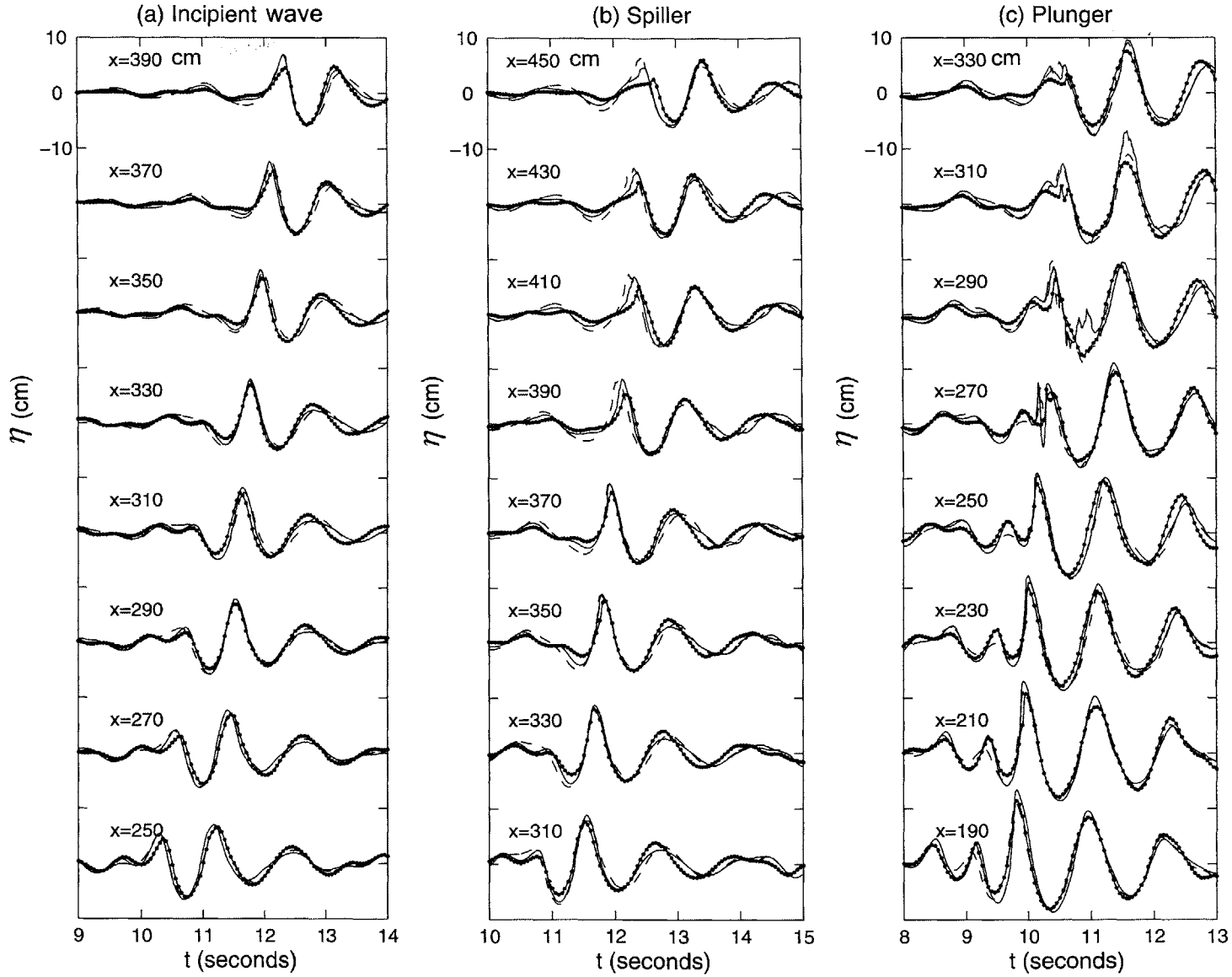

Figure 2.6. Surface displacement time series at the centerline, *i.e.* y=0 cm. The unit for x and η are in centermeters away from the mean position of the paddles and the still water level, respectively. The dashed lines, solid lines, and solid lines with dot correspond to two-dimensional, three-dimensional spatially focusing, and three-dimensional spatially diffracting waves, respectively: (a) incipient wave (b) spiller and (c) plungers.

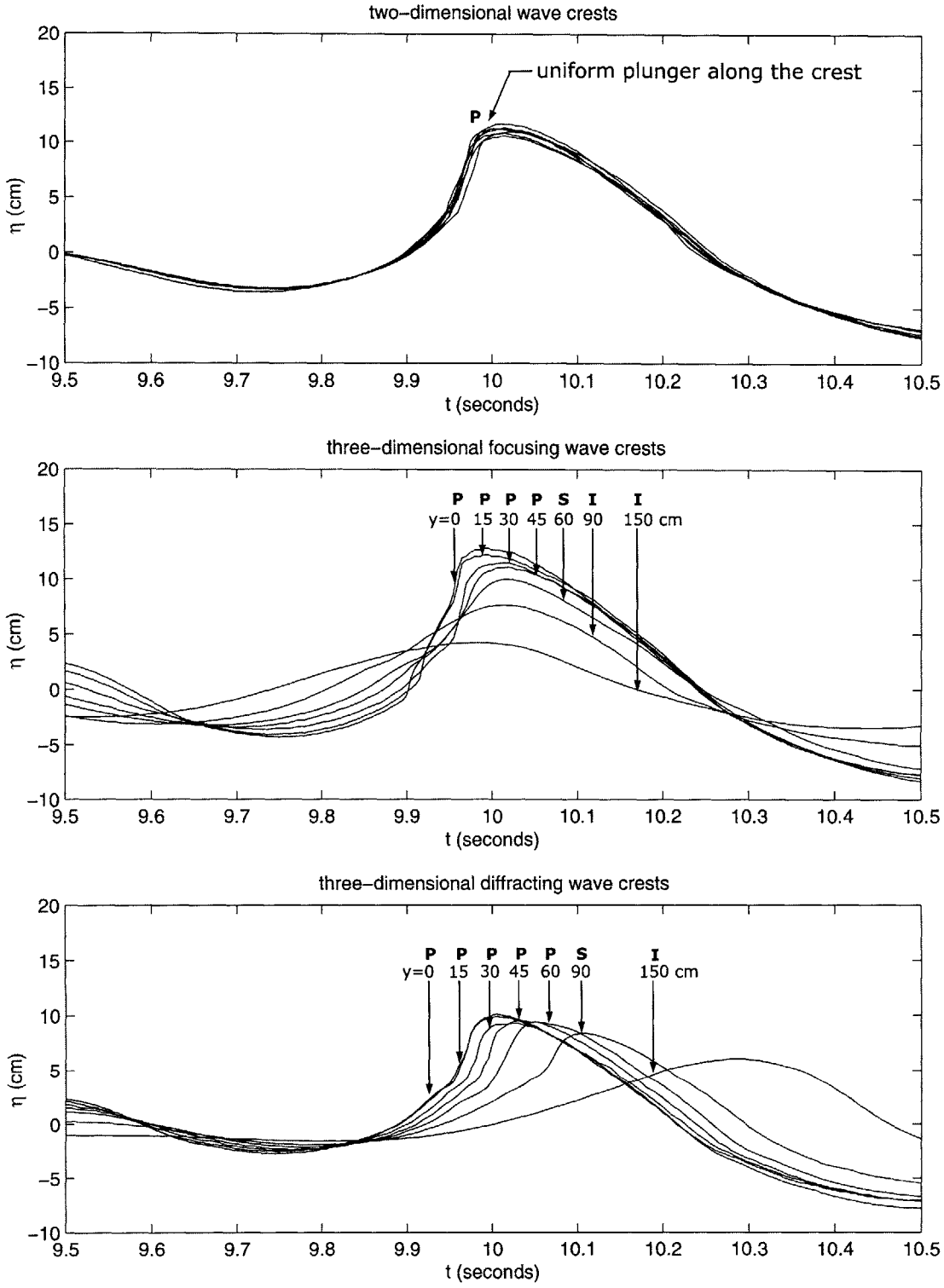

Figure 2.7. Comparison of surface displacement across the test section at x=230 cm (the onset of plunging breaker). While the lateral wave crests of the two-dimensional plunger were uniform, the lateral wave crests of three-dimesional focusing and diffracting waves showed pronounced variation and consisted of a composite intensity of breaking, i.e. (P)lunger, (S)piller and (I)ncipient wave, which are marked in each graph.

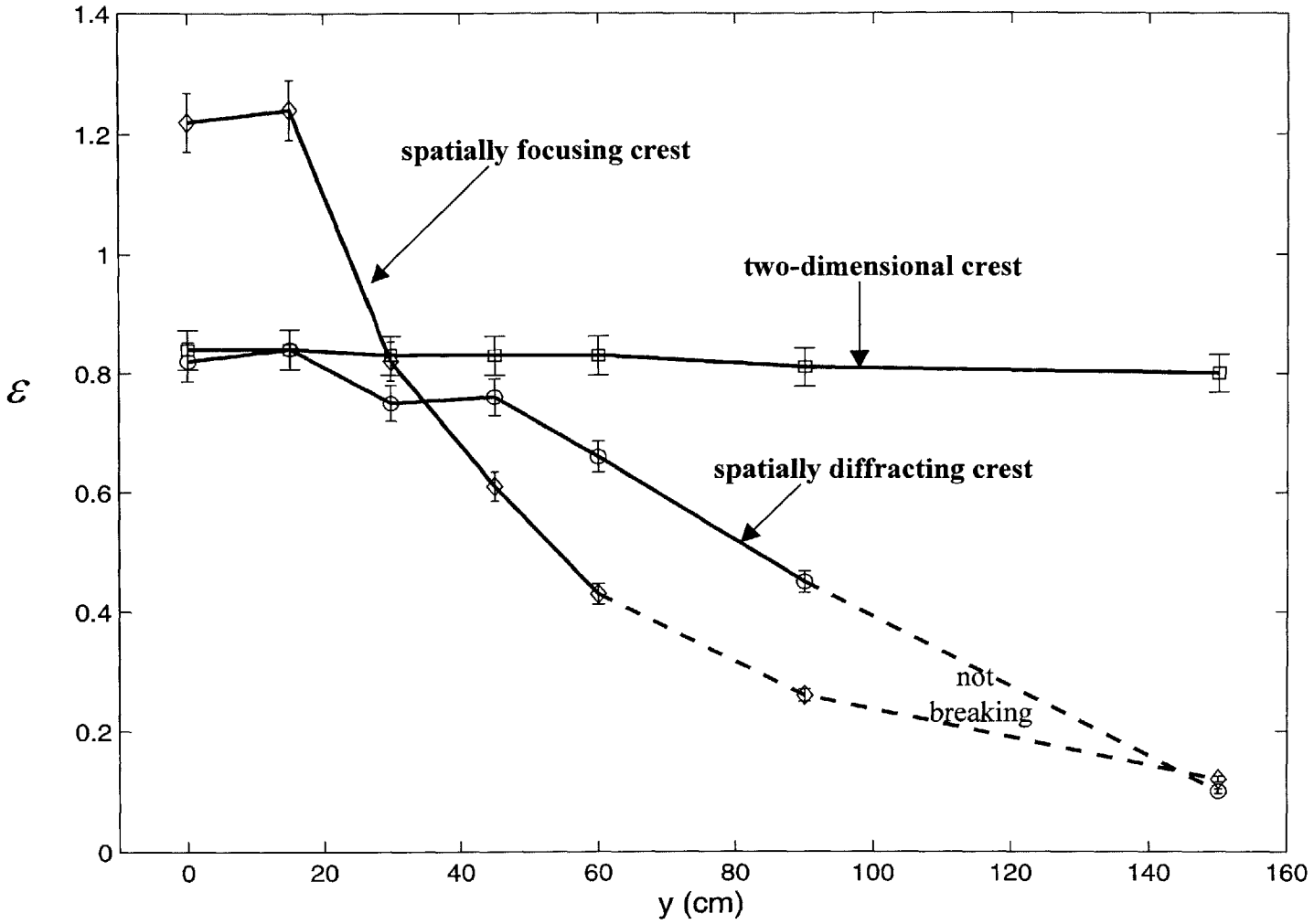

Figure 2.8. Crest front steepness at the onset of plunging breakers. The solid (dashed) lines correspond to the regions where breaking (does not) occurs.

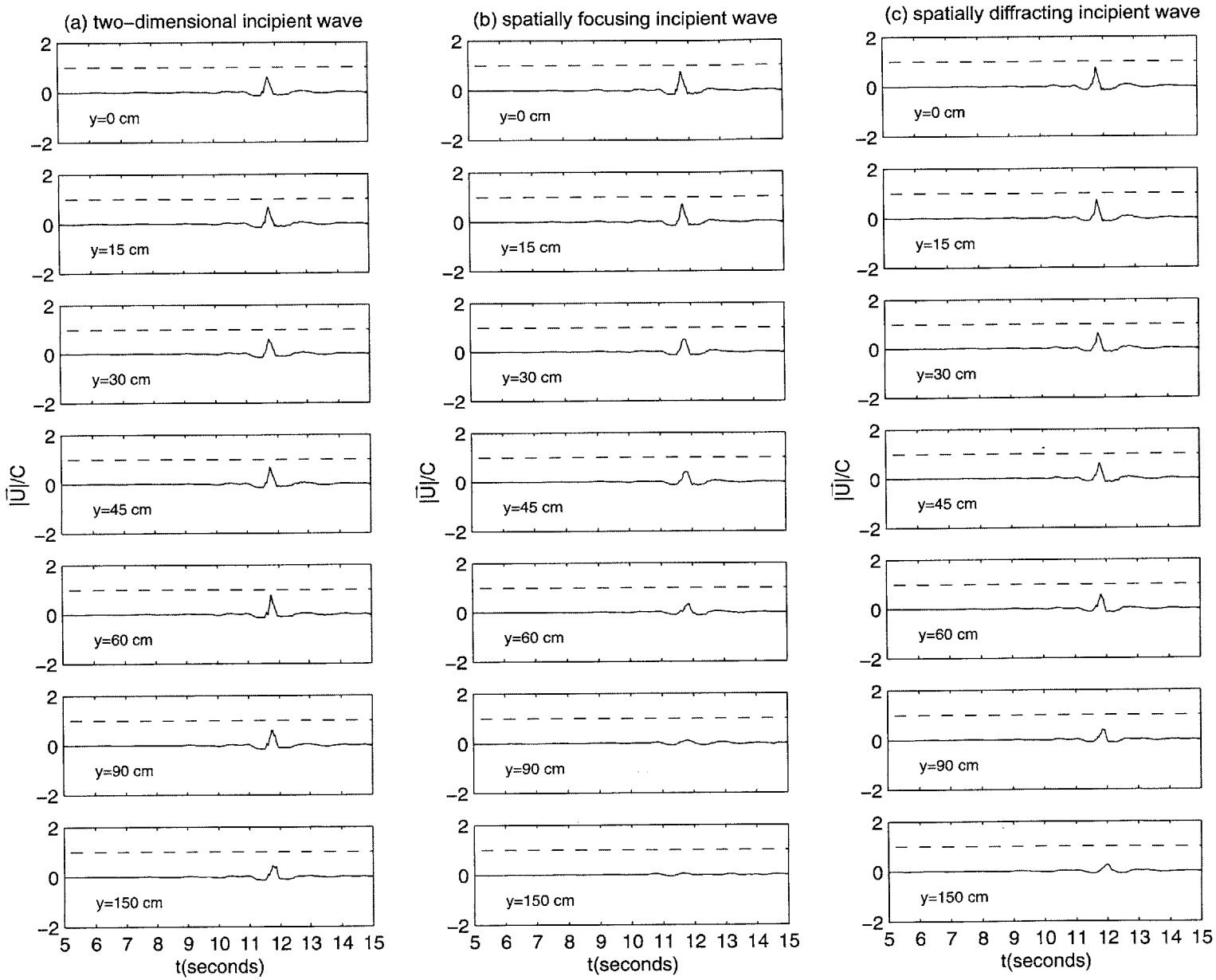

Figure 2.9. Ratio of particle velocity $|\bar{U}|$ and phase speed C at x=330 cm for (a) two-dimensional incipient wave, (b) spatially focusing incipient wave, and (c) spatially diffracting incipient wave. The lateral position y is given in the lower left of each graph. The dashed line is the threshold value of the kinematic breaking criterion where $|\bar{U}|/C=1$. As shown in each graph, the ratio doesn't exceed the threshold value, indicating no breaking event.

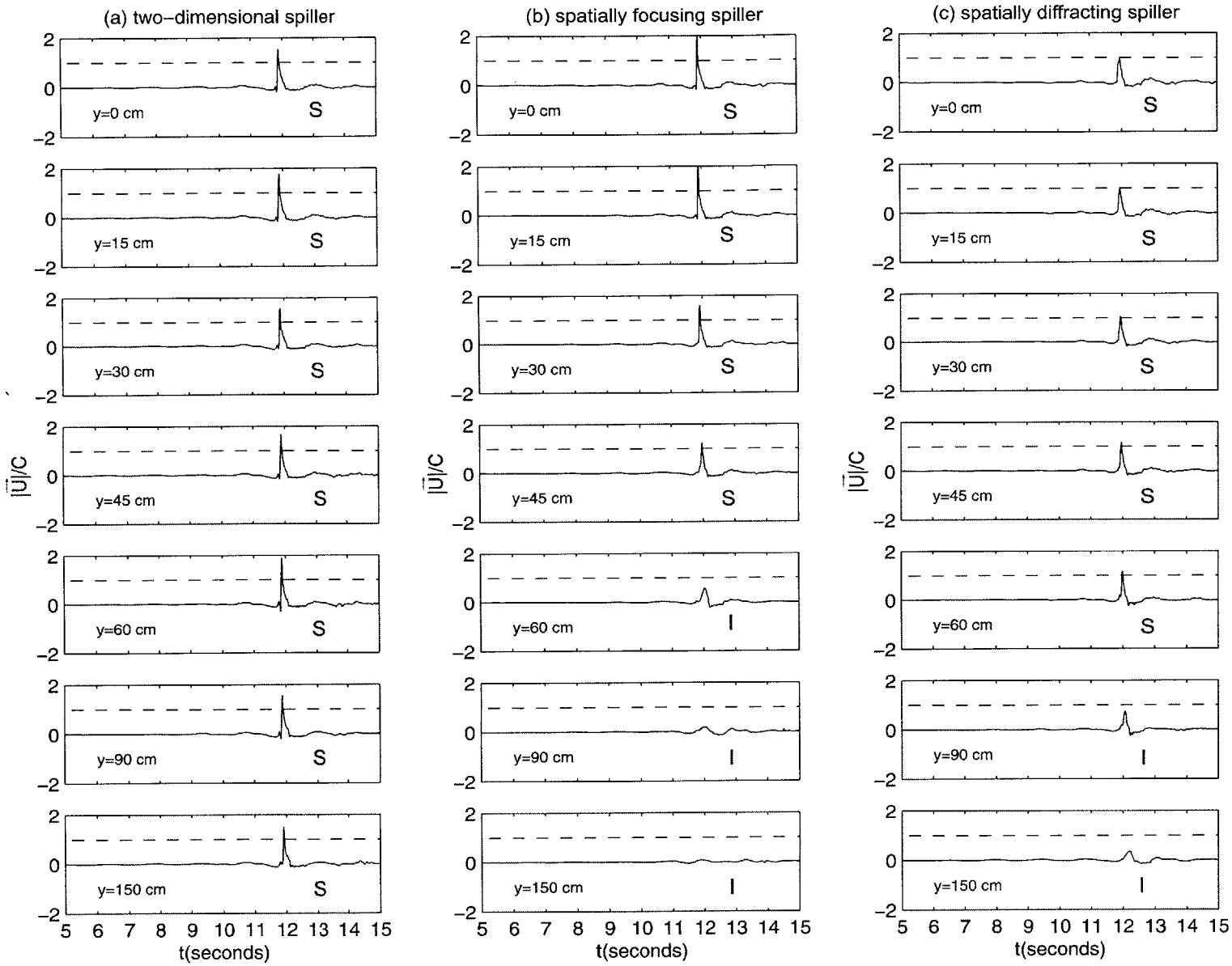

Figure 2.10. Ratio of particle velocity $|\bar{U}|$ and phase speed C at x=370 cm where (a) two-dimensional spiller, (b) spatially focusing spiller, and (c) spatially diffracting spiller start to occur. The lateral position y is given in the lower left of each graph. The dashed line is the threshold value of the kinematic breaking criterion where $|\bar{U}|/C=1$. The letters, 'S' and 'I', in each graph correspond to the spiller and incipient wave on video observations.

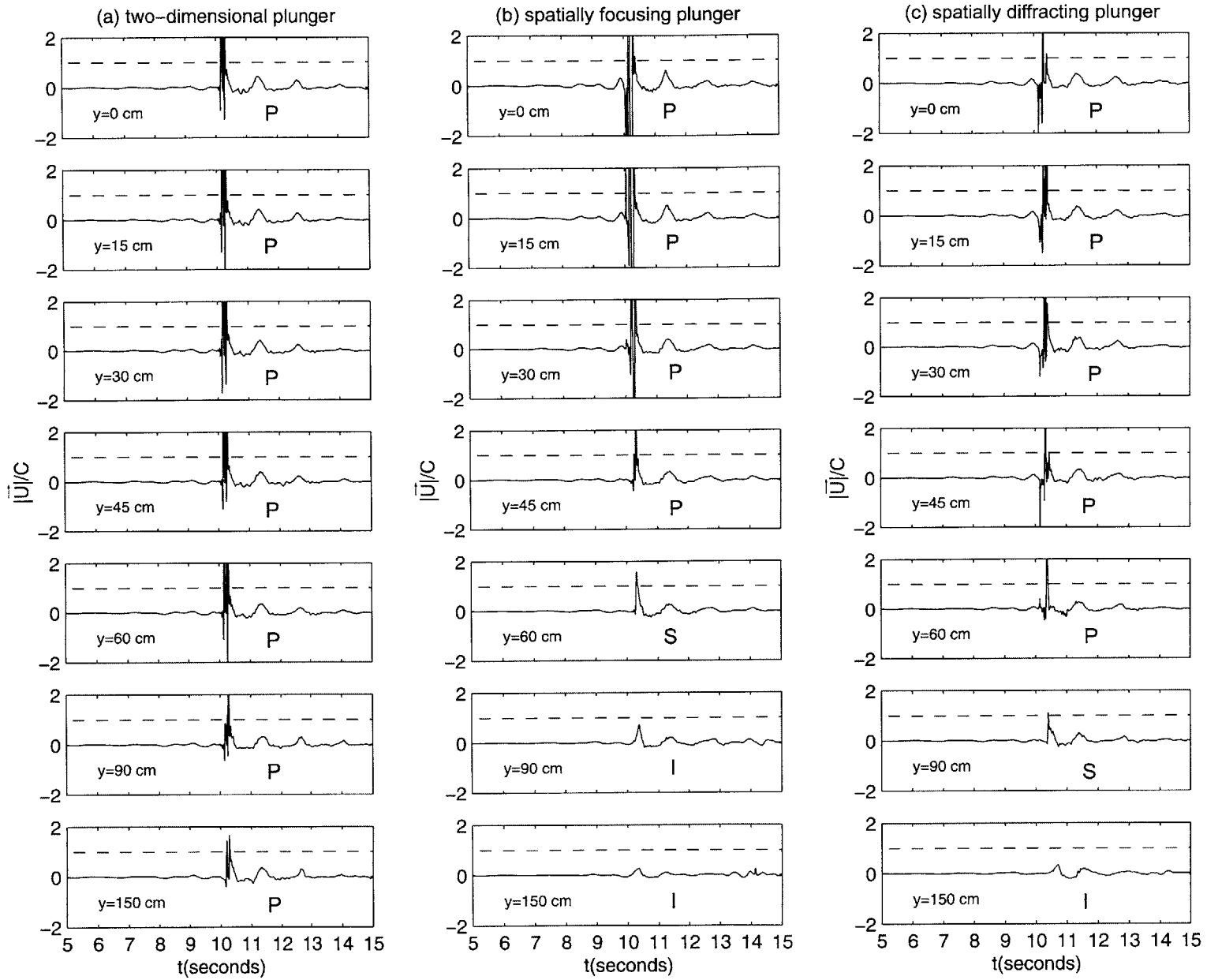

Figure 2.11. Same as Figure 2.10 but at x=270 cm where the (a) two-dimensional plunger, (b) spatially focusing plunger, (c) spatailly diffracting plunger occur. The letters, 'P', 'S' and 'I', in each graph correspond to the plunger, spiller, and incipient wave on video obervations. Note that some ratios are below zero, which may result from the splashing.

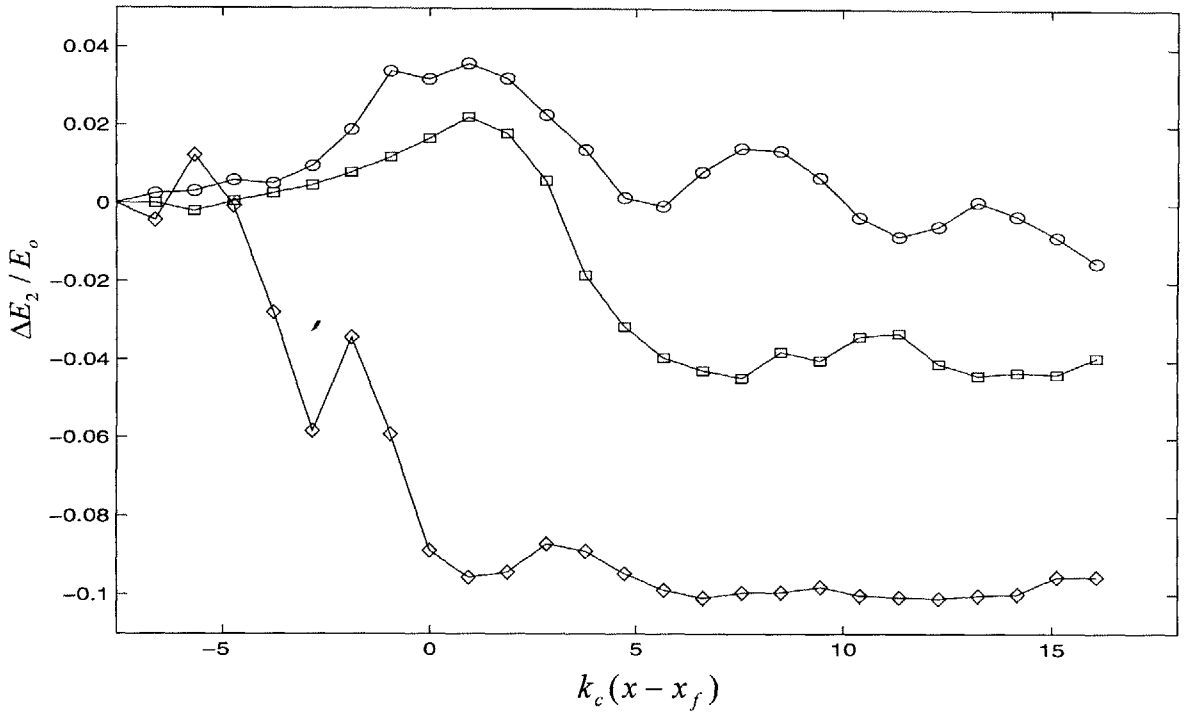

Figure 2.12. Evolution of E_2 spatially focusing plunger (◇), spiller (⊟), and incipient wave (⊖) at the centerline, i.e. y=0 cm. Note that the ΔE_2 is the difference of higher harmonic band energy with reference of x=170 cm. E_o is the total initial wave energy within each wave packet.

Chapter 3: Surface Current and Vorticity Induced by Three-Dimensional Wave Breaking

3.1 Introduction

One of the important processes associated with wave breaking is the transfer of momentum from the surface wave field to surface currents with a significant rotational component (Banner and Peregrine 1993, Meza *et al.* 1999). The breaking-induced currents and vorticity are significant to physical, chemical, and biological processes occurring in the upper ocean and across the air-sea interface (Thorpe 1995, Melville 1996). It is well known that oceanic wave breaking is a three-dimensional (3D) phenomenon (Csanady 1990). As suggested by Thorpe (1995), the breaker-induced currents should also be strongly three-dimensional. The research described here reveals this three-dimensional structure through detailed velocity measurements of a three-dimensional, deep-water, breaking event.

Over the last two decades, the study of two-dimensional (2D) breaking has been very active and successful. An excellent review of breaker-type classification, the mechanisms of wave breaking, and the evolution of wave geometry is given by Peregrine (1991) for shallow-water waves and by Banner and Peregrine (1993) and Melville (1996) for deep-water waves. The most comprehensive laboratory study of 2D wave breaking is that of Rapp and Melville (1990), who described the breaker-induced surface current, turbulence, surface mixing, surface motions, momentum fluxes, and energy dissipation. They observed initial breaker-induced surface currents of $0.02\sim 0.03C$, which took 60 wave periods to decay to $0.005C$, where C is the characteristic phase speed. Recently, Perlin *et al.* (1996) and Chang and Liu (1998) measured the vorticity field beneath 2D

breaking using particle imaging velocimetry (PIV). Numerical simulations of 2D plunging have progressed from descriptions of evolution before breaking (Longuet-Higgins and Cokelet 1976, Dommermuth *et al.* 1987, Skyner 1996) to more powerful models that can describe the plunging-jet impact and splash-up (Lin and Liu 1998, Chen *et al.* 1999).

While significant insight now exists for 2D breaking, much less progress has been made in the description of 3D breaking, except at the pre-breaking stage. The effects of three-dimensionality on deep-water, breaking criteria have been examined in laboratory (She *et al.*1994, 1997, Kolaini and Tulin 1995, Nepf *et al.*1998) and field studies (Holthuijsen 1986). Numerical descriptions of breaking onset are now feasible (Xü and Yue 1992, Miyata *et al.* 1996), but the full computation of strongly nonlinear, viscous, three-dimensional, breaker evolution remains a challenging issue (Tsai and Yue 1996).

Some observations of post-breaking structure have been made by Su *et al.* (1984), who photographed bubble streamers left by 3D breaking waves that suggest the presence of vertical vorticity near the edges of breaking crests. Csanady (1994) presented a conceptual model of the flow induced by a finite-length breaker that included similar zones of vertical vorticity. He further showed that streamwise vorticity could be generated through the interaction of the induced mean flow and Stokes drift. Thorpe (1995) also conjectured that short-crested, deep-water plunging would induce non-uniform currents with vertical vorticity. More recently, Peregrine (1998, 1999) described the vorticity generated by short-crested breaking in both shallow and deep-water conditions. In this study the detailed measurements of the induced current and vorticity

fields generated by a 3D breaking are explored in a laboratory wave basin. Our observations support the conceptual models described above.

3.2 Experimental Methods

The study was conducted in a 4 m x 11 m test section (Figure 3.1) within the Gunther Family Three-dimensional Wave Basin at the Massachusetts Institute of Technology. The mean water depth was 0.6 m. The test section contained thirteen hydraulically driven wave-makers controlled by a central computer. A coordinate system was chosen with x as the streamwise (wave propagation) direction and x = 0 at the mean paddle position; y as the lateral direction and y = 0 at the mid-point of test section; and z as the vertical direction and z = 0 at the mean water level. A wooden framed beach with a slope of 1:5 and covered with 10 cm of multi-layered horsehair material was used to reduce reflection at the end of the test section. The beach reflection coefficient for the multi-frequency wave-packets was less than 5 % (Nepf *et al.* 1998 and Wu and Nepf 1999).

The 2D unsteady breaking was generated by moving the thirteen paddles in unison to produce a wave packet of 32 frequency components that focused at a specified line, x_f = 330 cm , and time, $t_f = 12$ seconds (Greenhow and Vinje 1982). The packet spectrum was constructed based on constant-steepness. With a central frequency of $f_c = 1.08$ Hz and bandwidth of 0.789 Hz, all of the wave components satisfied the deep-water wave condition and the corresponding central wave number was $k_c = 4.72m^{-1}$. The 3D, short-crested, unsteady breaking waves were generated by varying the phase at each paddle so that the 32 wave components focused at a specified

point (x_f, y_f) = (330,0) cm. Further details of the wave generation technique can be found in Chapter 2.

The 3D plunger evolved as follows. As the wave components began to focus the profile of the wave crest became increasingly asymmetric, with the asymmetry most severe at the centerline (*i.e.*, $y = 0$), and decreasing away from the centerline (Figure 2.7). Subsequently, the front face of the central wave crest steepened, and a jet of water projected forward in an overturning motion. The central jet plunged back into the wave surface at $x_o \approx 270$ cm, creating the fan of splash-up visible in Figure 3.2. Away from the centerline (*i.e.*, $y \geq 90$ cm), the wave crest steepened without breaking (Figure 3.2). The height of the splash-up exceeded the height of the original plunging crest. The splash fan fell roughly one-third the characteristic wavelength, *i.e.* $1/3\, L_c (= 2\pi / k_c)$, downstream from the plunge point, x_o.

The velocity field was recorded using an array of three acoustic Doppler velocimeters (ADVs) and a digital particle image velocimetry (DPIV) (see Figure 3.1). The ADV has been widely used in measuring mean and turbulence flow (Kraus *et al.* 1994, Nikora and Goring 1998, Voulgaris and Trowbridge 1998). It measures three components of velocity of particles traveling through a 0.25 cm^3 sampling volume located 5cm below the probe head. In this study, near-neutrally buoyant, spherical, hollow particles with density 1.062 g/cm^3 and diameter 11.4 micron were used to seed the flow. To achieve a signal-noise ratio above 20 dB, these particles were well mixed and maintained at a concentration of 70 mg/l. The resolution of the ADVs was 0.25 cm/s with a velocity bias of 0.25%, consistent with the manufacturer's specification (Lohrmann et al. 1994). The array of the three ADVs was held by a moving aluminum carriage

system. Prior to the experiments, the orientation of each ADV was carefully aligned with our prescribed coordinate system.

The test section consisted of 324 grid positions with 20 cm longitudinal spacing from x=270 to 430 cm, lateral positions at y=0, 15, 30, 45, 60, 90 cm, and the vertical positions at z = -7, -10, -15, -20, -30, -50 cm (Figure 3.1). To obtain the representative unsteady mean and turbulent flow induced by the breaking waves, 10 repeatable runs were made at each grid position. During each run the velocity was sampled at 30 Hz for 50 seconds with the breaking event occurring at $t_o = 10.5$ seconds. The ensemble-averaged values estimated from 10 and 20 runs agree to 95% such that 10 runs were deemed sufficient for characterizing the velocity. For each 2D and 3D breaking wave, 1080 runs were needed to scan the entire measurement area. Between each run 20 minutes were required to settle the basin and removed the residual motion from previous run. To examine the repeatability between runs, a reference wave gage at (x, y) = (180,0) cm was used to record surface displacement. The standard deviation of this reference measurement was less than 1% over the entire set of experiments. The ADVs and the reference wave gage were also synchronized to the wave-maker system by an external analog triggering. Finally, using paired measurements, *i.e.* $y = \pm 30$ cm, the velocity field for non-breaking waves was shown to be symmetric across the centerline

To examine the surface drift and vorticity induced by breaking, the velocity was processed in the following manner. First, spurious measurements that occurred when the sampling volume of the ADV came out of the water were removed. The velocity records were then analyzed following a method proposed by Rapp and Melville (1990). The ensemble mean velocity was obtained by averaging 10 experimental runs, *i.e.*

$$< q(x,y,z,t) >= \frac{1}{10}\sum_{n=1}^{10} q_n(x,y,z,t)\,, \tag{3.1}$$

where $q(x,y,z,t)$ can be any velocity component $u(x,y,z,t)$, $v(x,y,z,t)$, or $w(x,y,z,t)$ in the prescribed x, y and z direction. The ensemble mean consists of contributions from carrier waves q_{cw}, a forced long wave q_{fw}, and the induced current q_{ic}, *i.e.*

$$< q(x,y,z,t) >= q_{cw} + q_{fw} + q_{ic}\,. \tag{3.2}$$

To remove the carrier waves from the ensemble mean, a Chebyshev Type II low-pass filter with passband frequency 0.3 Hz and stop-band frequency edge 0.4 Hz was performed. This low-pass filter has the advantage of being monotonic in the pass-band and maintaining 60 dB attenuation for ripples in the stop-band, which results in an estimated error of 0.1 %. Because the wave-packet used to generate the breaking event is transient, the forced wave (bound long wave) is also time dependent and should not be misinterpreted as the time-independent Stokes drift (Baldock *et al.* 1996). Once the wave-packet passed by, the backward forced wave should disappear within the test section, leaving only the induced current due to breaking (Rapp and Melville 1990). Finally, The induced current field was used to determine the induced vorticity, defined as

$\omega_x = \frac{\partial w_{ic}}{\partial y} - \frac{\partial v_{ic}}{\partial z}$, $\omega_y = \frac{\partial u_{ic}}{\partial z} - \frac{\partial w_{ic}}{\partial x}$, and $\omega_z = \frac{\partial v_{ic}}{\partial x} - \frac{\partial u_{ic}}{\partial y}$ in the longitudinal, lateral, and vertical directions, respectively.

Both the resolutions of the ADV scan and the ensemble averaging may limit the observation of maximum, instantaneous vorticity produced in the post-breaking wake. In order to assess the instantaneous vorticity at a smaller scale, an additional observation of the velocity field was made using a DPIV system. This system consisted of the following components. A SMD-1M60 digital CCD camera (1024 x 1024 pixel, 30 Hz and 12 bits-per-pixel) was mounted above the test section. A 24-mm lens with a 1-mm extension tube was used to image a 65 x 65 cm^2 area in the $x-y$ horizontal plane located ten centimeters below the mean water surface (Figure 3.1). This horizontal plane was illuminated by a 2-cm thick light-sheet generated by a 6 watt, Argon Ion laser beam (Coherent INNOVA 70) directed through a Dantec 9060 fiber optic which included a cylindrical front-face lens to spread the beam into a sheet. A mechanical shutter (Laser Products, Inc., model LS500F) was placed between the laser source and fiber optic to enable shuttering of the light source. Each frame was integrated 35 ms (28.57 Hz) and the shutter exposed each image 10 for ms.). The facility was seeded with particles with mean diameter 250 micron and specific gravity nominally 0.8. A 300 MHz Pentium II computer with dual processors and 512 Mb SDRAM was used for image recording. The National Instruments Labview program was used to coordinate the wave-maker system, the mechanical shutter and the camera framing rate. A total of 210 images corresponding to 7.35 seconds were acquired after the breaking event. The images acquired by the CCD camera were then analyzed using digital particle image velocimetry (DPIV), as described

in Cowen & Monismith (1997). Note that near the point of breaking large free surface curvature can distort images on the horizontal measurement plane so that the estimated velocity field would not be reliable. In addition, thee DPIV is not effective in regions of high-density air bubbles, as generated by breaking waves (White 1996, Chang and Liu 1998). To avoid these sources of error, the velocity field was only estimated from the images occurring 5 seconds or more after the breaking event for which the surface curvature and bubbles density were unimportant.

3.3 Results

The spatial-temporal evolution of the induced mean velocity due to breaking is shown in Figure 3.3 for the 2D plunger and in Figures 3.4, 3.5, and 3.6 for the 3D plunger. For the 2D case the current is uniform across the test section so that only the lateral plane y = 45 cm is shown here. Five wave periods after breaking, *i.e.* $(t-t_o)f_c = 5$, the wave group has passed the test section and a large eddy, centered at x = 340 cm, is left behind (Figure 3.3.a). A positive horizontal current is induced near the surface and a negative sub-surface flow is induced below $z = -30$ cm. The magnitudes of the initial surface velocity and subsurface flow are $0.06C$ and -0.02C, respectively (C is the characteristic phase speed and is defined as $f_c / k_c = 144$ cm/sec). The horizontal induced velocity at each end of the test section, *i.e.*, $x = 290$ and 430 cm, is small, suggesting that the length-scale of breaking influence is of the order of the characteristic wavelength, $L_c = 133$ cm. Ten wave periods after breaking, *i.e.* $(t-t_o)f_c = 10$, the region of elevated surface current has propagated downstream, but has still not penetrated below 20 cm depth (Figure 3.3b). Finally, thirty wave periods after breaking, the surface

and subsurface currents decay to $0.01C$ and -0.005C, respectively (Figure 3.3c). The above observations are consistent with those made by Rapp and Melville (1990) who used a constant-amplitude spectrum in contrast to the constant-steepness spectra used here. This suggests that surface drift induced by breaking is not sensitive to spectral shape of wave packet.

Figure 3.4 shows the velocity induced by the 3D plunger at the center plane, *i.e.* $y = 0$ cm. At $(t - t_o)f_c = 5$ (Figure 3.4a), the initial surface current is $0.12C$, twice that observed in the 2D plunger with the comparable amplitude. In addition, the surface current penetrates to 30 cm, which is deeper than observed for the 2D case. A negative current is induced at z = -50 cm, with a maximum value (-0.02C) between $x = 330$ to 370 cm. By ten wave periods after breaking (Figure 3.4b), the positive surface current has penetrated to z = 50 cm, which is more than twice the penetration achieved by the surface current induced by the 2D breaker. Finally, at $(t - t_o)f_c = 30$ the induced current has decayed to $0.02C$, and is positive everywhere on the centerline of the test (Figure 3.4c).

To examine the three-dimensionality of the short-crested behavior, we investigate the induced velocity at the lateral planes y = 45 cm (Figure 3.5) and y = 90 cm (Figure 3.6). Because the intensity of breaking is smaller at y = 45 cm, weaker currents are generated in this plane. After five wave periods (Figure 3.5a), a positive horizontal current, $0.02C$, is observed near the surface and a negative current, $-0.01C$, is observed below $z = -20$ cm. By $(t - t_o)f_c = 30$ the induced surface and bottom currents have decreased to $0.005C$ and -0.003C, respectively (Figure 3.5c). It is interesting to note

that the pattern of the induced velocity produced at y = 45 cm by the 3D plunger resembles that of the 2D plunger. At the edge of the breaking crest (y = 90 cm, Figure 3.6a) only a very thin surface current of $0.01C$ is generated, penetrating less than ten centimeters. Below this depth the induced current is negative with a magnitude of $-0.01C$. By ten wave periods after breaking the induced horizontal current nearly everywhere negative in this plane, and persist to the thirty wave period time mark (Figure 3.6c). Together with the positive induced currents observed at the centerline, this implies the presence of strong vertical vorticity, a pattern entirely absent from the two-dimensional breaker.

The above observations agree with the flow patterns conjectured for a 3D breaker (Thorpe 1995, Peregrin 1999). Specifically, the short-crested breaker generates a laterally non-uniform surface current, in contrast to the uniform current induced by a 2D breaker (Thorpe 1995). In addition, the short-crested plunger creates horizontal circulation (Figure 3.7) consisting of a positive current at the center-line and a negative current at $y = 90$ cm. The circulation is stronger and broader $z = -10$ cm (Figure 3.7a and c), than at $z = -30$ cm (Figure 3.7 b and d), indicating that the circulation decays away from the surface. Following Peregrine's (1999) conceptual description of circulation generated at the lateral boundaries of deep-water breaking-crests, we suggest that the circulation observed arises from the finite length of the breaking crest.

Note that similar circulation patterns may result from a pair of steady, phase-locked, obliquely traveling, progressive waves (Iskandarani and Liu 1991), and that the spatial focusing technique used in this study includes transient elements of this wave pattern. By considering the incipient wave condition, however, we conclude that this

wave-wave interaction is not significant in producing the circulation we observed post-breaking. Specifically, no comparable circulation pattern occurs after the passage of the incipient wave. The induced velocity observed for the incipient wave, whose wave height is one-half that of the plunger, is two orders of magnitude smaller than that of the plunger. This comparison suggests that the circulation observed after breaking is principally generated by the breaking impact, and not by the wave packet alone.

To quantify the strength of the circulation observed in the induced current, we calculate the vorticity field using a first-order finite difference approximation, and linear interpolation between the grid spaces. Figure 3.8 shows the resulting vorticity field induced by the 3D plunging breaker. Three regions of significant vorticity are generated by the breaking event. First, a large, sub-surface region of positive vorticity (centered at $y = 0$ cm, $x = 340$ cm in Figure 3.8a) results directly from the penetration of the plunging jet. The lateral extent of this vortex is limited to $\approx \pm 30$ cm. Because vortex lines cannot terminate in the body of a fluid, the vortex tube must tilt upward at the flank of the breaker to connect with the surface (Csanady 1994, Thorpe 1995). The point of connection is apparent in the map of vertical vorticity (Figure 3.8c), specifically the region of positive vertical vorticity centered at $x = 340$ cm and extending lateral to $y = 30$ cm. This reconnection does not occur for the 2D breaker, as the vortex tube simply terminates at the side boundaries. Taking symmetry at the centerline, the regions of lateral and vertical vorticity suggest a U-shaped vortex tube that penetrates to a depth of 40 cm, and spans 60 cm between its two surface connections. At $(t - t_o)f_c = 5$ the vorticity of this jet-vortex is comparable to the central wave-packet frequency, f_c. At $(t - t_o)f_c = 10$ (Figure 3.8b), the vortex tube has migrated with the mean current to $x =$

380 cm, and penetrates to 50 cm, which is twice the penetration depth observed for the two-dimensional breaker. Its strength has decayed to $0.3 \sim 0.4 f_c$.

A second region of positive vorticity is generated at the surface and downstream of the plunge point, between $x = 380$ cm and 430 cm (Figure 3.8a). This region of vorticity extends laterally to $y = 90$ cm, a region that corresponds to the splash fan. After five wave periods the centerline vorticity is comparable to the center wave-packet frequency, *i.e.* f_c. Away from the centerline, the strength and vertical penetration of this surface vorticity layer diminishes as the breaker becomes weaker and turns into a spiller. As with the larger, sub-surface vortex, this broader vortex line must also connect with the surface. In doing so, it generates a mild vertical vorticity, $\omega_z \approx 0.2 \sim 0.3 f_c$, across the splash-fan wake (Figure 3.8c).

A third region of negative lateral vorticity is detected at the centerline plane, just above the jet-vortex described above (centered at $x = 360$ cm, $z = -20$ z cm in Figure 3.8a). As with the larger sub-surface eddy, this lateral vortex tube should also curl upward and reconnect with the surface. However, the expected zone of negative vertical vorticity was not resolved by our measurements (Figure 3.8c). Negative vorticity, as observed here, may arise from the large surface curvature associated with the crest (Longuet-Higgins 1992). Using cine film, Bonmarin(1989) observed the generation of negative vorticity during interaction between the splash-up and crest of a 2D breaker. Similarly, numerical simulations of 2D breaking have shown that negative vorticity can be generated in the beginning of splash-up zone (Chen *et al.* 1999). In this study, however, negative vorticity was not observed after the 2D plunger. Because the overall penetration of the 2D breaker was much shallower than that of the 3D breaker, it is

possible that the comparable region of negative vorticity for the 2D breaking event was too narrow to resolve in the measurement grid.

Vorticity may also be contributed from the boundary layer, the wave maker, and/or from wave-wave interactions. However, the sum of these contributions can be shown to be small by considering the incipient wave, for which we find a maximum lateral and vertical vorticity of $0.05\ f_c$, which is 5 % of the peak vorticity observed after the breaking wave-packet. Therefore, we conclude that the vorticity associated with the breaking wave-packet is predominantly due to the breaking event.

Finally, the instantaneous circulation observed at high spatial resolution by the DPIV is shown in Figure 3.9 for the plane $z = -10$ cm plane. The image agrees well with the ensemble averaged circulation depicted in Figure 3.8, indicating that the spatial resolution of the ADV measurements captured the significant components of flow structure. In addition, the estimate of instantaneous vertical vorticity by the DPIV observations is $4.5\ f_c$. This is $3 \sim 4$ times larger than that of the ensemble averaged observations. The larger instantaneous values suggest that the generation of vertical vorticity by individual waves may be even more significant than vorticity estimated by ensemble average velocity.

3.4 Discussions and Concluding Remarks

This study has demonstrated that 3D breaking can generate a circulation pattern (vertical vorticity) which is positive at the centerline and negative at the edge of the crest.

This circulation is not observed in 2D breaking. The occurrence of this circulation pattern is explained by vorticity evolution at the following three temporal stages.

At the beginning stage, *i.e.* $(t-t_o)f_c = 0.5$, a fan of splash-up is generated by the collapsing plunger jet (Figure 3.10a). At the same time a zone of positive vorticity is generated as the jet penetrates the wave surface entraining gas. Negative vorticity appears downstream and at the beginning of the splash fan zone. Subsequently, the plunging jet carries the positive vorticity downward 3 ~ 4 wave heights below the surface (Figure 3.10b). This suggestion is verified by observations of dye tracer evenly placed on the free surface and observed with an underwater camera, which will be further discussed in Chapter 4. The interactions between the plunging jet and the following waves result in an active roller eddy of positive lateral vorticity that migrates downstream.

At the intermediate stage, *i.e.* $(t-t_o)f_c = 5$, three regions of vorticity are observed. First, the active roller eddy has been transported one-half wave length, *i.e.* $0.5L$, downstream by the induced velocity (Figure 3.10b). A positive vertical vorticity is observed at the surface, as the generated current is laterally non-uniform (*i.e.* stronger near the center and weaker at the side). A vortex tube (see solid line in Figure 3.10b) consisting of the positive lateral and vertical vortices tilts upward to the free surface at the flank of the breaker because vortex lines cannot terminate in the body of a fluid. Second, another vortex tube (see dashed line in Figure 3.10b) consisting of the negative lateral and vertical vortices may be formed and is located just above the positive lateral vorticity. Third, the splash-fan wake, starting from $1/3\,L_c$ downstream of the positive votex tube and extending laterally to the flank of the breaker, generates a positive lateral vorticity (see the gray area in Figure 3.10b) near the surface. This vortex line also tilts

vertically and connects with the surface. Following the Peregrine's (1998) suggestions that the sign of vorticity can be influenced by nearby vorticity, the tilted (vertical) vorticity is thus positive by interacting with the nearby (*i.e.* central) positive vertical vorticity.

At the final stage, *i.e.* $(t-t_o)f_c=10$, both the positive and negative vortex tubes near the center are transported downstream due to the positive streamwise induced velocity (Figure 3.10c). These two vortex tubes are slightly inclined along the streamwise direction because the induced velocity is stronger near the surface and weaker away from the surface. At the splash-fan wake, the tilted positive vertical vorticity thus initiates the circulation. This circulation pattern (or vertical vorticity) decays with time but it is still significant after thirty wave periods from breaking. Therefore, each event of a three-dimensional plunging breaker can create three regions of vertical vorticity that last at least ten times the order of magnitude longer than its frequency.

A question is then often asked: can a finite length of three-dimensional breaker establish streamwise vorticity of Langmuir circulation (Langmuir, 1938)? As suggested by Csanady (1994) and Thorpe (1995), wind gusts and breaking waves can increase surface shear and generate vertical vorticity at their edges. If the Stokes drift were to interact with the more substantial vertical vorticity that is created by an external force like breaking, the generation of Langmuir circulation would be more robust, comparing with the feeble mechanism of CL2 instability (Craik, 1977). In this study, we did not observe Langmuir circulation because there was no Stokes drift. However, our observations show that the formation of these vertical vortices agree well with the prediction of Csanady's (1994) conceptual model that expresses the effects of breaking waves as a moving shear

stress anomaly (excess shear stress). Specifically, the primary flow patterns in our observations are very similar to those generated by the model. As demonstrated by Csanady (1994), the primary flow field (vertical vorticity) can interact with Stokes drift to easily establish Langmuir circulation. Therefore, we believe that a finite length of 3D breaker should produce Langmuir circulation (windrows) if there were Stokes drift.

Furthermore, the observed induced vertical vorticity for the 3D breaker has several implications. First, since breaking in the ocean is random and 3D (Thorpe 1992), the random occurrence of vertical vorticity may generate random windrows, which helps to explain the stochastic nature of windrows variability observed in the field (Welander 1963, Csanady and Pade 1969, Kenney 1977, Thorpe and Hall 1982). Second, the rich structure of vertical vortex spatial distribution (positive and negative vortices) can generate surface convergence and divergence in breaking wakes, which in turn would determine windrow length. This may also help to explain windrow length variability observed in the field (Kenney 1977, Thorpe 1992). Third, contrast to the 2D breaking waves, our observations show that a vertical vorticity persists by forming ensemble average of the 3D breaking waves. This result suggests that multiple 3D breaking events can be superimposed to produce a substantial vertical vorticity in the field. Forth, the temporal evolution of the observed vertical vorticity may provide the information to investigate the generation and decay of Langmuir circulation. An experiment designed to combine the interaction of 3D breaking waves and Stokes drift is needed to also reveal this evolution.

In conclusion, we have measured the three-component velocity field of 3D plunging breakers using an array of ADVs. The generation and decay of the induced

surface current for the 3D plunging breaker are reported. Our observations show that strong lateral variation of the surface currents can generate vertical vorticity that is important to establish Langmuir circulation.

3.5 References

Banner, M. L. and Peregrine, W. K., "Wave breaking in deep water," *Annu. Rev. Fluid Mech.*, **25**, pp.373-379, 1993.

Baldock, T., Swan, C., and Taylor, P., "A laboratory study of nonlinear surface waves on water," *Phil. Trans. R. Soc. Lond.*, **A 452**, 649-676, 1996.

Bonmarin, P., "Geometric properties of deep water breaking waves," *J. Fluid Mech.*, **209**, pp. 405-433, 1989.

Chang, K. A. and Liu, P. L.-F., "Velocity, acceleration, and vorticity under a breaking wave," *Phys. Fluid,* **10 (1)**, pp. 327-329, 1998.

Chen, G., Kharif, C., Zaleski, S., and Li J., "Two-dimensional Navier-Stokes simulation of breaking waves," *Phys. Fluid,* **11 (1)**, pp. 121-133, 1999.

Cowen, E.A., Monismith, S.G., "A hybrid digital particle tracking velocimetry technique," *Experiments in Fluids*, **22**, 199 - 211, 1997.

Craik, A. D. D., "The generation of Langmuir circulations by instability mechanism," *J. Fluid Mech.*, **81**, pp. 209-223, 1977.

Csanady, G. T. and Pade, B., "Windrow observations. Dynamics and diffusion in Great Lakes," Univ. of Waterloo Dept. Mech, Engr. Report, pp 3-38, 1969.

Csanady, G. T., "Momentum fluxes in reaking waves," *J. Geoph. Res.*, **95**, pp.13289-13299, 1990.

Csanady, G. T., "Vortex pair model of Langmuir circulation," *J. Marine Res.*, **52**, pp. 559-581, 1994.

Dommermuth, D. G., Yu, D. K. P, Rapp, R. J. Chan, F. S. and Melville, W. K., "Deep water breaking waves: a comparison between potential theory and experiments," *J. Fluid Mech.*, **89**, pp. 432-442, 1987.

Holthuijsen, L.H. and Herbers, T.H.C., "Statistics of breaking waves observed as whitecaps in the open ocean," *J. Phys. Oceanogr.*, **16**, pp.290-297, 1986.

Kenny, B. C., *An experimental investigation of the fluctuating current responsible for the generation of windrows*, Thesis, Univ. of Waterloo, pp 163.

Kraus, N. C., Lohrmann, A. and Cabrera, R., "New acoustic meter for measuring 3D laboratory flows," *J. Hydr. Eng.*, **120 (3)**, pp. 406-412, 1994.

Kolaini, A. and Tulin, M., "Laboratory measurements of breaking inception and post-breaking dynamics of steep short-crested waves," *Int. J. of Offshore and Polar Engng,* **5**, pp. 212-218, 1995.

Langmuir, I, "Surface motion of water induced by wind," *Science*, **87**, pp. 119-123, 1938.

Lin, P. and Liu, P. L.-F., "A numerical study of breaking waves in the surf zone," *J. Fluid Mech.*, **359**, pp. 239-264, 1998.

Longuet-Higgins, M. S. and Cokelet, E. D., "The deformation of steep surface wave in water. I. A numerical method for computation," *Phil. Trans. R. Soc. London,* **A58**, pp. 1-26, 1976.

Lohrmann, A. Cabrera, R. and Kraus, N. C., "Acoustic Doppler velocimeter (ADV) for laboratory use," *Proc. Symp. on Fundamentals and Advancements in Hydr. Measurements and Experimentation,* edited by C. A. Pugh, pp. 351-365, 1994.

Melville, W. K., "The role of surface-wave breaking in air-sea interaction," *Annu. Rev. Fluid Mech.*, **28**, pp.279-321, 1996.

Meza, E., Zhang J., and Seymour R., "Free-wave energy dissipation in experimental breaking waves," to be appeared in *J. Phys. Oceanogr.*

Miyata, H, Kanai, A., Kawamura T. and Park, J.-C., "Numerical simulation of three-dimensional breaking waves," *J. Marine Sci. and Tech.*, **1**, pp183-197, 1996.

Nepf, H. M., Wu, C.H., and Chan, E.S., "A comparison of two- and three-dimensional wave breaking," *J. Phys. Oceanogr.*, **28**, pp.1496-1510, 1998.

Nikora, V. I. and Goring D. G., "ADV measurements of turbulence: Can we improve their interpretation?" *J. Hydr. Engrg.*, **124 (6)**, pp. 335-355, 1998.

Peregrine, D. H., "Breaking water waves" in *Nonlinear Topics in Ocean Physics*, edited by Osborne, A. R., Course 109, *Italian Phys. Soc.*, Internat. Sch. of Physics, North Holland, pp. 499-526, 1991.

Peregrine, D. H., "Surf zone currents," *Theor. and Comp. Fluid Dyna.*, **10**, pp. 295-309, 1998.

Peregrine, D. H., "Large scale (vertical) vorticity generation by 3D Bores in shallow water," *IUTAM Symp. on Three-dimensional Aspects of Air-Sea Interaction*, Nice, pp. 9-12, 1998.

Peregrine, D. H., "Large scale vorticity generated by breakers in shallow and deep water," *Eur. J Mech. B/Fluid*, pp. 77-82, 1999.

Perlin, M., He, J. and Bernal, L. P., "An experimental study of deep water plunging breaker," *Phys. Fluid,* **8**, pp. 2365-2374, 1996.

Rapp, R .J. and Melville W. K., "Laboratory measurements of deep water breaking waves," *Phil. Trans. R. Soc. London,* **A331**, 735-780, 1990.

She, K., Greated, C. A. and Easson, W. J., "Experimental study of three-dimensional wave breaking," *J. of Waterway, Port, Coastal, and Ocean Eng.* **120**, pp. 20-36, 1994.

She, K., Greated, C. A. and Easson, W. J., "Experimental study of three-dimensional breaking waves kinematics," *Applied Ocean Res.* **19**, pp. 329-324, 1997.

Skyner, D., "A comparison of numerical predictions and experimental measurements of internal kinematics of a deep-water plunging wave," *J. Fluid Mech.*, **315**, pp. 51-64, 1996.

Su, M. Y., Green, A. W., and Bergin M. T., "Experimental studies of surface wave breaking and air entrainment" in *Gas transfer at water surfaces*, edited by Brutsaert, W. and Jirka, G. K. (Reidel Publishing Company, Dordrecht), pp. 211-219, 1984.

Thorpe, S. A., "The breakup of Langmuir circulation and instability of an array of vortices," *J. Phys. Oceanogr.,* **22**, pp.350-360, 1992.

Thorpe, S. A., "Dynamical processes of transfer at the sea surface," *Prog. Oceanog.*, **35**, pp315-352, 1995.

Thorpe, S. A. and Hall, A. J., "Observations of the thermal structure of Langmuir circulation," *J. Fluid Mech.*, **114**, pp. 237-250, 1982.

Tsai, W. T. and Yue, D. K. P., "Computation of nonlinear free-surface flows," *Annu. Rev. Fluid Mech.*, **28**, pp.249-278, 1996.

Xü H., and Yue, D.K.P., "Computations of fully nonlinear three-dimensional water waves," *Proc.19th Symp.on Naval Hydrodyn.*, Seoul, Korea, pp. 177-201, 1992.

Voulgaris, G. and Trowbridge, J. H., "Evaluation of acoustic Doppler velocimeter (ADV) for turbulence measurements," *J. Atmospheric and Oceanic Technol.*, **15 (1)**, part2, pp.272-289, 1998.

Wetlander, P., "On the generation of wind streaks on the surface by action of surface film," Tellus, **15**, pp. 67-71, 1963.

White, C. J., *A laboratory study of breaking waves using digital particle image velocimetry,* Thesis in Univ. of California, San Diego, 1996.

Wu, C. H. and Nepf, H. M., "Breaking criteria and energy losses for three-dimensional wave breaking," submitted to *J. Geoph. Res.*, 1999.

Wu, J. "Sea-surface drift currents induced by wind and waves," *J. Phys. Oceanogr.*, **13**, pp.1441-1451.

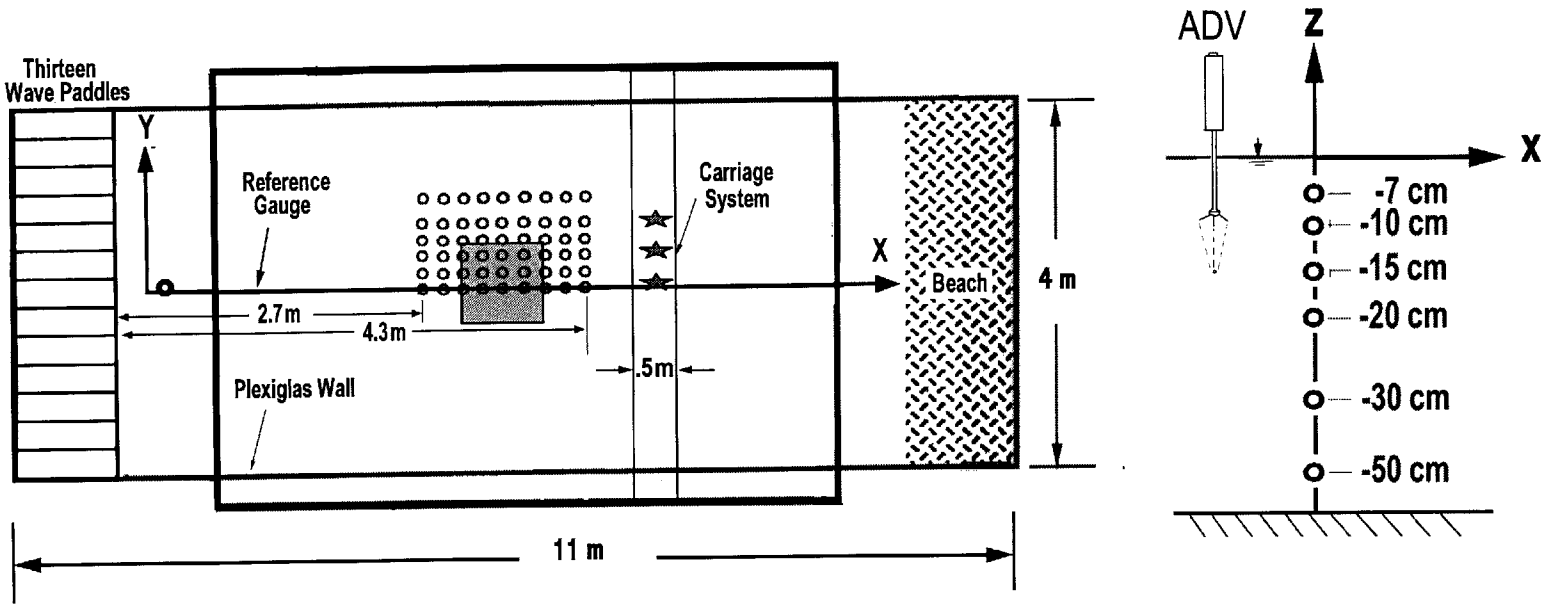

(a) top view

(b) side view

Figure 3.1. Top view (a) and side view (b) of the test section. The arrays of ADVs, shown as ★ ,were held by a moving carriage system. Circles indicate the locations of velocity measurement using ADVs. The gray zone corresponds to the PIV image area 60 x 60 cm^2. To verify the repeatability of waves for different runs, a reference wave gauge was kept at location (x=180, y=0) cm.

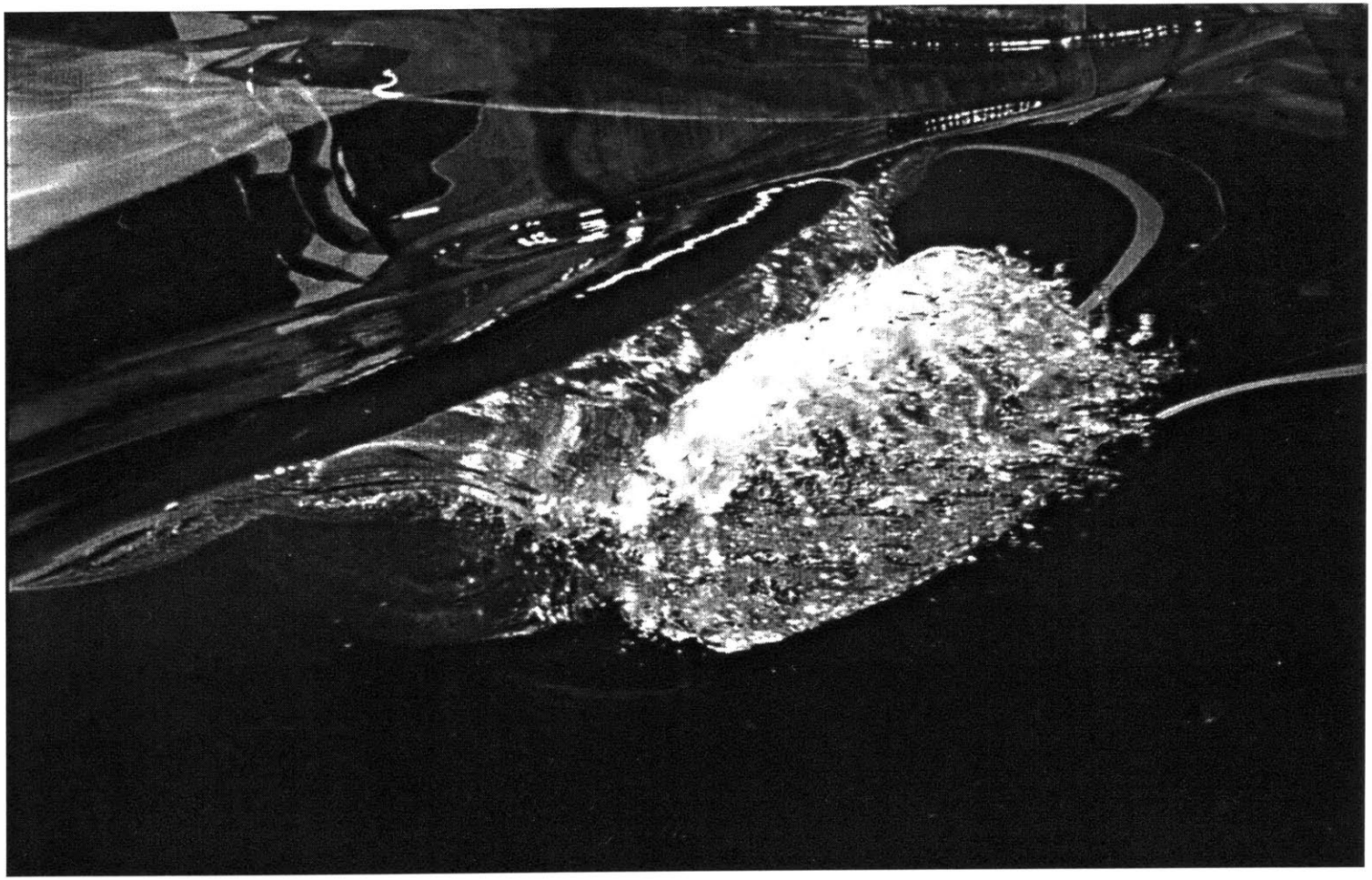

Figure 3.2. Photograph of the three-dimensional plunging breaker. The short-crested waves traveling from the left to the right first plunge and subsequently create splash-up downstream.

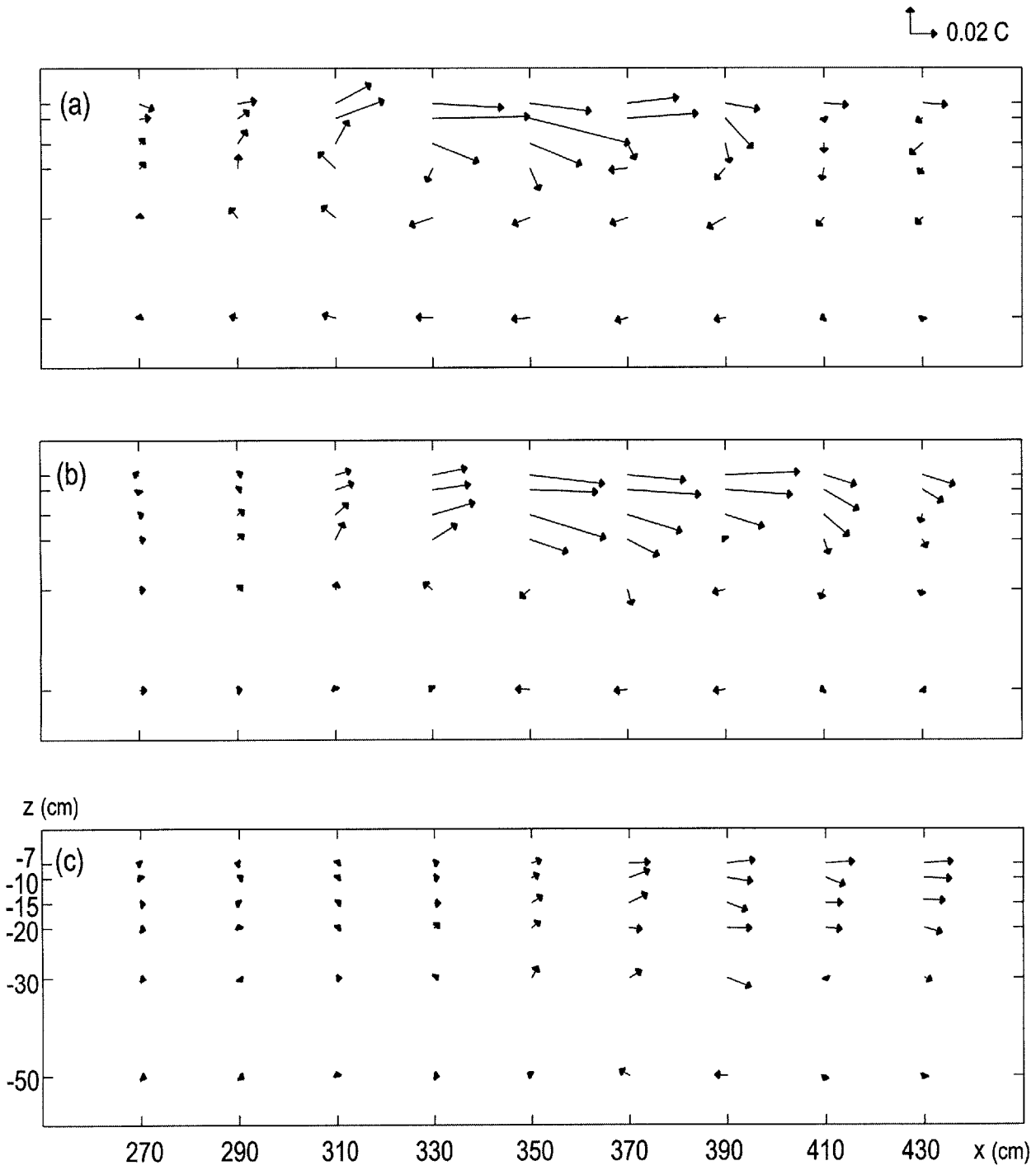

Figure 3.3. The induced mean velocity for the two-dimensional plunger at the lateral plane y = 45 cm. Each graph correponds to time $(t-t_o)f_c$ = (a) 5, (b) 10, and (c) 30 after the wave breakes.

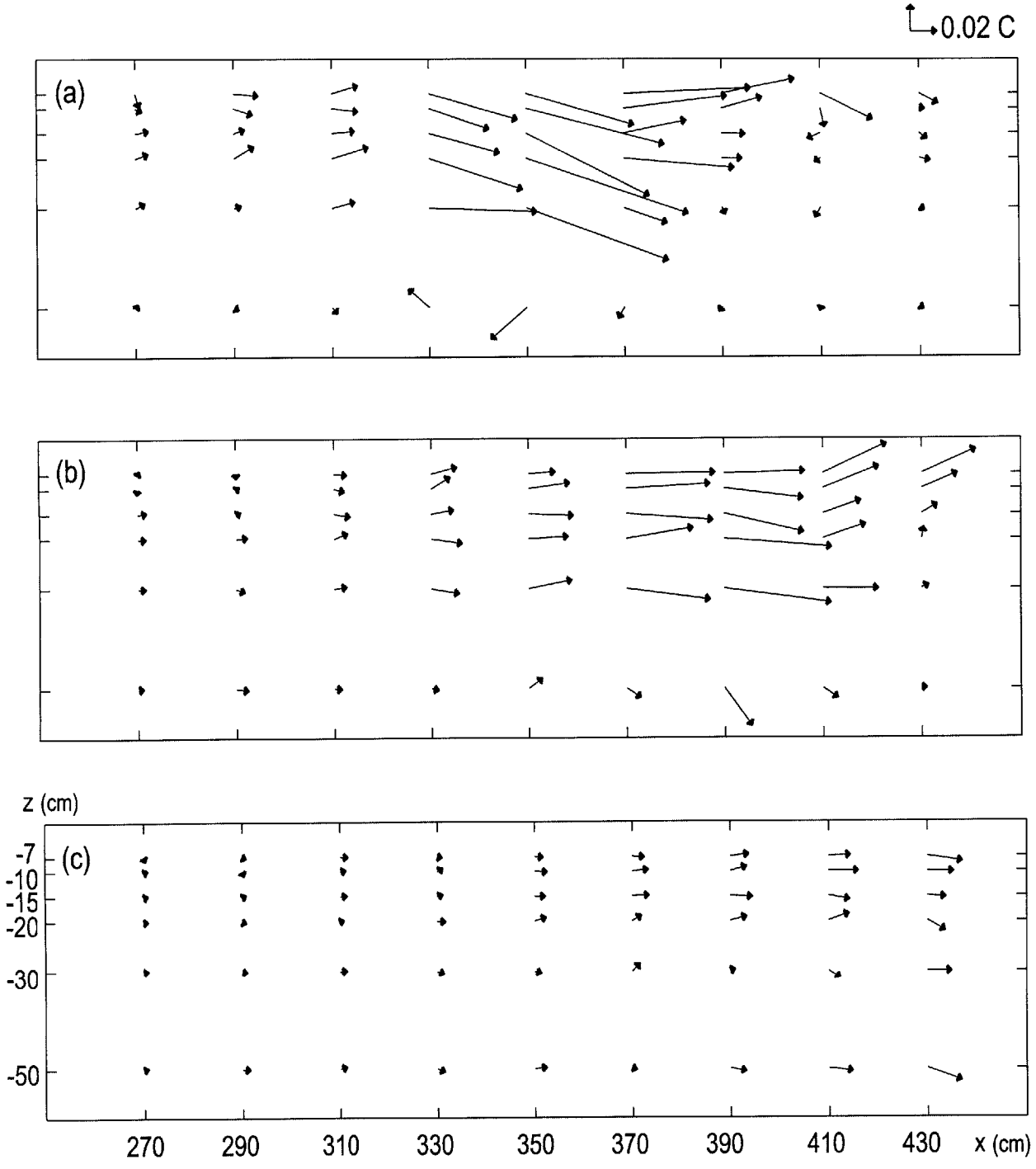

Figure 3.4. The induced mean velocity for the three-dimensional plunger at the center plane y = 0 cm. Each graph correponds to time $(t - t_o) f_c$ = (a) 5, (b) 10, and (c) 30 after the wave breakes.

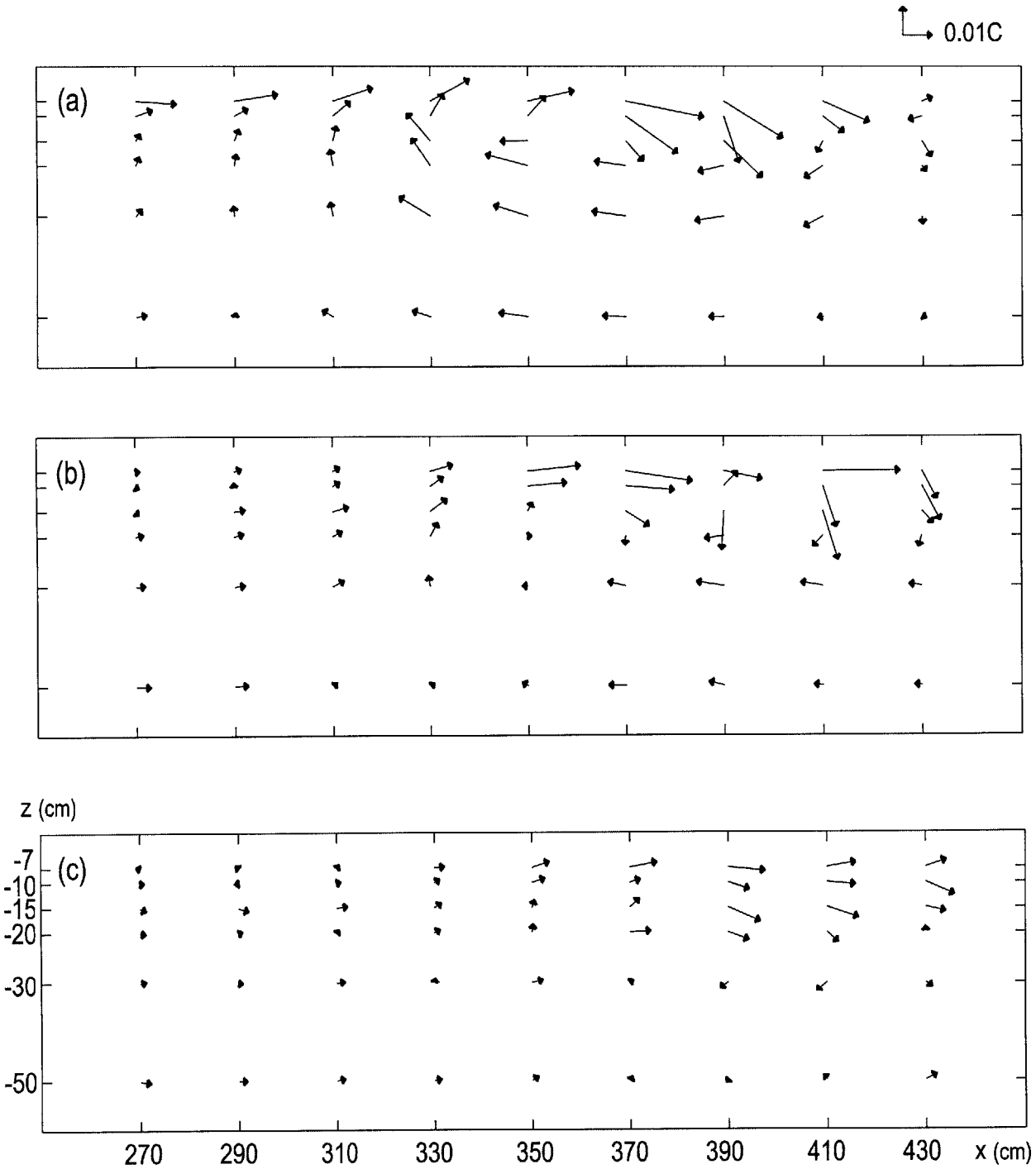

Figure 3.5. Same as in Figure3.4 but for the lateral plane y = 45 cm. Note the scale is enlarged two times in order to see the circulation pattern.

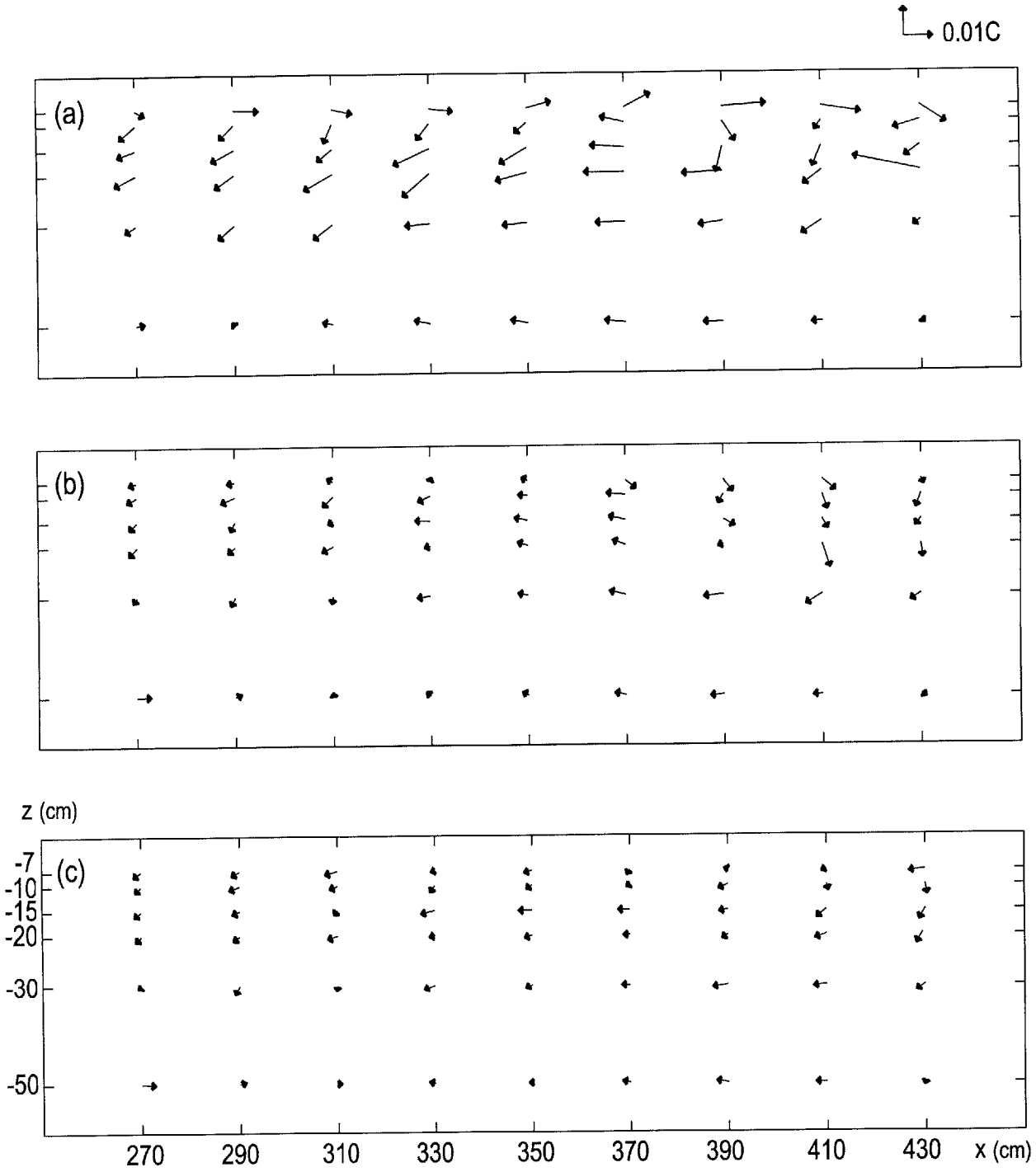

Figure 3.6. Same as in Figure 3.5 but for the lateral plane y = 90 cm.

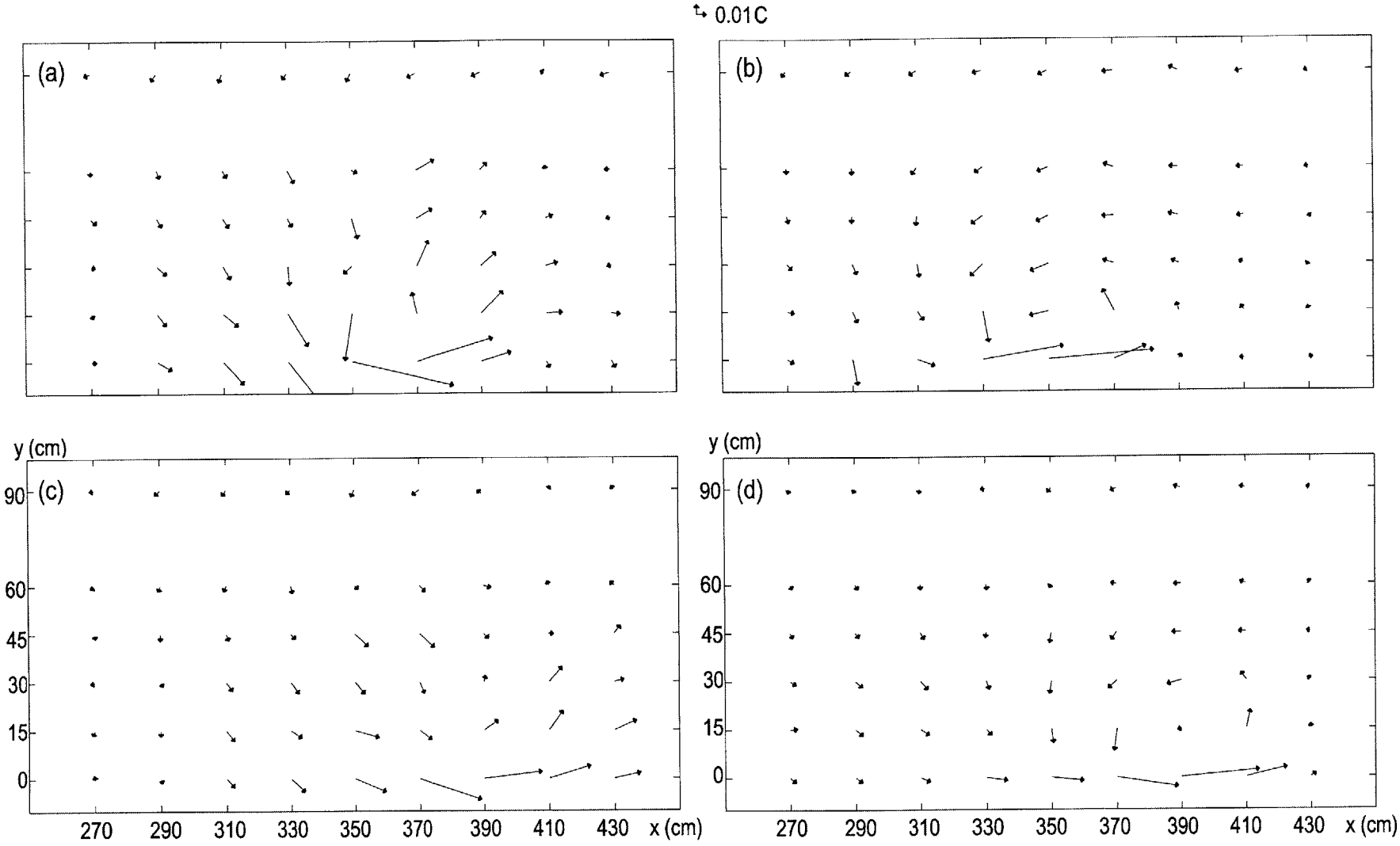

Figure 3.7. The induced mean velocity for the three-dimensional plunger on the horizontal plane z = -10 cm at time $(t-t_o)f_c$ = (a) 5 and (c) 10; and on the horizontal plane z = -30 cm at time $(t-t_o)f_c$ = (b) 5 and (d) 10.

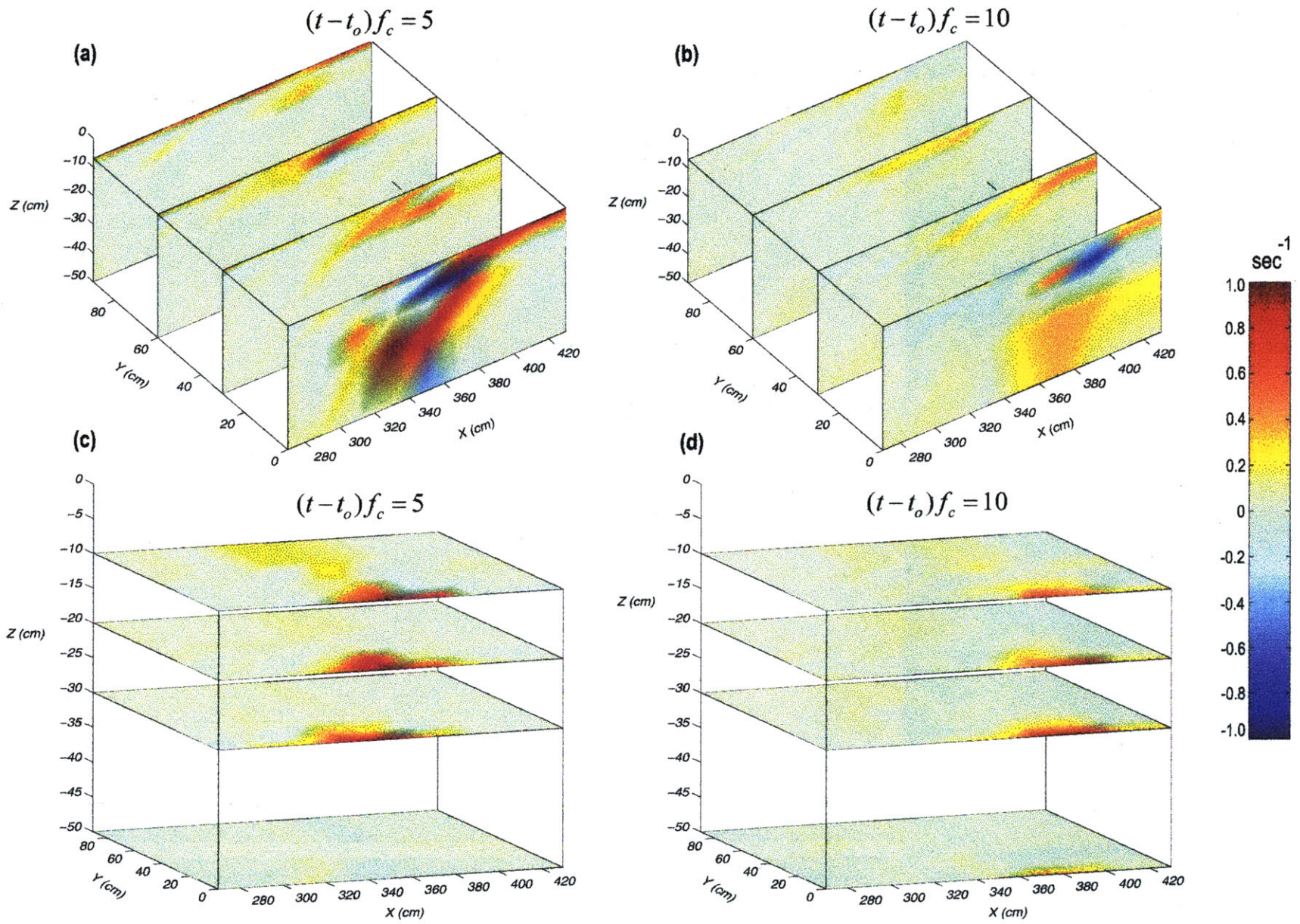

Figure 3.8. Vorticity induced by the three-dimensional plunging breaker at $(t-t_o)f_c = 5$ and 10 wave periods. (a) and (b): the horizontal vorticity field with y = 0, 30, 60, and 90 cm planes. (c) and (d): the vertical vorticity field with z = -10, -20, -30, -50 cm planes.

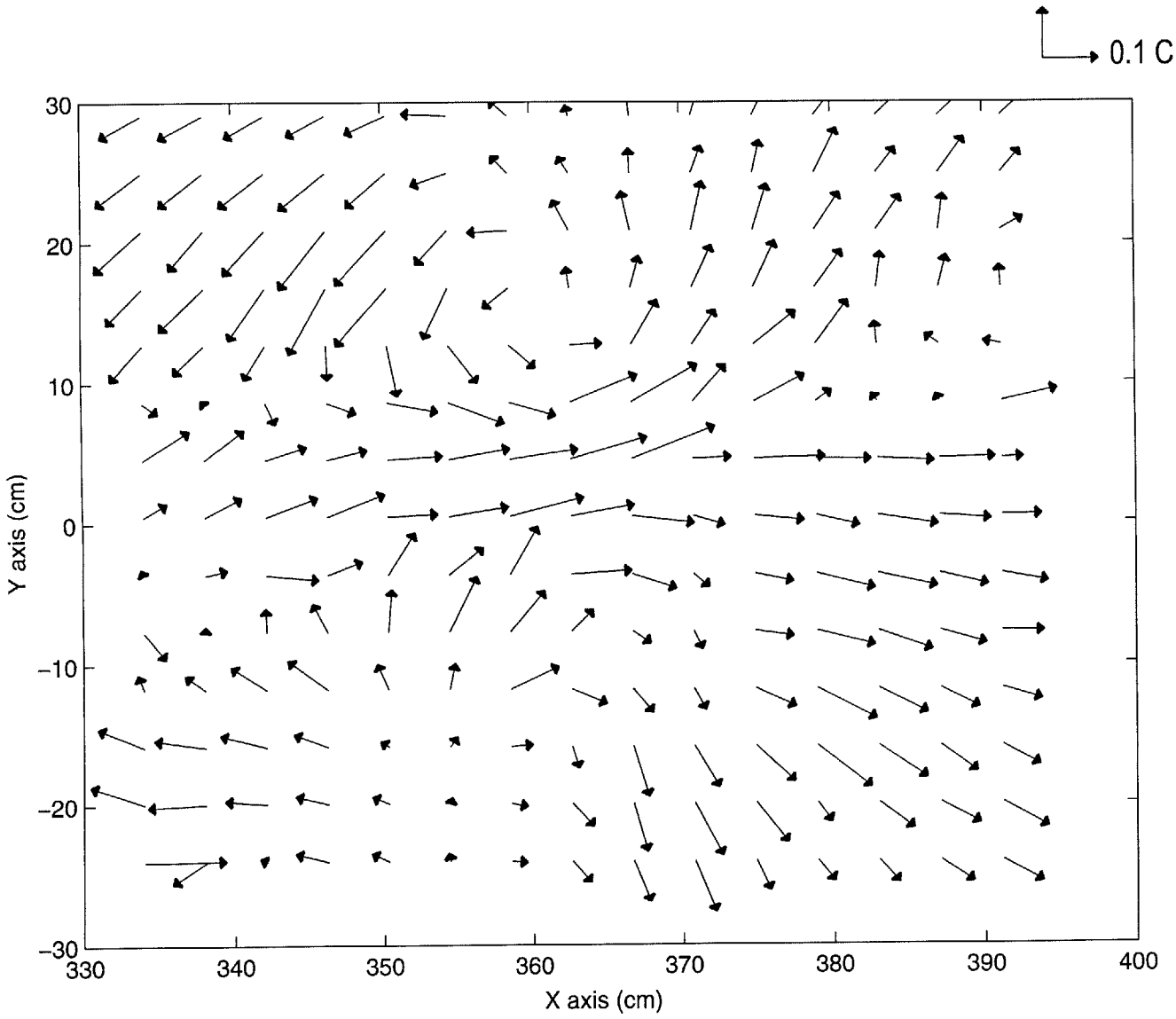

Figure 3.9. The instantaneous induced mean velocity at the plane z =-10 cm and time $(t-t_o)f_c = 5$ by DPIV. The estimated instantaneous vorticity can be as high as 4.5 f_c.

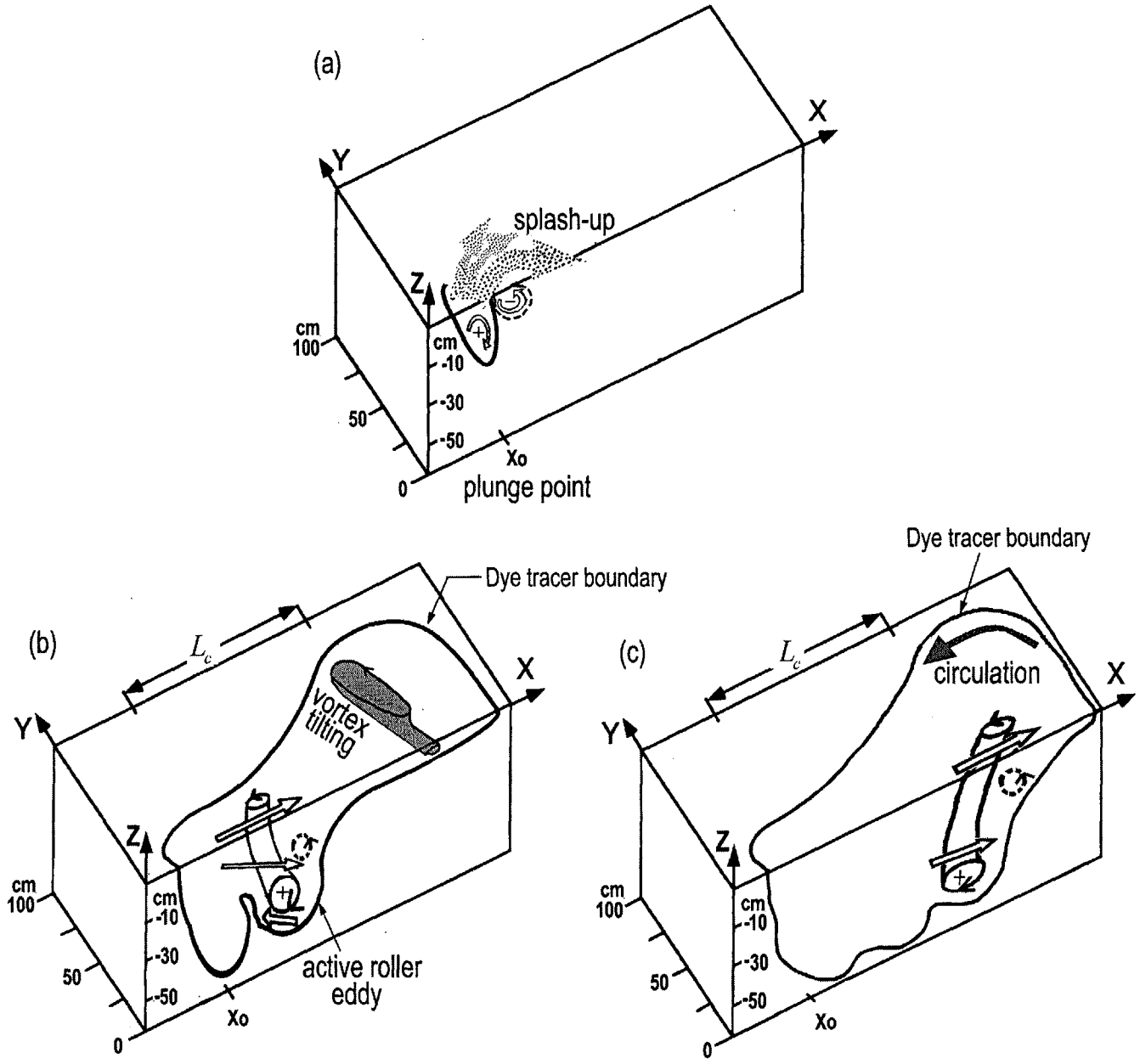

Figure 3.10. Vorticity evolution at three temporal stages. (a) $(t-t_o)f_c = 0.5$, (b) $(t-t_o)f_c = 5$, and (c) $(t-t_o)f_c = 10$. In each graph, the solid and dashed lines correspond to the positive and negative vorticity, respectively. The gray area represents the positive vorticity generated by the splash-up fan.

Chapter 4: Turbulence and Mixing Generated by Three-Dimensional Wave Breaking

4.1 Experimental Methods

4.1.1 Turbulence

To obtain the turbulence generated by wave breaking, we use the recorded velocity measurements described in Chapter 3.2. By subtracting the raw velocity, $q(x,y,z,t)$, from the ensemble mean velocity, $<q(x,y,z,t)>$, in (3.1), the fluctuating velocity is

$$q'(x,y,z,t) = q(x,y,z,t) - <q(x,y,z,t)>, \tag{4.1}$$

where $q'(x,y,z,t)$ can be any fluctuating velocity component $u'(x,y,z,t)$, $v'(x,y,z,t)$, or $w'(x,y,z,t)$ in the prescribed x, y and z directions (see Figure 3.1). The intensity of the fluctuating velocity can be evaluated as the variance of the 10 experimental runs,

$$<q'^2> = \frac{1}{10}\sum_{n=1}^{10}[q_n']^2 . \tag{4.2}$$

For convenience, the square root of the variance, $[<q'^2>]^{1/2}$, is used as a measure of magnitude for the fluctuating velocity.

The fluctuating velocity consists of three sources: breaking generated turbulence, q'_{gt}, random surface waves, q'_{rw}, and the measurement noise, q'_{mn}, *i.e.*

$$q' = q'_{gt} + q'_{rw} + q'_{mn} . \tag{4.3}$$

Substituting (4.3) into (4.2), and assuming that correlation between the three sources of the fluctuating velocity, *i.e.* $< q'_{gt} q'_{rw} >$, $< q'_{gt} q'_{mn} >$, and $< q'_{rw} q'_{mn} >$ is weak, we get

$$< q'^2 > \approx < q'^2_{gt} > + < q'^2_{rw} > + < q'^2_{mn} > . \tag{4.4}$$

The variance of the measurement noise, $< q'^2_{mn} >$, resulting from the instrument noise of the ADVs, can be evaluated from the time series records of $< q'^2 >$ before waves break assuming that there is no turbulence. The measurement noise is $0.0005\,C$ for $[< w'^2_{mn} >]^{1/2}$ and $0.002\,C$ for both $[< u'^2_{mn} >]^{1/2}$ and $[< v'^2_{mn} >]^{1/2}$, consistent with the manufacturer's specification that lateral component noise is roughly four times larger than that of vertical component (Lohrmann *et al.* 1995). The variance of $< q'^2_{rw} >$ comes from random waves generated by breaking. The 90 % confidence interval for the square root of the variance is between 0.73 ~ 1.64 $[< q'^2 >]^{1/2}$ for ten experimental samples (Walpole and Myers 1993). The contribution of random waves $[< q'^2_{rw} >]^{1/2}$ to the $[< q'^2 >]^{1/2}$ is thus 10 % (Figure 4.2).

The variance of the generated turbulence, $< q'^2_{gt} >$, can be evaluated from the time series records of $< q'^2 >$ by removing $< q'^2_{mn} >$ and $< q'^2_{rw} >$. In other words, at times after the wave breaks, the $[< q'^2 >]^{1/2}$ is the turbulence generated only by breaking with an error of 10% and measurement noise of $0.0005\,C \sim 0.002\,C$.

4.1.2 Mixing

To quantify the temporal and spatial extent of turbulent mixing generated by breaking, a flow visualization technique that integrates laser-induced fluorescence, digital image processing, and image reconstruction was developed. The experimental setup is shown in Figure 4.1. Before each experimental run, a thin patch of Uranine dye with emission wave length 490-520 nm was evenly spread on the free surface. The dye was applied as a fine mist produced by the tips of three (FogJet 7N) high pressure sprays at the end of 1/4" PVC pipe. A 0.75 Hp gravity pump was used to drive the fluorescein dye into the PVC pipe. A fine mist is required to produce a uniform dye layer at the water surface, and to avoid penetration of dye into the water column prior to breaking.

After breaking the penetrating dye cloud tracked the motion of fluid injected beneath the surface by the breaking event. The dye cloud was illuminated by a 2 cm thick laser light sheet created by passing the beam of a 6-watt Argon-Ion laser (Coherent INNOVA 70) through a fiber optic and a cylindrical lens (Dantec 9060 water-tight light-sheet). The laser-light sheet was oriented to illuminate the x - z plane. A total of six planes, *i.e.* y = 0, 15, 30, 45, 60, and 90cm, was examined in separate experimental runs for both two- and three-dimensional breaking waves. A watertight, CCD camera (COHU 4910) with 640 x 480 pixel resolution was used to capture images of the evolving dye. To minimize optic distortion, the camera was positioned at 90 degrees to the visual plane illuminated by the light sheet. Note that the side-walls of the test section are made of Plexiglas to provide a clear field of view for camera.

A Bitfiow PCI bus frame grabber board embedded in a Pentium-90 microcomputer transfers 74 digitized, real-time images to a 64 megabytes host RAM. The

collection of images was controlled by EYE Image Calculator software. In order to maximize the collection of key images and to minimize image storage requirements, the rate of image sampling was varied during the breaking evolution. With the plunging event occurring over a period of 20 seconds, two sampling rates were chosen: 10 Hz for $(t-t_o)=1-6$ seconds and 1 Hz for $(t-t_o)=6-20$ seconds. The frame grabber was synchronized with the wave generation system to provide a consistent time reference between runs. The time reference was then used to synchronize images collected over experimental runs at the multiple planes. To avoid image contamination from the residual fluorescence dye, only one experiment run was performed each day so that the residue dye can be bleached out by photo decay.

Finally, a series of image processing tools were used to sharpen and improve contrast (Figure 4.3). To correlate the recorded images with real dimensions, a calibration board was placed in the plane of laser light sheet at each lateral position and digitally imaged. The board is marked with a 20 cm spacing in the x direction and the vertical positions at z = -7, -10, -15, -20, -30, and -50 cm, corresponding to the measurement points of the velocity. The resolution is 4.4 x 4.4 mm^2 for each pixel of the recorded images at the plane $y=90\,cm$, which is the farthest from the CCD camera. Using SigmaScan/Image software developed by Jandel Scientific, the dye mixing area, $A(y,t)$, at each time and on each of six y planes were analyzed. The individual plane images were also used to re-construct a three-dimensional image of the dye mixing volume, $\forall(t)$, generated by the plunging breaker wake.

4.2 Results

The spatial and temporal evolution of the turbulence generated by the three-dimensional plunging breaker is shown in Figure 4.4. Five wave periods after breaking, *i.e.* $(t-t_o)f_c = 5$, the wave group has passed the test section and a large turbulent wake, center at x = 350 cm, is left behind (Figure 4.4a). The strength of the wake is quantified by the turbulent kinetic energy, $TKE = \frac{1}{2}\left[< u_{gt}'^2 > + < v_{gt}'^2 > + < w_{gt}'^2 >\right]$, normalized by the square of the characteristic wave speed, C^2. At the centerline, TKE reaches to the depth of 30 cm and is $2.5\times10^{-3}C^2$, which is four times larger than that of two-dimensional breaker (Rapp and Melville 1990). Away from the centerline, the strength of TKE decreases to $0.5\times10^{-3}C^2$ near the surface as the breaker becomes weaker and turns into a spiller. This TKE spreads laterally as turbulent wake advects downstream. Note that only one half of the turbulent wake is shown here. Taking the symmetric at the centerline, the whole shape of the turbulent wake looks like a teardrop patch, consistent with conjectured shape by Thorpe (1995). At $(t-t_o)f_c = 10$ (Figure 4.4b), the central core of TKE is $2\times10^{-3}C^2$ and penetrates deeper to the depth over 50 cm. The turbulent wake also advects further downstream. The turbulent wake decays with time, but persists at least 30 wave periods from breaking.

The flow visualization photographs in Figure 4.5 show a comparison of mixing areas at the centerline generated by the three and two-dimensional plungers . Two main differences are found. First, at $(t-t_o)f_c = 5$, the dye penetrated by the three-dimensional plunger (Figure 4.5a) at $x \approx 310$ cm has reached to the depth of 60 cm, which is two times larger than that of the two-dimensional plunger (Figure 4.5c) with a

comparable wave height of 17 cm. In other words, the penetration depth for the three-dimensional plunger is 3 ~ 4 wave heights, consistent with the penetration depth of small bubbles generated by breakers in the field (Thorpe and Hall 1983). Second, as time goes by, the mixing area for the three-dimensional plunger increases more rapidly than that of the two-dimensional plunger. Specifically, the mixing area grows significantly from $x \approx 360$ cm (Figure 4.5a) to $x \approx 400$ cm (Figure 4.5b), corresponding to where the active roller turbulent eddy is. The penetration depth of this active roller eddy is 55 cm. On the other hand, the growth of the mixing area for the two-dimensional plunger is less pronounced and the penetration depth is only 35 cm.

To examine the mixing characteristics of three-dimensional breaking, we investigate the mixing areas at different lateral planes (Figure 4.6). Near the centerline, where $y = 0$ (Figure 4.6a) and 30 cm (Figure 4.6b), the growth of mixing areas comes from two contributions: the plunging at (x, z)=(310, 50) cm and the active roller eddies at (x, z)=(370, 50) cm. In contrast, at the edge of breaker where $y = 60$ (Figure 4.6c) and 90 cm (Figure 4.6d), only the active roller eddies at (x, z)=(380, 15) cm resulting from the spiller contributes to the growth of the mixing area. This spatially inhomogeneous characteristic created by a finite length of the three-dimensional plunger causes the mixing region to grow laterally as well as vertically and longitudinally, distinct from growing only vertically and longitudinally in two-dimensional breaking. In other words, the mixing generated by three-dimensional breaking should be more efficient than that by two-dimensional breaker.

To examine the growth of mixing area, we use a log-log plot of the mixing area, $A(y,t)$, of different lateral planes against time, t (Figure 4.7). The $A(y,t)$ and t are

normalized by k_c^2 and $2\pi f_c(t-t_o)$, respectively. Five wave periods after breaking, the evolution of the mixing area apparently follows a power law

$$A(y,t)k_c^2 = I\left[2\pi f_c(t-t_o)\right]^S, \tag{4.5}$$

where S is the growth rate and is the slope of the log-log plot in Figure 4.7a. I can be interpreted as the initial mixing area and is the vertical intercept in Figure 4.7a. Based on the correlation coefficients of 0.90, it is interesting that the slopes, S, near the center and at the edge of the three-dimensional breaking are close to that of the two-dimensional breaking, suggesting that the growth of mixing is dominated by the vertical and longitudinal directions. On the other hand, at $y = 45\,\text{cm}$ where the inhomogeneous mixing is expected (Figure 4.6), S is as large as 0.84, as compared to 0.5 in the two-dimensional plunger. The mixing area there can extend without restraints, causing a more effective growth of mixing. Furthermore, integrating each plane laterally, we examine the temporal evolution of the three-dimensional generated mixing volume, $V(t)$, normalized by k_c^3 (Figure 4.7b). Comparing the slopes of S in the three- and two-dimensional breaking, we find that mixing of the three-dimensional breaker wake is more rapid, given that the correlation coefficient is as good as 0.95.

4.3 Discussions and Conclusions

The dissipation rate due to deep-water wave breaking is of critical importance in achieving an accurate representation of the sink in the wind wave modeling (Komen *et al.*

1994). To estimate the dissipation rate due to three-dimensional breaking, the turbulent kinetic energy, TKE, and the mixing volume, $\forall(t)$, of the turbulent wake are needed. The total integrated turbulent kinetic energy, $\overline{TKE\forall}(t)$, is

$$\overline{TKE\forall}(t) \equiv \rho \iiint_{\forall(t)} TKE \; dzdydx \quad , \tag{4.6}$$

where ρ is the water denisity. Two procedures are employed to evaluate (4.6). First, to determine if the turbulent wake reaches a specific grid position, the dye image at each plane is superimposed onto the image of the calibrarion board at the corresponding plane. The boundary of the dye at each plane indicates the spatial evolution of the turbulent wake at each time. Second, TKE at each grid position within the wake is multiplied by the surrounding volume of the grid poistions where the turbulent wake exists.

From the results discussed in Section 4.2, we found that both $\overline{TKE\forall}(t)$ and $\forall(t)$ follow power laws for longer time (five wave periods after breaking), *i.e.*,

$$\overline{TKE\forall}(t) \propto t^{-R_1} \tag{4.7}$$

and

$$\forall(t) \propto t^{R_2} , \tag{4.8}$$

where R_1 and R_2 are real constant numbers. The dissipation rate due to wave breaking is therefore

$$\varepsilon_b \equiv \frac{d}{dt}\left(\frac{\overline{TKE\,\forall}}{\rho\forall(t)}\right) \propto t^{-(R_1+R_2+1)}, \tag{4.9}$$

where ε_b is dissipation rate per unit mass.

A second estimate of dissipation rate can be found based on dimensional analysis. The total integrated kinetic energy is expressed as

$$\overline{TKE\forall}(t) \propto \rho U^2 \ell^3, \tag{4.10}$$

where ℓ is an integral length scale of the turbulence and can be roughly considered as one-third root of the mixing volume, *i.e.* $[\forall]^{1/3}$. From (4.8), it follows

$$\ell \propto t^{\frac{R_2}{3}}. \tag{4.11}$$

The characteristic velocity, U, can be obtained by substituting (4.7) and (4.11) into (4.10), *i.e.*

$$U \propto t^{\frac{-(R_1+R_2)}{2}}. \tag{4.12}$$

Although three-dimensional turbulent breaker wake is inhomogenous, the integrated three-dimensional breaking wake can be viewed as isotropic turbulence, suggested by Chasnov (1997). Assume that the Reynolds number is large enough so that the larger

generated eddies can supply the energy to the smaller eddies at the rate equal to dissipation rate, the dissipation rate, ε_b, is given by Taylor's (1935), that is

$$\varepsilon_b \propto \frac{U^3}{\ell}. \tag{4.13}$$

Substituting (4.11) and (4.12) into (4.13), we get

$$\varepsilon_b \propto t^{-\frac{3}{2}R_1 - \frac{11}{6}R_2} \tag{4.14}$$

The above analysis can be degenerated to two-dimensional breaking waves by replacing the mixing volume, $\forall(t)$, with the mixing area, $A(y,t)$. A similar analysis of dissipation rate for two-dimensional breaking can be found in Rapp and Melville (1990).

Figure 4.8 shows the volume integrated turbulent kinetic energy in $<u_{gt}'^2>$, $<v_{gt}'^2>$, and $<w_{gt}'^2>$ components for the three-dimensional plunger. It is interesting to note that the decay for each component follows a $t^{-1\pm0.06}$ power law, which is similar to that of the two-dimensional plunger with a constant-amplitude spectrum (Rapp and Melville 1990). Based on the correlation coefficient of 0.95, the decay of total integrated turbulent kinetic energy, $\overline{TKE\forall}(t)$, for three- and two-dimensional breakers are close to each other. Moreover, the decay of $\overline{TKE\forall}(t)$ for the two-dimensional plunger with a constant-steepness spectrum (Figure 4.9) also resembles that with a constant amplitude spectrum by Rapp and Melville's (1990), suggesting that the decay of turbulence is not

sensitive to spectral shapes. We summarize the dissipation rates due to the three- and two-dimensional breaker in Table 4.1. Although the integrated turbulent kinetic energy is similar, the dissipation rate ε_b due to the three-dimensional breaker is much larger than that of the two-dimensional breaker, indicating that the three-dimensional turbulence is more dissipative. The ε_b estimated by (4.9) and (4.14) agrees with each other, suggesting that integrating inhomogenous turbulent over inhomogenous directions indeed results in homogenous turbulence in the integral scales (Chasnov 1997).

The above results highlight several important issues. First, the turbulence generated by three-dimensional breaking can penetrate to the depth of $3 \sim 4$ wave heights, which explains and supports the enhanced dissipation surface layer observed in the field (Agrawal et. al 1992, Terray *et. al* 1996). Second, mixing generated by a finite length of three-dimensional breaking is more rapid than that by two-dimensional breaker. Besides the mixing in the longitudinal and vertical directions, the lateral extent provides another degree to the evolution of mixing. Third, three-dimensional breaking can cause a higher dissipation rate, which should be taken into account in numerical modeling or field applications. Finally, our estimates of the intergral length scale, ℓ, in (4.11) and the characteristic velocity, U, in (4.12) for three-dimensional breaking provide a basis for calculating temporally varying eddy viscosity, *i.e.* $U\ell \propto t^{\frac{-(3R_1+R_2)}{6}}$.

In conclusion, the turbulence and mixing generated by three-dimensional breaking waves are different from those by two-dimensional breaking waves. To the best of our knowledge, these detailed measurements of velocity field and mixing for three-

dimensional, unsteady deep-water breaking waves are the first laboratory study to address the complexity of three-dimensional breaking waves.

4.4 References

Agrawal, Y.C., Terray, E.A., Donelan, P.A., Hwang, A.J., and Williams, W.M., Drennan, K.K. Kahma and Kitaigorodskii, S.A., "Enhanced dissipation of kinetic energy beneath surface waves," *Nature*, **359**, pp. 219-220, 1992.

Chasnov, J. R., "On the decay of inhomgeneous turbulence," *J. Fluid Mech.*, **342**, pp. 335-354, 1997.

Komen, G. J., Cavaleri, L., Donelan M., Hasselmann K., Hasselmann, S., and Janssen P.A.E.M., *Dynamics and modeling of ocean waves*, Cambridge University Press, 532 pp., 1994.

Lohrmann, A. Cabrera, R. and Kraus, N. C., "Acoustic Doppler velocimeter (ADV) for laboratory use," *Proc. Symp. on Fundamentals and Advancements in Hydr. Measurements and Experimentation,* edited by C. A. Pugh, pp. 351-365, 1994.

Rapp, R .J. and Melville W. K., "Laboratory measurements of deep water breaking waves," *Phil. Trans. R. Soc. London,* **A331**, 735-780, 1990.

Terray A.M., Agrawal, Y.C., Drennan, W.M., Kahma, K.K., Williams, A.J., "Esitmates of kinetic energy dissipation under breaking waves," *J. Phys.Oceanogr.*, **262,** pp. 792-807, 1996.

Thorpe, S. A., "Dynamical processes of transfer at the sea surface," *Prog. Oceanog.*, **35**, pp315-352, 1995.

Thorpe, S. A. and Hall, A. J., "The characteristics of bubbles clouds, breaking waves and near surface currents observed using side-scan sonar, *Continental Shelf Res.*, **1**, pp. 353-384, 1983.

Walpole, R. E. and Myers, R. H., *Probability and statistics for engineers and sciences,* Macmillan Publishing Company, 766 pp., 5th Edition, 1993.

Table 4.1. The dissipation rates due to the three- and two-dimensional breaker.

	3D	**2D** constant-steepness spectrum	**2D** constant-amplitude spectrum Rapp and Melville (1990)
$TKE\forall$ $TKEA$	$t^{-0.98}$	$t^{-0.94}$	$t^{-1.00}$
$\forall(t)$ or $A(t)$	$t^{0.64}$	$t^{0.52}$	$t^{0.50}$
$\overline{U}^2$	$t^{-1.62}$	$t^{-1.46}$	$t^{-1.50}$
ε_b **(4.9)**	$t^{-2.62}$	$t^{-2.46}$	$t^{-2.50}$
ε_b **(4.14)**	$t^{-2.64}$	$t^{-2.45}$	$t^{-2.50}$

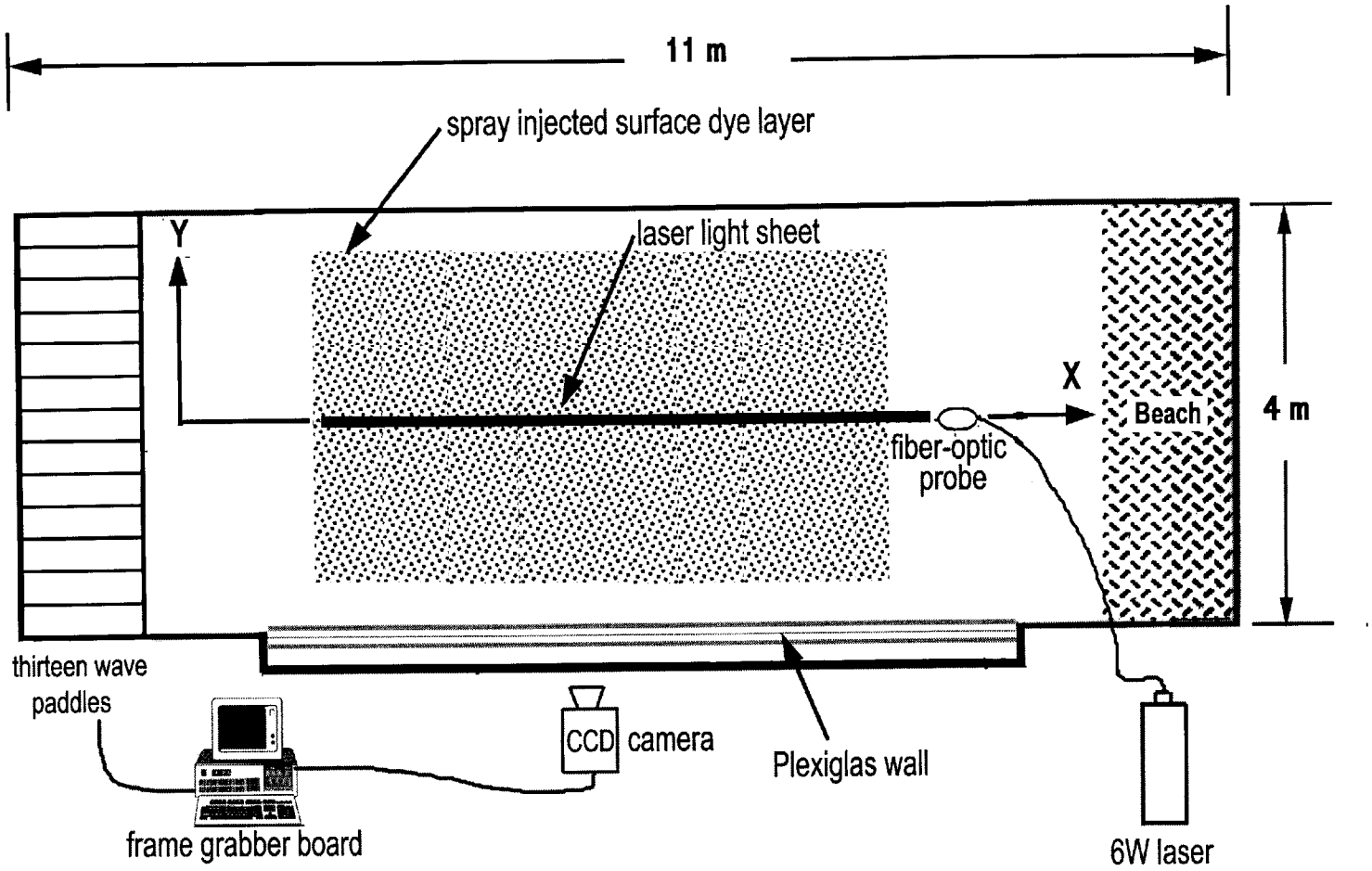

Figure 4.1. Flow visualization experimental setup. Before each experiment, a thin patch of Uranine dye was even spread on the free surface. The dye was illuminated by laser light sheet created by passing 6W argon-ion laser through a fiber optic probe. A water-tight CCD COHU camera was used to capture images of the evolving dye after breaking. The images were acquired by a BitFlow frame grabber board embedded in a Pentium 90 Computer. An external trigger was used to synchronize between the wave paddles and the frame grabber board.

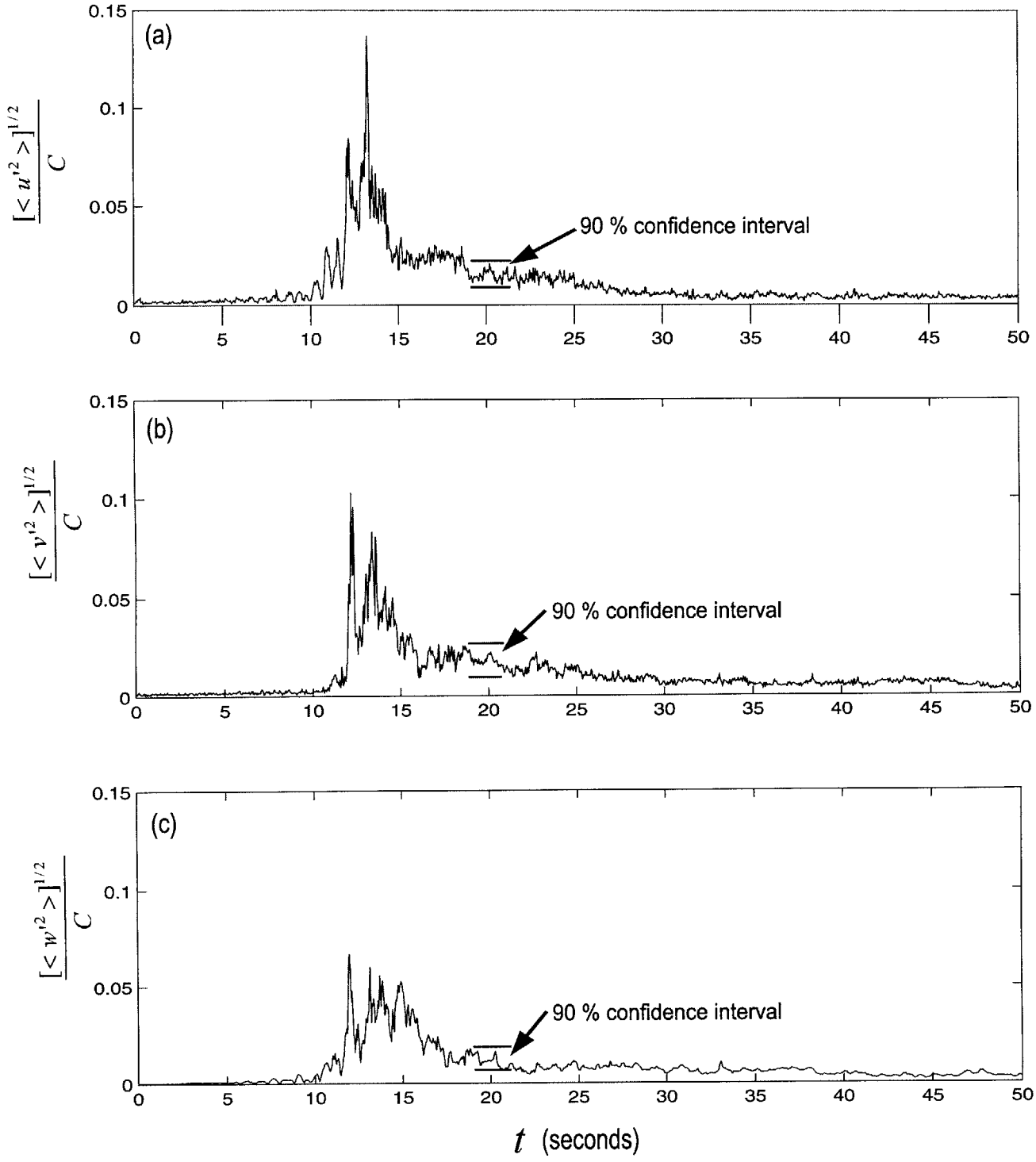

Figure 4.2. The square root of the variance in (a) $[<u'^2>]^{1/2}$, (b) $[<v'^2>]^{1/2}$, and (c) $[<w'^2>]^{1/2}$ versus time.

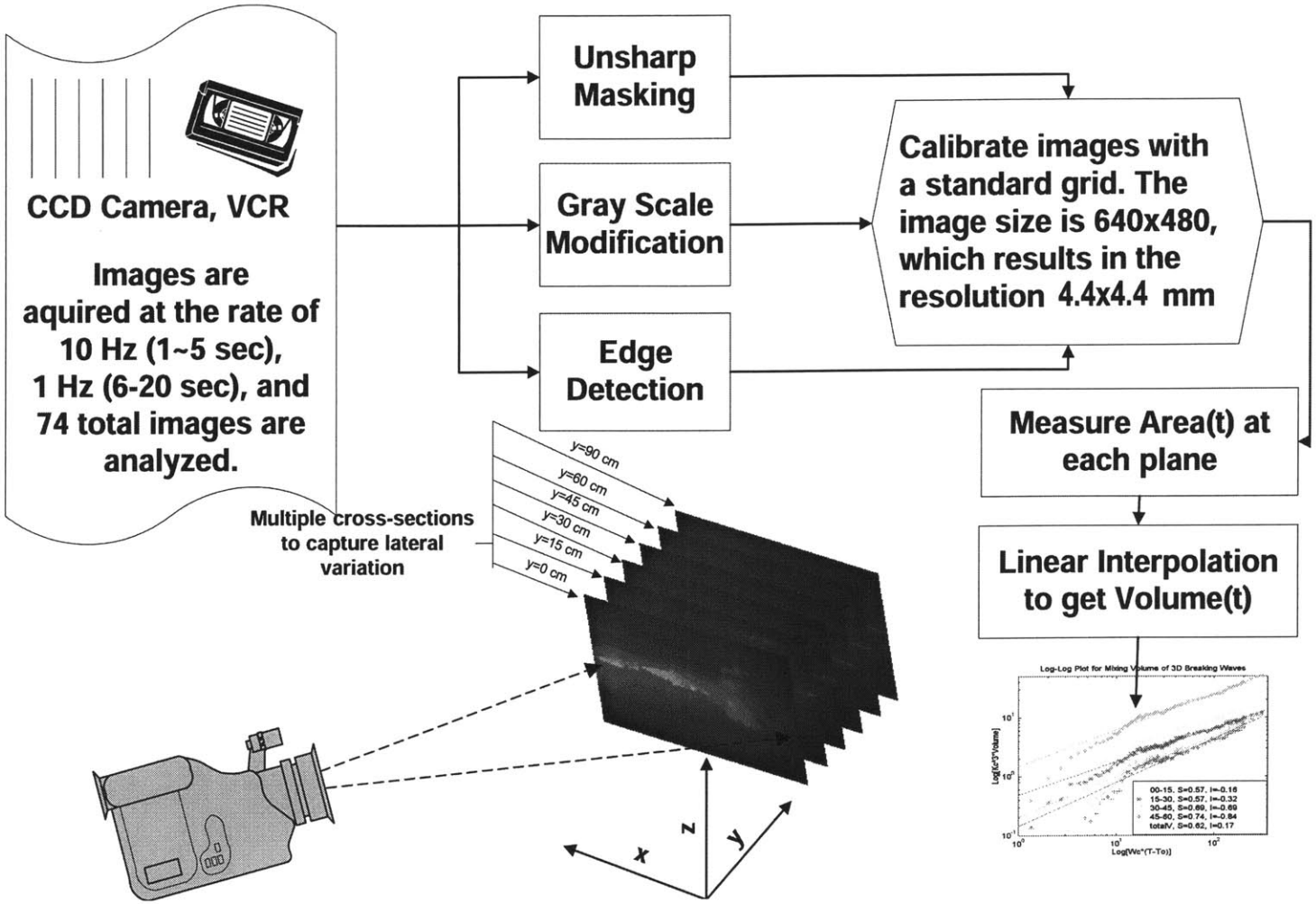

Figure 4.3. Image processing and reconstruction. First, the recorded images are enhanced using image processing techniques, unsharp masking, gray scale modification, and edge detection. Then the enhanced images are correlated with the calibrated board image. The mixing area at each time and on each of the six planes is calculated. Finally the mixing volume is obtained by integrating along the lateral direction and image reconstruction.

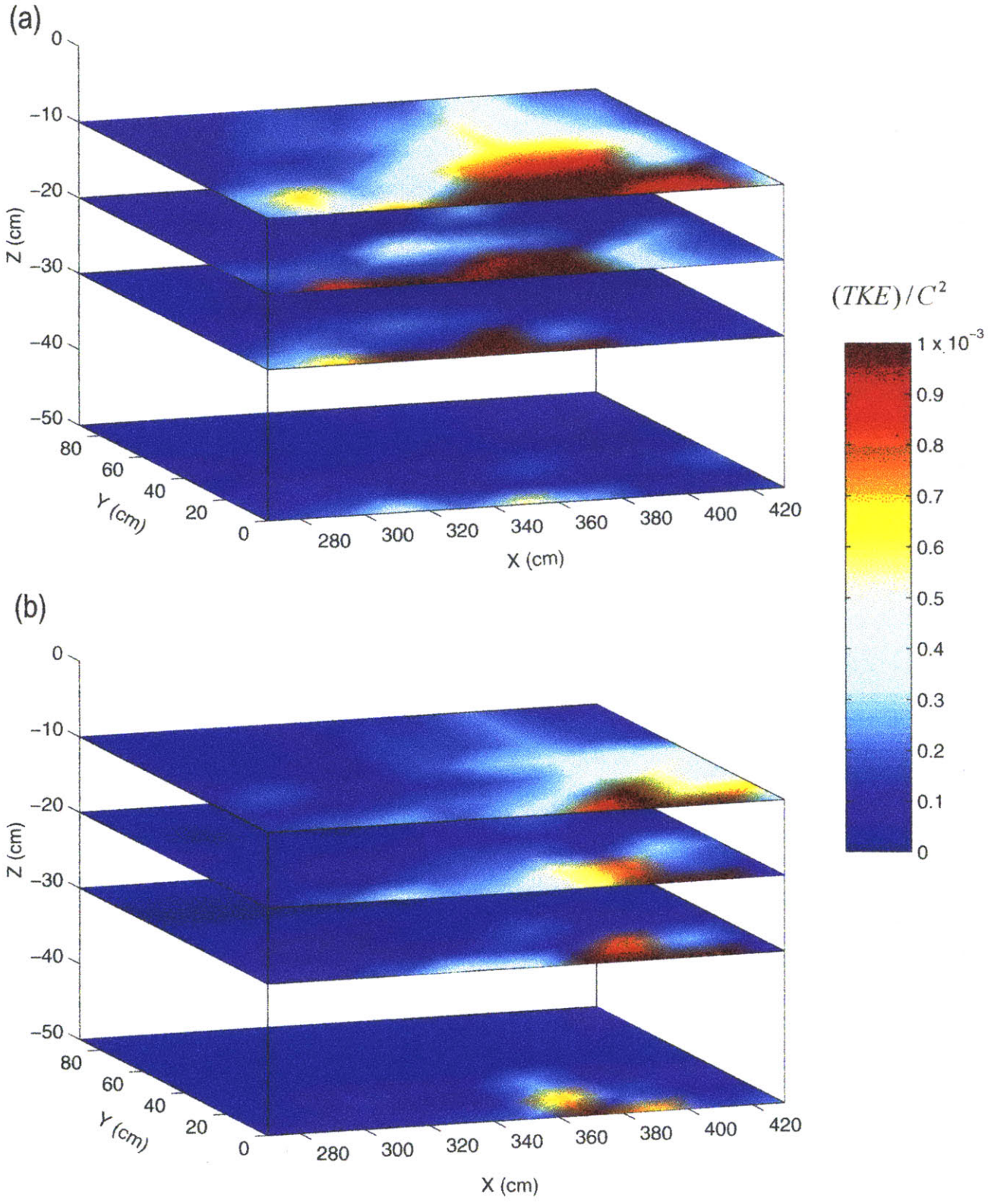

Figure 4.4. Turbulent kinetic energy in the three-dimensional breaking wake at (a) $(t-t_o)f_c=5$ and (b) $(t-t_o)f_c=10$.

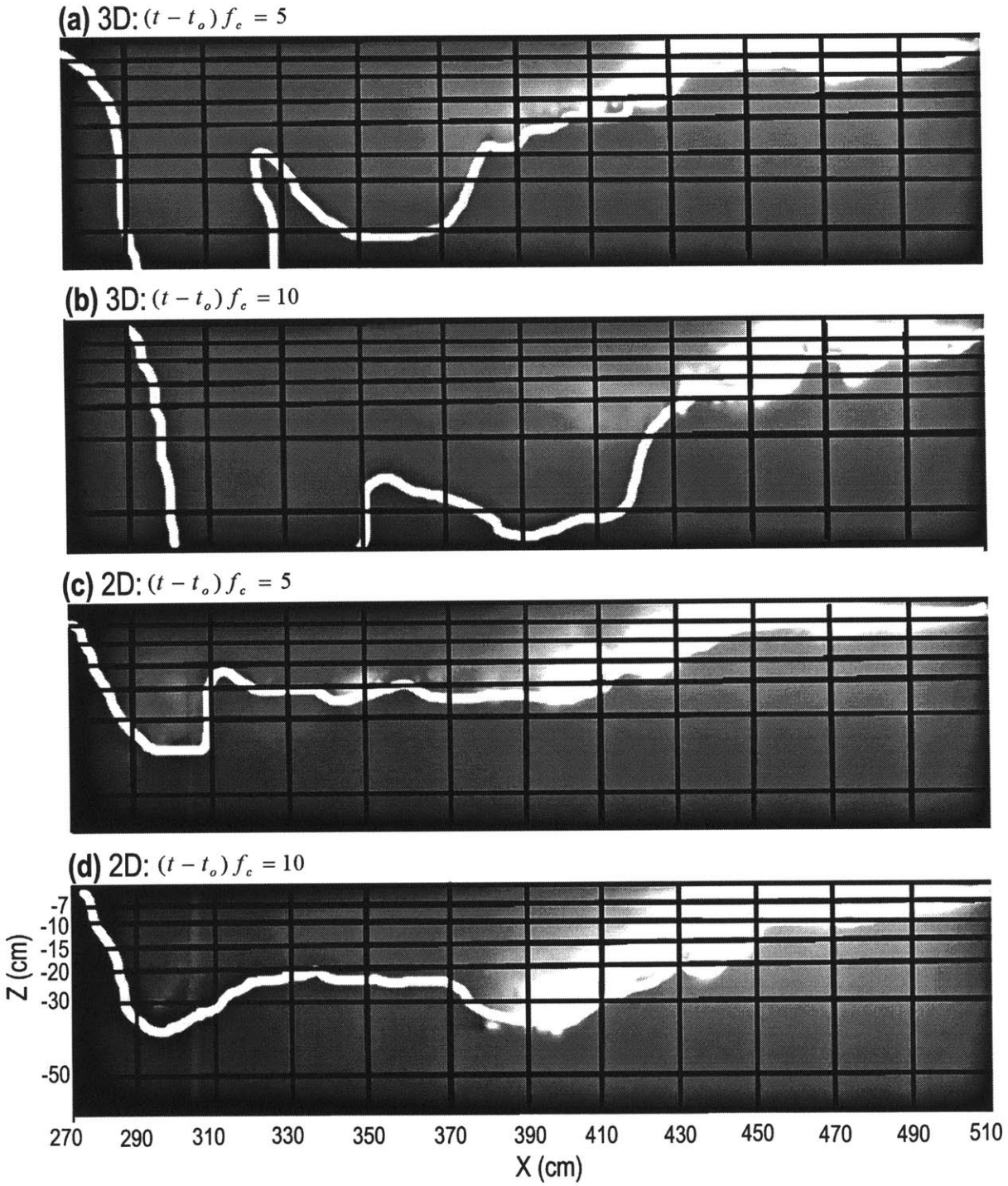

Figure 4.5. Dye mixing area for the 3D (a,b) and 2D (c,d) plunging breaker at y=0 cm.

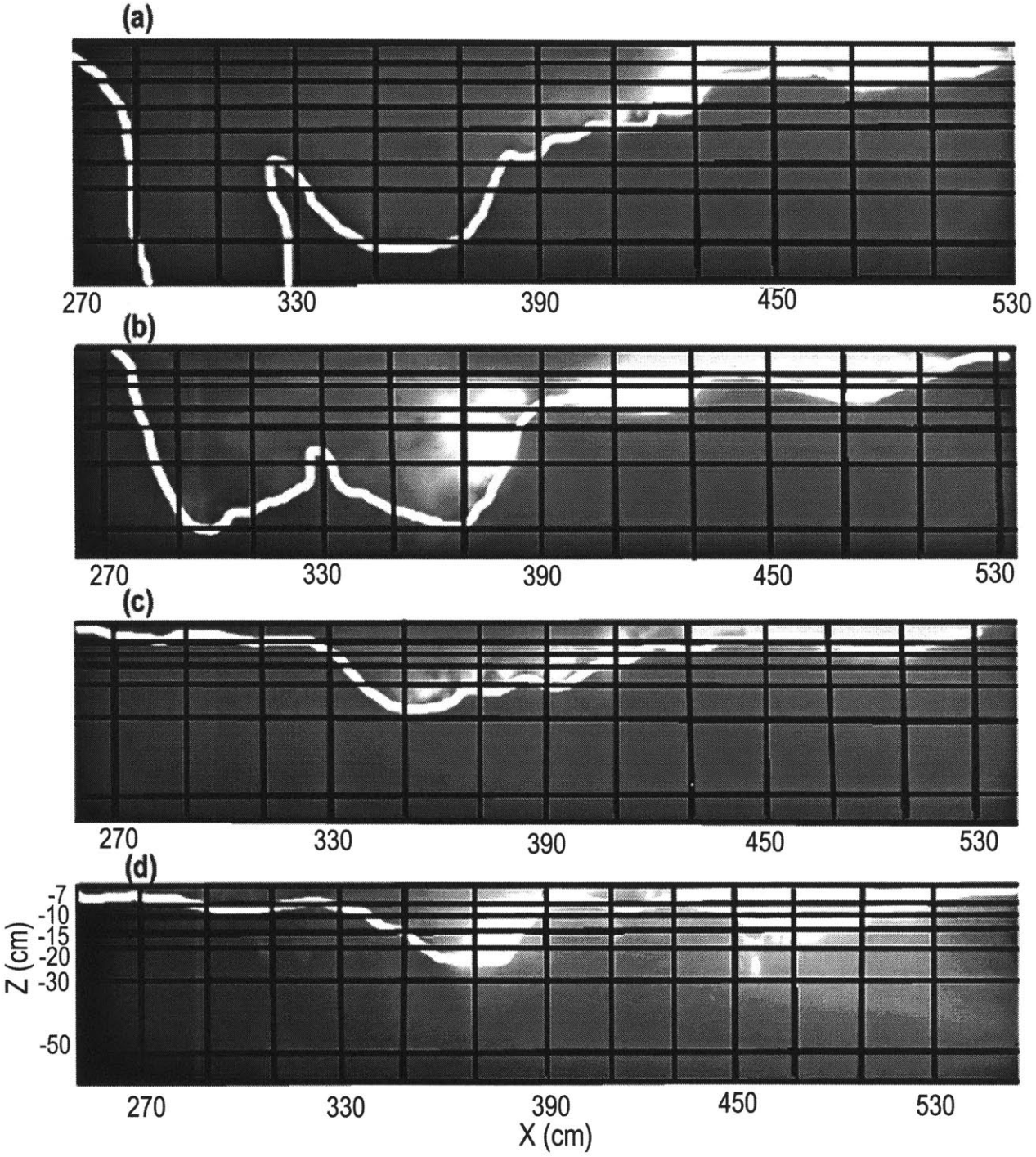

Figure 4.6. Mixing area at lateral positions y = (a) 0, (b) 30, (c) 60, and (d) 90 cm after the three-dimensional plunger breaks at $(t - t_o) f_c = 5$. Note that the scale at each lateral plane is different because the distance between the each plane and the camera varies.

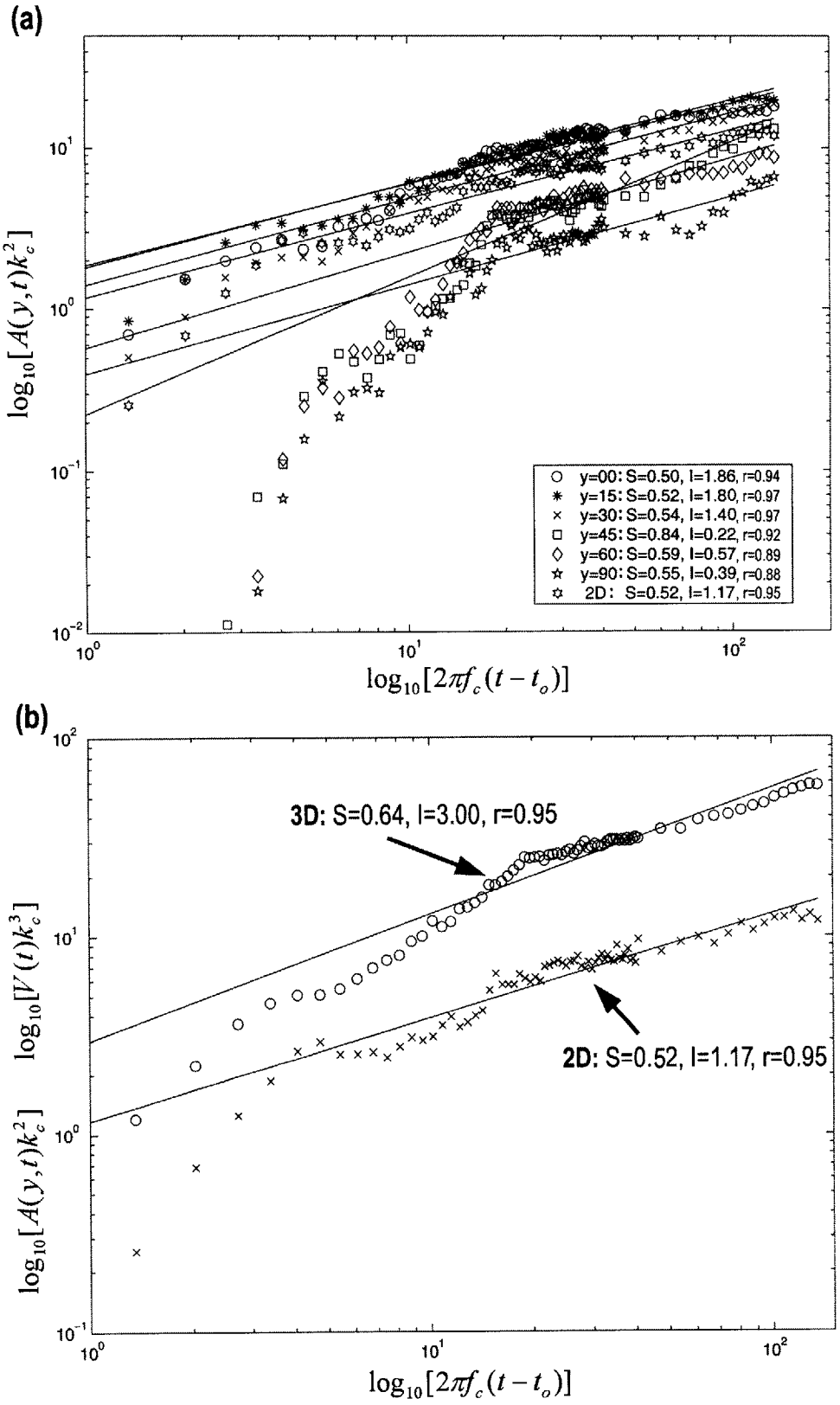

Figure 4.7. Log-log plot of (a) mixing area, $A(y,t)$, and (b) mixing volume, $\forall(t)$, versus nondimensional time. The data are fitted using a straight linear line with the slope, S, and the intercept, I. The correlation cofficient, r, indicates the performance of linear relationship.

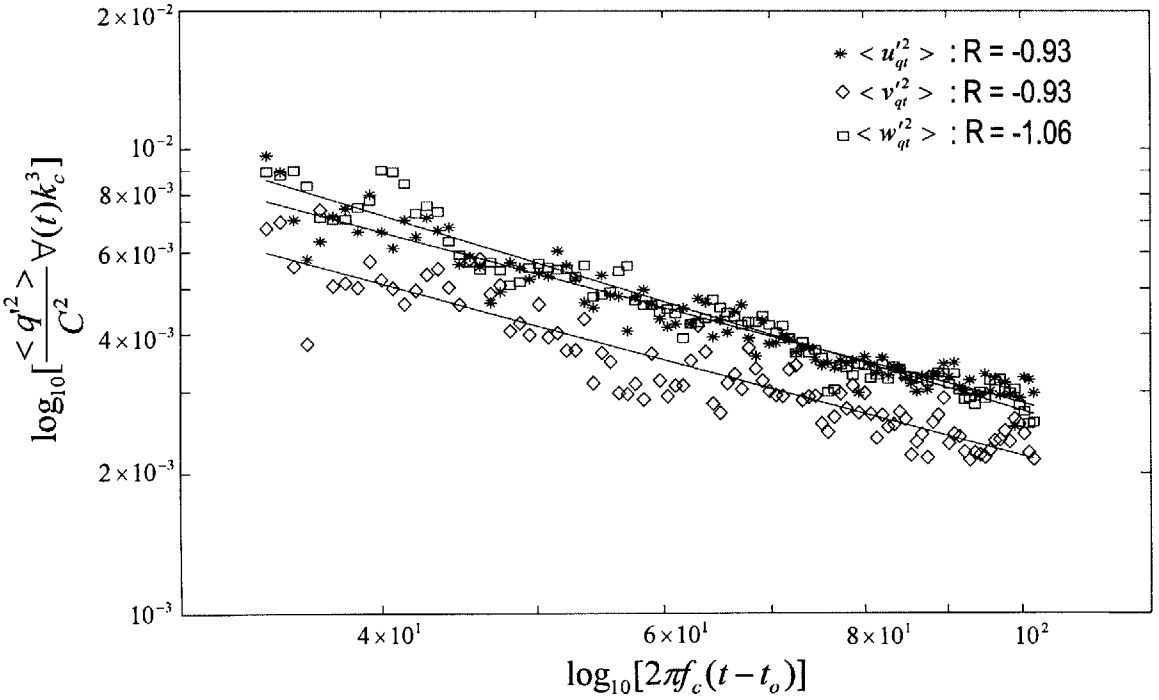

Figure 4.8. The decay of volume integrated turbulent kinetic energy in $< u'^2_{qt} > (*)$, $< v'^2_{qt} > (\diamond)$, and $< w'^2_{qt} > (\square)$ components. The data is fitted using a straight linear line with the slope R.

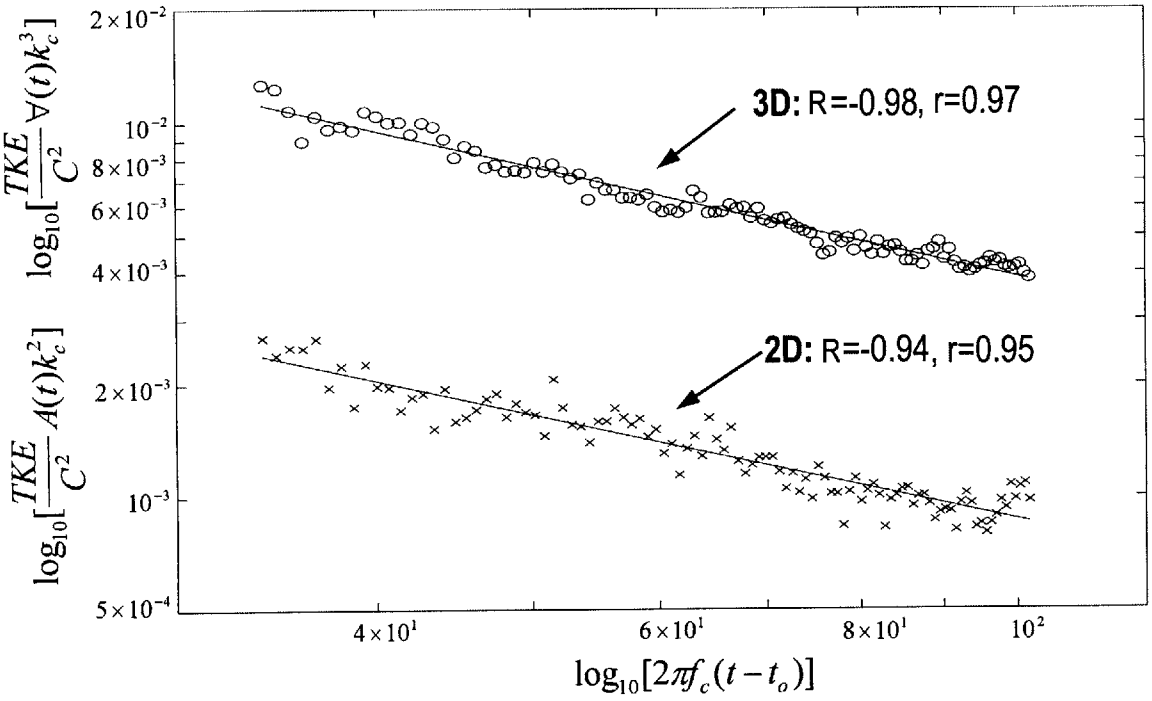

Figure 4.9. The decay of 3D volume and 2D area integrated turbulent kinetic energy. The data is fitted using a straight linear line with the slope R. The correlation cofficient, r, gives the performance of linear relationship.

Chapter 5: Summary

This thesis has reported a series of laboratory measurements of three-dimensional breaking waves. The primary motivations for this research are to provide quantitative analysis and to examine the geometric evolution, the kinematic and dynamic processes of unsteady three-dimensional deep-water breaking waves. To the best of our knowledge, the detailed measurements for surface displacement, velocity, and turbulent mixing are the first laboratory study to address the complexity of three-dimensional, unsteady deep-water breaking waves. The important findings related to the six proposed issues including breaking wave criteria, energy losses, induced surface currents, vorticity generation, turbulent mixing and dissipation rate due to breaking are summarized as follows:

- A new wave generation technique that combined spatially and temporally constructive interference was developed to investigate the effects of wave directionality on three-dimensional wave breaking. The technique proved to be able to generate a very repeatable, isolated, unsteady, three-dimensional breaking event within a wave group. This wave generation allows us to repeatedly measure an identical breaking event.

- Using the Hilbert transform, the present experiments show the kinematic criteria ratio $|\vec{U}|/C$ not only detects breaking locations along a wave crest

but also reveals variation in breaking intensity. Specifically, the ratio differentiates directional plunging and spilling with $|\vec{U}|/C \geq 1.5$ and $|\vec{U}|/C \geq 1$, respectively. Moreover, we show that the effects of wave directionality can significantly increase the geometric breaking criteria in focusing waves or decrease it in diffracting waves. Although the directionality of waves does not alter dynamic breaking criteria that exhibit up-frequency transfer associated with wave steepening, the proposed dynamic criteria are sensitive to the choice of reference locations.

- The spatially focusing and diffracting, three-dimensional wave-packets respectively lose 34% and 18% of their energy as a result of plunging breakers, and 12% and 9% as a result of spilling breakers. Comparable two-dimensional breakers with the same spectral shape lose 16 % for plunging and 12% for spilling. This observation suggests that wave directionality can play an important role in determining breaking losses.

- The three-dimensional plunging breaker can generate non-uniform currents, which is not observed in the two-dimensional breaker. Specifically, at the centerline, the generated current is $0.12C$ initially and persists to $0.02C$ after thirty wave periods from breaking. At the flank of the breaker, the generated current is $-0.01C$ and decays slowly to $-0.005C$ after thirty wave periods

from breaking. The generated currents penetrate to the depth of 3 ~ 4 wave heights, which is twice the penetration depth achieved by the induced currents of two-dimensional breaker. The penetration depth generated by the three-dimensional plunging breaker is also consistent with those in field observations.

- The three dimensional plunging breaker generates vertical as well as lateral vorticity with initial intensity f_c and slowly decays to $0.3 \sim 0.4 f_c$ after ten wave periods from breaking. As far as we are aware, this is the first laboratory result that supports the field observations and the theoretical conjectures for the existence of vertical vorticity due to a finite length of three-dimensional breaking. An explanation for vorticity evolution induced by the three-dimensional breaking is proposed (Figure 3.10).

- Turbulent kinetic energy, $2.5 \times 10^{-3} C^2$, is generated by the three-dimensional plunging breaker at the surface of the centerline and decays to $0.5x10^{-3} C^2$ at the depth of 3 ~ 4 wave height. Away from the centerline, the strength and penetration of turbulent kinetic energy decrease as the plunging breaker turns into a spiller. As time goes on, the turbulent wake spreads laterally as it further advects downstream, creating a teardrop shaped patch. This laboratory

observation is believed to be the first study to verify the conjectured turbulent wake shape (Thorpe 1995).

- The three-dimensional plunger can penetrate the surface dye layer to the depth of 3 ~ 4 wave heights, consistent with the penetration depth of small bubbles generated by the breaking in the field. The active roller eddies generated by the three-dimensional plunger also increase the turbulent wake and mixing as time goes on. A flow visualization technique is developed to examine the growth of mixing volume for the three-dimensional plunger. It is found that the turbulent wake generated by the three-dimensional plunging breaker grows more rapidly than that by two-dimensional breaker.

- The dissipation rate due to the three-dimensional breaking $(\varepsilon_b)_{3D} \propto t^{-2.62}$ is higher than that due to two-dimensional breaking, $(\varepsilon_b)_{2D} \propto t^{-2.46}$. This result supports the argument that the three-dimensional turbulence is more dissipative than that of the two-dimensional turbulence. Finally, a time varying eddy viscosity, $t^{\frac{-(3R_1+R_2)}{6}}$, for three-dimensional breaking waves is proposed. This result provides the ground for future study of the temporal evolution of the turbulence in the field and wind-wave numerical modeling.

Appendix A: A Comparison of Two- and Three-Dimensional Wave Breaking

H. M. NEPF AND C. H. WU

Department of Civil and Environmental Engineering, Massachusetts Institute of Technology, Cambridge, Massachusetts

E. S. CHAN

Department of Civil Engineering, National University of Singapore, Singapore

(Manuscript received 24 January 1997, in final form 8 October 1997)

ABSTRACT

The influence of directionality on wave-packet evolution and in particular on the onset of breaking was explored through laboratory experiment. Lateral tapering was applied to the input signal to produce a range of crest lengths, with greater directionality created by diffraction for the shorter crests. The wave shape, local and global wave steepness, and surface displacement spectra were used to characterize the wave fields. The observations suggest that directionality can accelerate or suppress the onset of breaking, and additionally can influence both the local wave steepness at breaking as well as the breaking severity. Directionality, however, did not alter the observed up-frequency energy transfer associated with wave focusing. When no breaking occurred this energy shift was completely reversed. With breaking the shifted energy was lost, that is, passed from the wave to the turbulent energy field. The short-crested wave packet lost 16% of its energy as a result of breaking, while a comparable two-dimensional breaker lost 22%.

1. Introduction

Oceanic wave breaking provides an important conduit for the exchange of gas, water vapor, energy, and momentum between the atmosphere and the ocean (Melville 1996). These exchanges affect the growth of wind waves (Phillips 1977), the generation of bubbles and sea spray (Johnson and Cooke 1979; Thorpe 1993), the formation of surface currents (Longuet-Higgins 1969; Mitsuyasu 1985; Melville and Rapp 1988; Rapp and Melville 1990), and the generation and distribution of near-surface turbulence (Koga 1982; Blanchard and Woodcock 1980; Gargett 1989; Thorpe 1995). Recent studies have also shown that breaking waves may retard global warming by increasing CO_2 fluxes to the ocean (Bryan and Spelman 1985; Csanady 1990). In addition, the forces associated with freak wave breaking threaten both offshore structures and ships (Kjeldsen and Myrhaug 1994; Chan and Melville 1988; Greenhow and Vinje 1982). In view of the many important consequences of wave breaking, it is crucial to have a fundamental understanding of this process and, in particular, to have the ability to predict the onset of breaking events and their severity in terms of energy loss.

Corresponding author address: Dr. H. M. Nepf, Department of Civil and Environmental Engineering, Massachusetts Institute of Technology, Room 48-425, Cambridge, MA 02139.
E-mail: hmnepf@mit.edu

Over a century ago theorists began to examine the limits of wave stability. Using a breaking criteria based on the crest particle velocity exceeding the phase speed, the breaking limit of the two-dimensional Stokes wave was shown to occur at a wave steepness, $ak = 0.443$, and crest angle 120°, where a is wave amplitude and k is wavenumber (Stokes 1880; Michell 1893; Havelock 1918). However, theoretical and experimental results have since shown that finite amplitude Stokes waves, given sufficient fetch, are unstable at much lower steepness due to the growth of two forms of instability, longitudinal (Type I) and lateral (Type II) modulation (Benjamin and Feir 1967; McLean 1982; Longuet-Higgins 1985a). For an initial steepness $a_0k_0 > 0.25$ the evolution of lateral modulation can lead to three-dimensional spilling breakers (Melville 1982; Su 1982; Su et al. 1982).

A variety of other wave forms have been examined experimentally. For example, steady waves created by towed hydrofoils have a breaking onset of $H/L = 0.10$, where H and L are the local wave height and length, respectively (Duncan 1981, 1983). Assuming a symmetric wave, this steepness value is roughly equivalent to $ak = 0.31$. In contrast, for quasi-steady breakers generated between convergent walls the observed onset criteria was $H/L = 0.132$, or $ak = 0.41$ (Ramberg and Griffin 1987). The difference in these results suggests that a breaking onset criteria based on local wave steepness is sensitive to the process of wave generation.

Field and laboratory studies have shown that, as a

wave approaches breaking, the wave profile becomes both horizontally and vertically asymmetric, and so deviates from the symmetric profile of the theoretical wave shape (Kjeldsen and Myrhaug 1979; Bonmarin 1989; Tulin and Li 1992). Most notably the front of the crest becomes steeper than the rear, reflecting an intrawave energy shift; that is, the energy of the crest and front simultaneously increase at the expense of the trough and back (Bonmarin 1989; Tulin and Li 1992). The local steepness ak, while appropriate for the theoretical, symmetric wave, is inappropriate for the characterization of real waves because it cannot reflect this profile asymmetry. To capture the asymmetry a new wave-shape parameter was introduced, the front-crest steepness, ε (Kjeldsen and Myrhaug 1979). Unfortunately, the new steepness parameter was only marginally better than ak in terms of providing a stable breaking criteria (Kjeldsen and Myrhaug 1979). Indeed, the range of limiting steepness observed in the field, ε = [0.32 to 0.78], suggests that this single point characterization of local wave shape is not capable of discerning the physical limits of breaking.

Rapp and Melville (1990) considered a global spectrum-based steepness, ak_c, to describe the breaking onset for two-dimensional, unsteady breakers generated through wave–wave interaction within frequency-modulated wave packets. Here, a is the sum of the component amplitudes a_n, and k_c the wavenumber of the center frequency. For a top-hat spectrum, that is, constant component amplitude, the onset of breaking was observed at $ak_c = 0.25$. In addition, ak_c was shown to have reasonable correlation to breaker severity as measured by fractional energy loss, which ranged from 10% for spilling breakers up to 25% for plunging breakers. Using the same wave generation technique, Chaplin (1996) compared two different spectral forms, a constant component amplitude and a constant component steepness, and found different onset criteria $ak_c = 0.265$ and 0.30, respectively, indicating that the breaking onset criteria based on ak_c are sensitive to spectral shape.

Theorists and field investigators have also considered breaking criteria based on the downward acceleration at the crest (Penney and Price 1952; Taylor 1953; Phillips 1958). For the almost highest wave, Longuet-Higgins (1986) has shown that the Eulerian (apparent) acceleration in the crest tends to infinity, but that the Lagrangian (real) acceleration is limited to $-0.388g$. To apply these results to the field one must consider the affect of unsteadiness. Longuet-Higgins (1985b) suggested that unsteady waves may be considered as the superposition of steady, progressive waves of differing frequency. The constructive interference leads to higher accelerations at the crest for lower overall steepness, suggesting that unsteady waves break at lower overall steepness than do steady waves. This result, however, does not consider the effect of wave-field directionality.

As a simplification for directional wave fields, She et al. (1994) and Kolaini and Tulin (1995) specifically explored the influence of spatial focusing. Both studies demonstrated that, as the angle of wave interaction increased (0° corresponding to a planar wave front), both the breaking height and the breaking severity also increased. Interestingly, this trend is counter to that suggested for the superposition of unidirectional, multifrequency progressive waves, described above. However, the observed increase in breaking steepness with focusing angle is consistent with Penney and Price (1952), who used a limiting acceleration criteria to predict that the breaking steepness of a standing wave, that is, maximum focusing angle, exceeds that of a progressive wave by 50%. Taylor (1953) verified this prediction qualitatively in a laboratory tank, but suggested that three-dimensional modulation, which appeared as the predicted limiting wave height was approached, assisted in the precipitation of breaking.

Field observations, which correlated photographic images of whitecapping to vertical acceleration within a directional wave field, support a breaking criteria of $-0.5g$ (Snyder et al. 1983). In contrast, other investigations of random, deep-water wave fields have suggested threshold values of $-0.39g$ (Ochi and Tsai 1983), $-0.34g$ (Dawson et al. 1993), and $-0.32g$ (Longuet-Higgins 1985b). The discrepancy between these different observations may be attributed to differences in Eulerian and Lagrangian observational methods, as well as to the influence of multiple frequency superposition and directionality on real crest acceleration.

The experiments described in this paper were intended to build on several of the above studies by further examining the details of breaking within a directional wave field. The study provides a direct comparison of the evolution and breaking criteria for spectrally similar two- and three-dimensional wave packets created through frequency focusing. To contrast the directional focusing explored by She et al.(1994) and Kolaini and Tulin (1995), this study explored the influence of passive directional spreading (diffraction), and demonstrates that both the local breaking steepness (§3a) as well as the breaking severity (§3d) are diminished under conditions of diffraction. This is complementary to previous observations of increasing breaking steepness and severity with increasing wave focusing (She et al. 1994; Kolaini and Tulin 1995). In addition, the limiting spectrum-based steepness increased with increasing diffraction, suggesting that breaking may be suppressed in a strongly diverging field (§3b). Directionality, however, did not influence the up-frequency shift in wave energy associated with the approach to breaking (§3c).

2. Experimental methods

a. Wave generation

The present study was conducted in a 4 m × 11 m test section within the Gunther Family Wave Basin at the Massachusetts Institute of Technology. The mean

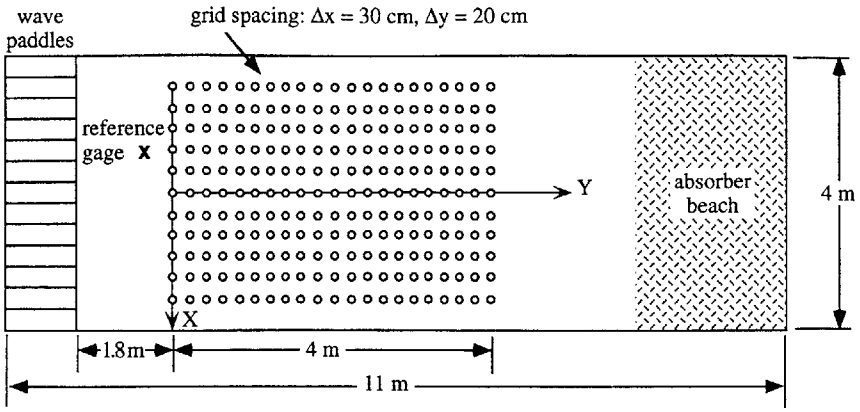

FIG. 1. Top view of test section. Circles indicate the locations of surface displacement measurements. To verify repeatability and to synchronize different runs a reference gauge was maintained at $y = -20$ cm, $x = -30$ cm.

water depth was $h = 0.6$ m. The waves were generated using 13 independently programmed and hydraulically driven paddles, each 30 cm wide. A coordinate system was chosen with y as the longitudinal direction and $y = 0$ at the first measurement position; x as the lateral direction and $x = 0$ at the midpoint of the test section, $z = 0$ at the mean water level and positive upward. The breaking events occurred within a 4 m × 4 m measurement area (Fig. 1), which began 180 cm (=3 h) from the mean position of the paddles to avoid interference from the evanescent modes associated with the paddles (Dean and Dalrymple 1984).

A single, unsteady breaker can be generated using frequency focusing. This technique, based on the constructive interference of dispersive wave components, was first used by Cummins (1962) and Davis and Zarnick (1964) for testing ship models. Greenhow and Vinje (1982) and Rapp and Melville (1990) have also used this technique to generate individual, isolated breakers within a wave packet. The technique mimics the wave–wave interaction, which is believed to be the fundamental process producing unsteady breaking in the field (Tulin and Li 1992). It is important to note, however, that other mechanisms such as wave–current interaction (Kjeldsen and Myrhaug 1980), direct wind forcing (Banner and Phillips 1974), and fetch (Su and Green 1985) may also affect the breaking processes. Here, we followed the frequency focusing technique described in Rapp and Melville (1990) but applied a different distribution of component amplitudes a_n, and limited the lateral extent of the wave packet to achieve a short-crested breaker.

To begin, linear wave theory was used to derive the surface displacement required at the paddles, $\eta(y_p, t)$, in order to produce constructive interference and breaking at a prescribed distance y_b measured from the mean position of the paddles:

$$\eta(y_p, t) = \sum_{n=1}^{N} a_n \cos[-k_n y_b - 2\pi f_n (t - t_b)], \quad (1)$$

where t_b is the theoretical time of breaking (maximum focusing), and a_n and f_n are the amplitude and frequency for each of N wave components. Because the wave becomes nonlinear in its approach to breaking, (1) is not strictly valid near the prescribed focal point and the actual point of breaking may occur later than, that is, downstream of, the theoretical value (Baldock et al. 1996). The wavenumber of each component k_n is given by the linear dispersion relation

$$(\omega_n)^2 = k_n g \tanh(k_n h), \quad (2)$$

where g is the gravitational constant, and the radian frequency, $\omega_n = 2\pi f_n$. The surface displacement may then be described by the variables N, a_n, f_n, y_b, t_b, and k_n, defined for each paddle, and the global parameters h and g. These variables can be reduced to a shorter set of dimensionless parameters as follows.

The spectrum parameters were chosen to produce a specific spectral shape that mimics the high-frequency tail of the wind wave spectrum, f^{-5} (Phillips 1958). The number of wave components N was chosen at 32 in order to approximate a continuous spectrum. The 32 components, f_n, were equispaced across a bandwidth of Δf and centered at frequency f_c. The component amplitudes were then chosen to produce a constant wave steepness for all wave components; that is,

$$a_n = G/k_n, \quad (3)$$

where G is a scale factor (Loewen and Melville 1991). In contrast to a constant component amplitude, that is, $a_n = \text{const}$, this condition inhibits premature breaking because all components maintain similar scale with regard to steepness.

The intensity of the wave packet can be described in terms of a global, spectrum-based wave steepness, ak_c, defined by Rapp and Melville (1990),

$$ak_c = k_c \sum_{n=1}^{32} a_n, \quad (4)$$

where a_n was defined by (3). The wavenumber of the

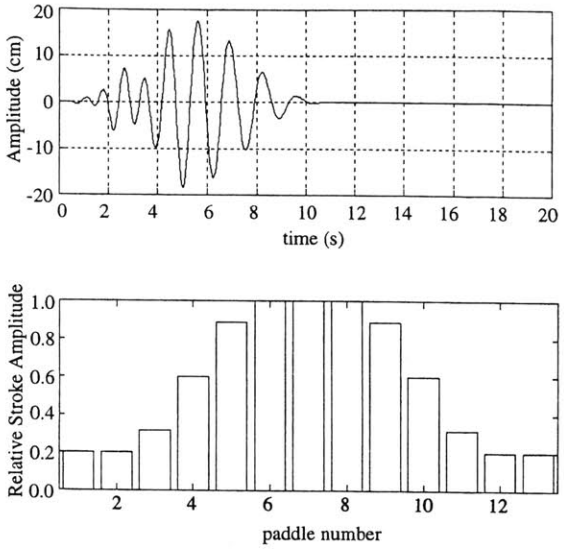

FIG. 2. Input signal of centerline wave paddle (a). To create a short-crested wave packet the centerline signal is tapered to 20% using a cosine window. An example of the taper function is shown in (b).

central frequency k_c is given by f_c and (2). With spectral shape held constant, ak_c was varied through the scale factor G.

To produce a two-dimensional wave, the input signal (1) was identically defined for each of the 13 paddles. To introduce directionality, a limited crest length was created by spatially tapering the individual paddle movements. The central paddles moved together at the maximum amplitude (Fig. 2a) and the remaining paddles were tapered down to 20% using a cosine window (Fig. 2b). This spatial variation mimics field conditions in which local heterogeneity within the wind field produces local heterogeneity within the wave field. By varying the number of central paddles the forced crest length, L_0, was varied from 30 to 150 cm. For the two-dimensional breaker L_0 was effectively infinite. The transverse tapering produced passive directional spreading during wave evolution. The extent of directional defocusing (diffraction) was dependent on both the initial crest length and the distance to breaking, yielding a dimensionless diffraction parameter, y_b/L_0.

The three-dimensional wave packet evolution can now be described by the nondimensional set: (ak_c, y_b/L_0, $\Delta f/f_c$, k_ch). Varied conditions of ak_c and y_b/L_0 were considered in this study. The frequency bandwidth ratio, $\Delta f/f_c$, has been shown to have only a weak influence on breaker onset and severity (Rapp and Melville 1990, Fig. 17), and so was not varied here. A fixed value of $\Delta f/f_c = 0.73$ ($\Delta f = 0.789$ Hz and $f_c = 1.08$ Hz) was selected because it produced the most distinct transition between the spilling and plunging cases (Rapp and Melville 1990). Finally, we considered deep water waves such that the last parameter, k_ch, had little effect on the wave evolution. From the wavenumber $k_c = 4.73$ m^{-1}, $\tanh(k_ch) = 0.99$, indicating a deep water wave condition at the scale of the wave packet.

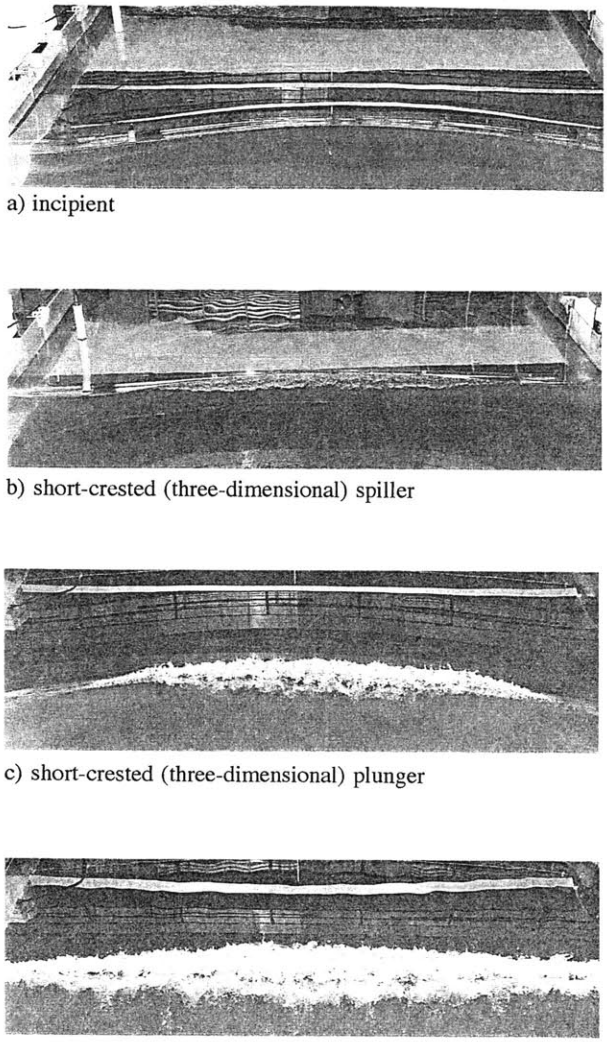

a) incipient

b) short-crested (three-dimensional) spiller

c) short-crested (three-dimensional) plunger

d) long crested (two-dimensional) plunger

FIG. 3. Photograph of the breaking crest taken from above and behind the wave, that is, the crest is moving away from the camera: (a) three-dimensional incipient wave crest, (b) three-dimensional spilling wave crest, (c) three-dimensional plunging crest, and (d) two-dimensional plunging crest.

The limiting conditions for nonbreaking, spilling, and plunging waves were determined as follows. Starting with a nonbreaking wave, the gain was slowly increased for successive runs, producing a nonbreaking, spilling, and finally a plunging wave. The wave was classified as nonbreaking if the free surface remained visually smooth throughout the run (Fig. 3a). The largest steepness at which a nonbreaking wave was observed was defined as the incipient breaking criteria. At larger values of ak_c a slight spilling began at $y_b = 420$ cm, manifest in a ruffled surface appearance along the central wave crest (Fig. 3b). Increasing ak_c further eventually produced a second breaker at $y_b = 300$ cm, that is,

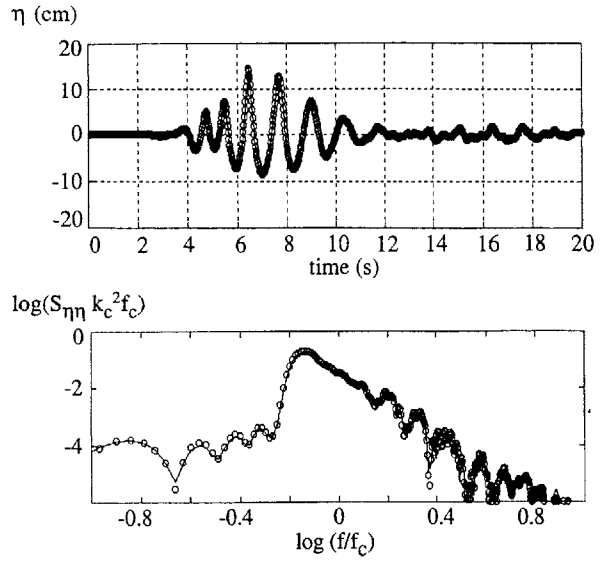

FIG. 4. (a: top) The records of surface elevation measured at the reference gauge are compared for run number 5 (open circles), corresponding to the gauge array positioned at $y = 80$ cm, and run number 12 (solid line), corresponding to the gauge array positioned at $y = 180$ cm. The records demonstrate the excellent repeatability of the wave-packet conditions. (b: bottom) The spectra of the records shown in (a). The total energy of the individual wave packets agree to within 1%.

upstream of the original spiller. The onset of this upstream wave was chosen as the spilling criteria as it represents the strongest individual spiller that could be produced within the wave packet. Finally, ak_c was increased to the point at which the upstream breaker became a plunger (Fig. 3c), and the downstream spiller disappeared. This condition represented the weakest plunger that could exist alone, that is without a secondary breaker downstream. The two-dimensional plunger (Fig. 3d) was similarly selected, but with uniform paddle forcing ($y_b/L_0 = 0$).

b. Free surface displacement

The surface displacement was recorded for 40 seconds at 40 Hz using 4-mm diameter, resistance-type wave gauges. Wave records were measured at 126 grid positions spaced 30 cm in the lateral (x) direction, and 20 cm in the longitudinal (y) direction (see Fig. 1). A tighter spacing was chosen for Δy to capture the more rapid spatial variation. A carriage system holding six wave gauges was used to traverse the measurement grid. Allowing for symmetry across the centerline, the entire test section could be scanned using 21 runs. Between each run the basin was required to settle for 15 minutes to eliminate all previous surface motion.

Before each testing session the following measurements were made to verify the experimental conditions and to minimize error. First, the wave gauges were calibrated and the accuracy, ± 0.2 mm, confirmed. Second,

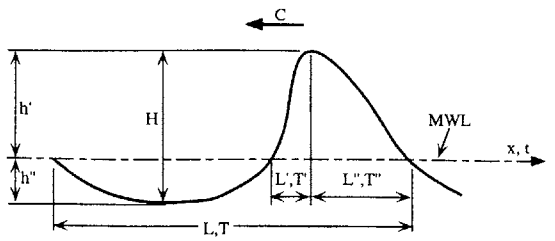

FIG. 5. A definition sketch for the determination of crest-front steepness, $\varepsilon = \eta'/L' = (2\pi\eta')/(gTT')$, where T is the observed wave period, and T' is the time interval associated with the passage of the front crest region defined as the interval between the passage of the crest-front zero crossing and the wave peak. Taken from She et al. (1994)

pairs of surface elevation records, $\eta(t)$, measured at symmetric positions on either side of centerline were compared to verify the centerline symmetry. The mean-square deviation between records at several longitudinal positions matched to within 1%–2%, confirming symmetry. Third, to test the repeatability of wave generation and to synchronize the multiple wave records, a stationary reference wave gauge was maintained at the position ($y = -20$ cm, $x = -30$ cm). For any two runs the surface displacement record at the reference gauge were essentially indistinguishable (e.g., Fig. 4a). In addition, the spectra and the total spectral energy observed at the reference gauge agreed between any two runs to within 1% (Fig. 4b). Finally, the influence of beach reflection was evaluated for steady waves at the central frequency by comparing wave records at three gauges unevenly spaced along the channel (Rosengaus-Moshinsky 1987). Extrapolating these results to the wave packet, we determined that reflection contributed less than 5% error to the estimation of local wave-packet energy.

c. Wave shape parameters

Two wave shape parameters were considered. First, the wave steepness ak_c was used to characterize the potential steepness of a wave within a modulated wave packet based on the steepness of the spectral components. It represents a global estimate of the wave steepness and was evaluated from (3) and (4) above. Second, a local wave steepness was estimated using the temporal records of surface displacement at each wave gauge. To capture crest asymmetry, the front crest steepness was chosen to represent the local wave shape (Kjeldsen and Myrhaug 1979; Bonmarin 1989). The crest front steepness, $\varepsilon = \eta'/L'$, was evaluated as

$$\varepsilon = \frac{2\pi\eta'}{gTT'}, \tag{5}$$

where η', L', T, and T' are defined in Fig. 5.

d. Spectral analysis

At each measurement position the surface displacement spectra $S_{\eta\eta}$ was calculated for the wave packet, which was isolated from the extended record by a tapered window. Zero padding was applied to extend the record for a 4096 point FFT with a 256 point smoothing filter. The resulting spectra were used to evaluate the intrawave harmonic exchange associated with changes in wave shape, in particular the increasing steepness and asymmetry observed as the wave focuses and approaches breaking. To more clearly evaluate these changes, the spectrum was divided into two frequency bands. The principle frequency band, 0.7–1.5 Hz, corresponded to the input signal. Upshifted energy was observed in a second band of frequencies, 1.5–3.0 Hz. The energy content of each frequency band, E_1 and E_2, was estimated by integrating the spectrum over the corresponding frequency range. Changes in E_1 and E_2 were used to interpret cross-frequency exchanges of energy, as well as diffraction effects.

e. Energy fluxes

As the wave packet propagated downstream changes in local wave-packet energy arose from diffraction, viscous dissipation in the wall- and bottom-boundary layers, and breaking. Diffraction, resulting from the lateral variation in wave energy, contributes a net loss (or gain) only within a longitudinal slice of limited lateral extent. If the entire basin width is considered, then diffraction merely redistributes wave energy, contributing no net loss from the width-averaged wave packet. Thus, to eliminate diffraction from the energy budget, we chose a control volume that spans the basin width, $-b/2 < x < b/2$; is bound from below by the basin bottom, $z = -h$; is bound from above by the free surface, $z = \eta$; and finally is bound by the longitudinal positions of $y_1 = 0$ and $y_2 = 4.0$ m. This control volume roughly corresponds to the measurement grid points shown in Fig. 1. Using laterally averaged quantities, we write the following conservation equation (Mei 1983):

$$\frac{\partial E}{\partial t} + \frac{\partial F}{\partial y} = -\rho \overline{\int_{z=-h}^{\eta} (e + e_b)\, dz}, \qquad (6)$$

where e is the rate of viscous dissipation within the sidewall and bottom boundary layers, and e_b is the rate of energy loss due to breaking, both per unit volume, and ρ is the fluid density. The overbar represents a time average over the wave-packet interval, t_1 to t_2, where t_1 occurs before the arrival of and t_2 occurs after the departure of the wave packet. The laterally averaged energy density E and energy flux F are defined by

$$E = \int_{x=-2m}^{x=+2m} \overline{\int_{z=-h}^{\eta} \rho\left(\frac{1}{2}(u^2 + v^2 + w^2) + gz\right) dz}\, dx \qquad (7)$$

$$F = \int_{x=-2m}^{x=+2m} \overline{\int_{z=-h}^{\eta} \left(p + \frac{1}{2}\rho(u^2 + v^2 + w^2) + \rho g z\right) v\, dz}\, dx \qquad (8)$$

with the velocity field (u, v, w) corresponding to the directions (x, y, z), respectively. The analysis is completed by integrating over the control volume length, y_1 to y_2:

$$\int_{y_1}^{y_2} \frac{\partial E}{\partial t}\, dy + \int_{y_1}^{y_2} \frac{\partial F}{\partial t}\, dy = -\int_{y_1}^{y_2} \rho \int_{x=-2m}^{x=+2m} \overline{\int_{-h}^{\eta} (e + e_b)\, dz}\, dx\, dy$$

$$\Delta F = [e]_T + [e_b]_T. \qquad (9)$$

If we assume that all mean currents and turbulence generated by the breaking are contained within the control volume, then the motions at y_1 and y_2 are purely wave. Then, at t_1 (before the arrival of the packet) and at t_2 (after the packet has passed by) the wave energy, $E = 0$ at both y_1 and y_2, and the first term in (9) is zero. This assumption is supported by observations of dye tracer injected into the water column and observed with an underwater camera. The tracer indicated that mean currents initiated by the breaking event were contained between y_1 and y_2 during the time t_1 to t_2. The second term in (9) is the net difference in total wave energy flux at the longitudinal boundaries of the control volume, for simplicity ΔF. The third term is the net loss of energy from the wave packet due to both viscous dissipation $[e]_T$ and breaking $[e_b]_T$.

The evaluation of (9) requires detailed temporal and spatial measurement of the velocity and pressure fields in addition to the surface displacement. However, reasonable flux estimates may be made using surface displacement only. The second-order estimate of the energy flux associated with the wave motion is given by $F = C_g E$. If the wave motion at y_1 and y_2 is at most weakly nonlinear then an equi-partition of potential and kinetic energy may be assumed and the local energy density may be given as $E = \rho g \overline{\eta^2}$, where $\overline{\eta^2}$ is the surface displacement variance. To construct comparative flux estimates along the channel using $\overline{\eta^2}$ alone we must additionally assume that the group velocity C_g is constant along the channel. This assumption, however, is not strictly true, as surface displacement records indicated a 12%–18% downshift in phase velocity after breaking, similar to observations made by Bonmarin (1989) for two-dimensional waves. A smaller change in

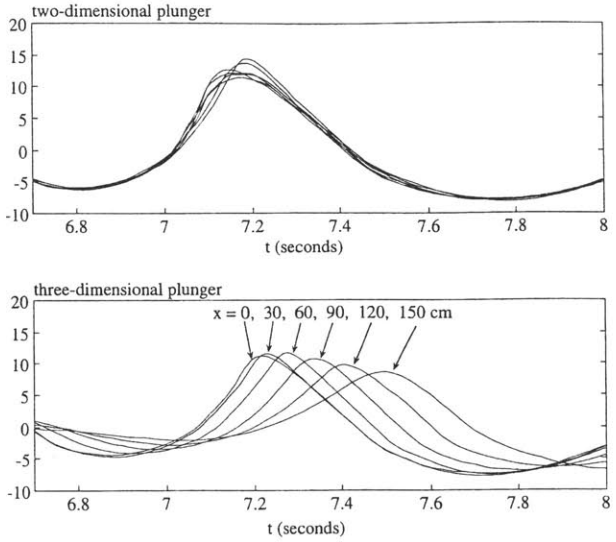

FIG. 6a. The two-dimensional plunger breaks evenly across the channel, with all lateral positions observing a plunging breaker. In contrast the three-dimensional plunger breaks in a crescent shape, with the centerline leading. In addition, the three-dimensional crest is a composite of breaking intensity. At x = 0, 30, and 60 cm the wave is plunging; at x = 90 cm the wave is spilling; x = 120 cm marks the edge of the breaking regions; and the wave is not breaking at x = 150.

group velocity is expected, however, as only the central crest was downshifted.

Finally, normalizing by values at the upstream position y_1 = 0 m, denoted by subscript "0," the fractional change in wave energy flux may be given as

$$\Delta F/F_0 = \Delta(\overline{\eta^2})/\overline{\eta_0^2}, \tag{10}$$

remembering that the terms in (10) represent cross-sectional averages based on the measurements from 11 lateral grid positions. While (10) is not generally valid close to the point of breaking because the assumptions of energy equipartition and constant group velocity fail there, previous experiments have shown that (10) does provide a reasonable estimate of flux variation at positions up- and downstream of the breaking point. (Rapp and Melville 1990).

3. Results

a. Breaking criteria based on local wave steepness

With an initial crest length, L_0 = 90 cm, the three-dimensional wave packet produced a crescent-shaped breaking crest 220 cm in length, that is, limited to less than one-half the channel width. The two-dimensional wave packet produced a spatially uniform crest that

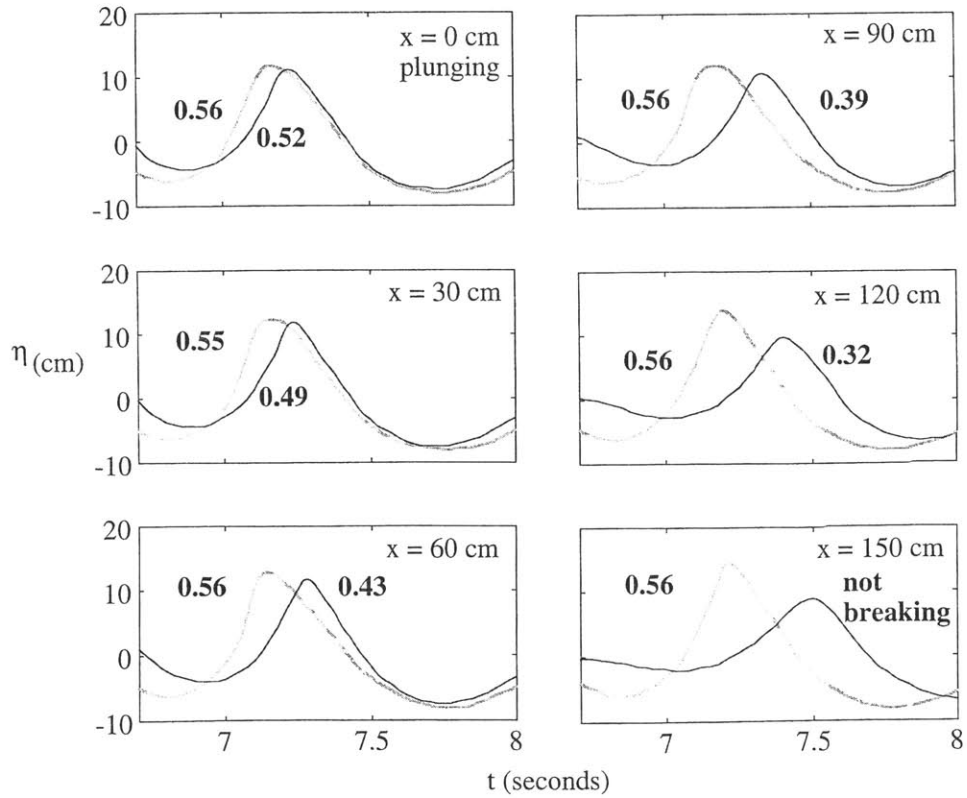

FIG. 6b. Comparison of wave shape at onset of breaking. The black line corresponds to the three-dimensional wave crest and the gray line to the two-dimensional wave crest. The lateral position x of record is given in the upper right of each figure. The values of limiting front-crest steepness are given in bold numerals. By visual inspection the edge of the breaking region for the short-crested wave is x = 120 cm.

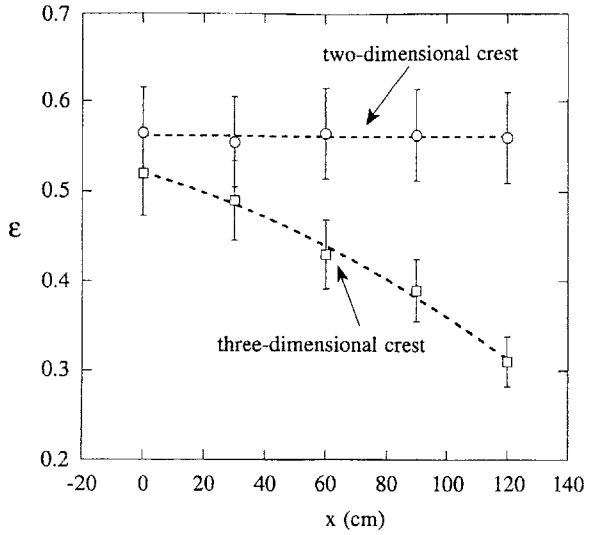

FIG. 7. The crest-front steepness at breaking (see Fig. 5 for definition). The lower steepness as well as the lateral variation in steepness across the three-dimensional breaker suggest the influence of diffraction is to diminish the breaking criteria. Note, for the three-dimensional breaker, x = 120 cm marks the edge of the breaking crest.

broke across the entire channel (Fig. 6a). Consistent with previous observations (Bonmarin 1989; Kjeldsen and Myrhaug 1979), both the two- and three-dimensional crests developed front-to-back asymmetry prior to breaking (Fig. 6b), but both the asymmetry and the crest front steepness were greater for the two-dimensional crest, which broke at a steepness $\varepsilon = 0.56$. In contrast, $\varepsilon = 0.52$ at the centerline of the three-dimensional crest and diminished monotonically to $\varepsilon = 0.32$ moving away from the centerline (Fig. 7). For the short-crested wave packet spatial tapering of the input signal created lateral gradients in crest amplitude and thus diffraction. The laterally diminishing breaking steepness was attributed to the influence of diffraction. Complementary to these observations, spatial focusing of wave energy has been observed to increase local breaking steepness. She et al. (1994) examined energy focusing angles from zero, a two-dimensional wave, to 90 degrees and found that the crest front steepness increased monotonically across this range from $\varepsilon = 0.51$ to $\varepsilon = 1.02$. Combining the observations of both studies documents a consistent relationship between breaking steepness and wave field directionality, that is, over a range of conditions spanning negative focusing (diffraction) through zero angle of focus (two-dimensional wave crest) to strongly positive focusing, local steepness at breaking monotonically increases.

We now consider how these observations fit into the paradigm of wave breaking based on crest particle velocity. In the superposition of two, single-frequency, wave trains, that is, crossed waves, the ratio of crest particle velocity to phase velocity is diminished relative to a planar wave of comparable wave amplitude for any angle of crossing (Le Mehaute 1986). This suggests that breaking height should increase as the angle of wave crossing increases. This tendency was confirmed by the experiments of Kolaini and Tulin (1995). In addition, the observations of She et al. (1994) suggest that this result may be extended to focusing wave fields comprised of both multiple interaction angles as well as multiple frequencies. The observations made in the present study, that is, diminished breaking steepness with increasing diffraction, suggest that within diffracting wave packets the ratio of crest particle velocity to phase velocity is increased. To the authors knowledge, no analytical results exist to support this interpretation.

It is also instructive to note the relative timing of breaking onset along the breaking crest. For the two-dimensional breaking condition, breaking was initiated synchronously along the crest. In contrast, along the crescent-shaped crest of the three-dimensional wave, breaking was initiated at the centerline first, and propagated outward, consistent with observations of breaking made in the field. This sequence of breaking, that is, initiation at the centerline and propagation outward, could suggest that breaking at the centerline provokes breaking away from the centerline at less than critical steepness, perhaps through the introduction of turbulence and/or surface instabilities. Consistent with this, previous studies have noted that the steepness required for breaking was lowered by the presence of turbulence left by preceding breaking events (Ramberg and Griffin 1987; Kolaini and Tulin 1995). This suggests that oceanic turbulence generated by wind may encourage breaking below critical conditions described by theory or observed in pristine tank experiments. In addition, once breaking begins the breaking criteria may shift to allow continued breaking at lower steepnesses.

Finally, the steepness values observed along the three-dimensional wave crest fall within the range of steepnesses observed in the field, ε = [0.32 to 0.78] (Kjeldsen and Myrhaug 1979), suggesting that field variability may be attributed to variability along individual wave crests. In addition, if one includes the steepness values observed under conditions of wave focusing ε = [0.51–1.02], from She et al. (1994) and Kolaini and Tulin (1995), the entire range of field variability may be attributed to wave directionality. In fact, the dependence on wave directionality may explain why single point characterizations of wave shape have not been able to provide stable limits for oceanic wave breaking.

b. Spectrum-based wave steepness

The spectrum-based definition of steepness, ak_c, more broadly reflects the spectral content of the wave field. Based on experiments in a wave channel, that is, for two-dimensional wave crests, ak_c proved to be a robust predictor of three distinct breaking conditions: ak_c = 0.25 (incipient), =0.30 (spiller), and =0.39 (plunger)

(Rapp and Melville 1990). For the two-dimensional wave packets considered in this study the following limits were observed: $ak_c = 0.32$ (incipient), 0.38 (spiller), and 0.50 (plunger). The difference in transition criteria observed here and in Rapp and Melville (1990) is attributed to differences in spectral shape, that is, constant component steepness versus constant component amplitude, respectively. The former spectrum is weighted more heavily at the low-frequency end of the frequency band. Chaplin (1996) also considered both of these spectral forms and found an incipient breaking criteria of $ak_c = 0.26$ and 0.30, for the constant amplitude and constant steepness spectra, respectively. Despite a slightly larger bandwidth, $\Delta f/f_c = 0.83$, the upward shift in breaking criteria with increasing weight on lower-frequency components is consistent with the observations made here.

The shift in breaking criteria cannot be attributed to changes in total wave energy. Assuming the same characteristic steepness, the spectral shape $a_n \sim k_n^{-1}$ contains greater total energy than the spectral shape $a_n = \text{const}$. Thus, based on total energy considerations one would expect the constant ak spectra to produce breaking at a lower value of ak_c, but the opposite is true, suggesting that the distribution of spectral energy plays a significant role in defining the breaking point. In particular, observations presented here and by Chaplin (1996) suggest that wave fields consisting of a relatively greater contribution of low-frequency energy are more stable, that is, have higher threshold for breaking. This suggests that the breaking criteria in the field may shift as the wave-field spectrum develops under changing wind conditions.

The breaking criteria also differed between two- and three-dimensional wave packets of the same spectral shape, $a_n \sim 1/k_n$. Note that for the three-dimensional packets the spectral steepness was defined based on the component amplitudes at the centerline. For the short-crested wave packet the transition to each breaking regime occurred at a higher value of ak_c: 0.35 (incipient), 0.39 (spiller), and 0.54 (plunger). The upshift in transition criteria relative to the spectrally similar, two-dimensional packets was attributed to diffraction, which drains energy from the centerline of the short-crested packet even as it evolves to the point of breaking.

The influence of diffraction on the breaking steepness ak_c was explored by varying the parameter y_b/L_0 (Fig. 8). Note that the impact of diffraction on crest development increases with increasing y_b/L_0. For a two-dimensional wave $L_0 \to \infty$ and $y_b/L_0 = 0$ for all values of y_b, suggesting that the evolution of two-dimensional packets are insensitive to y_b. This was demonstrated by Rapp and Melville (1990) who showed that breaking onset as well as energy loss were insensitive to changes in y_b (x_b in RM). A similar result was found here; that is, breaking onset as described by ak_c was independent of y_b for two-dimensional crests.

For the short-crested breakers, the incipient breaking criteria increased monotonically with increasing y_b/L_0 (Fig. 8). An identical trend was observed for the spilling and plunging criteria as well. These observations demonstrate how strongly the global breaking criteria ak_c is influenced by diffraction. Since the global parameter, ak_c, reflects the total energy within the wave spectrum, these observations suggest that more wave energy is needed within a diverging wave field in order to initiate breaking; the corollary of which is that breaking may be suppressed if a wave field is diverging strongly enough. By extrapolation, breaking is encourage in a focused wave field. Because of the strong influence of directionality on breaking criteria, one should use caution when extrapolating two-dimensional laboratory results to three-dimensional wave fields.

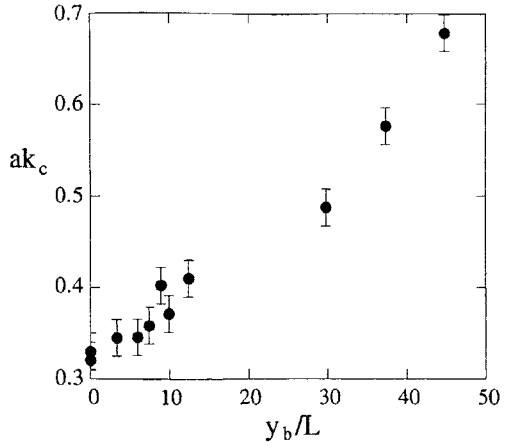

FIG. 8. A breaking criteria based on global steepness, ak_c, increases as the influence of diffraction increases, y_b/L_0. The experiments considered a range of conditions: L_0 = (30, 60, and 90 cm) and y_b = (4, 5, 6). Identical trends in steepness were observed for the onset criteria of spilling and plunging.

c. *Spectral evolution*

As the wave crest approached breaking, the wave profile became sharper and more asymmetric. These changes are reflected in the surface displacement spectra by the appearance of higher harmonics (Tulin and Li 1992). Figures 9, 10, and 11 compare the spectral evolution along the centerline of a short-crested (3D) incipient and plunging wave, and a two-dimensional plunging wave, respectively. The frequency f[Hz] is normalized by the central frequency f_c of the input spectra, and the spectral density $S_{\eta\eta}$ [cm^2 s] is normalized by $k_c^2 f_c$. In each graph the solid line represents the spectrum measured at $y = 0$. The dashed lines represent the spectrum at two downstream positions, $y = 80$ cm ($yk_c = 3.8$) in panels a and $y = 180$ cm ($yk_c = 8.5$) in panels b. The points $y = 80$ and 180 cm are chosen because they depict the most extreme shifts in energy relative to the initial condition. Although the surface displacement at $y = 80$ and 180 cm were measured during separate runs, Fig. 4 confirms that the wave condition,

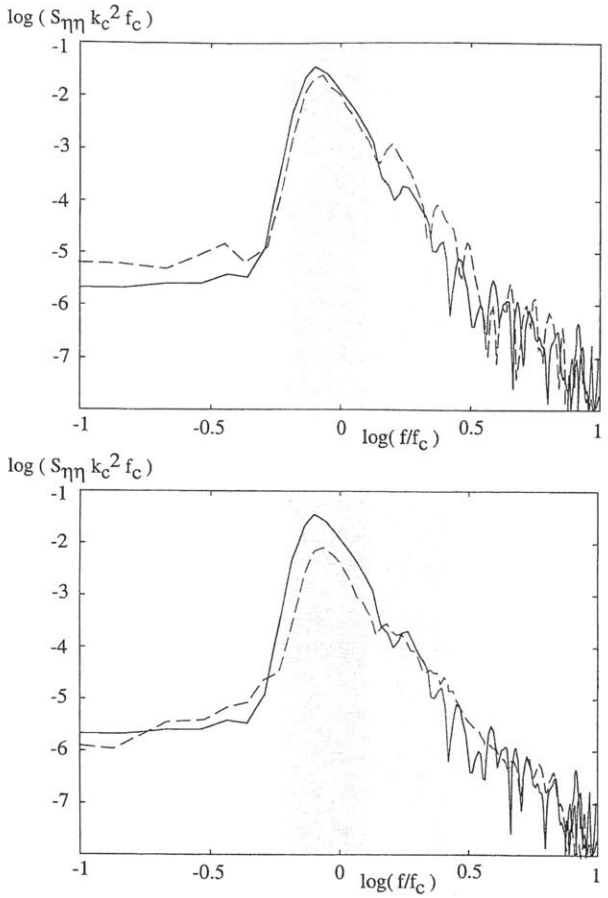

FIG. 9. Surface displacement spectra measured at the centerline of the short-crested, incipient wave packet. In each graph the solid line represents the spectrum measured at y = 0. The dashed lines represent the spectrum at (a: top) y = 80 cm, and (b: bottom) y = 180 cm. The principal and second harmonic bands are shaded in dark and light gray, respectively. The 95% confidence interval for the spectral estimates is equal to 1/2 unit (1/2 decade) on the left axis.

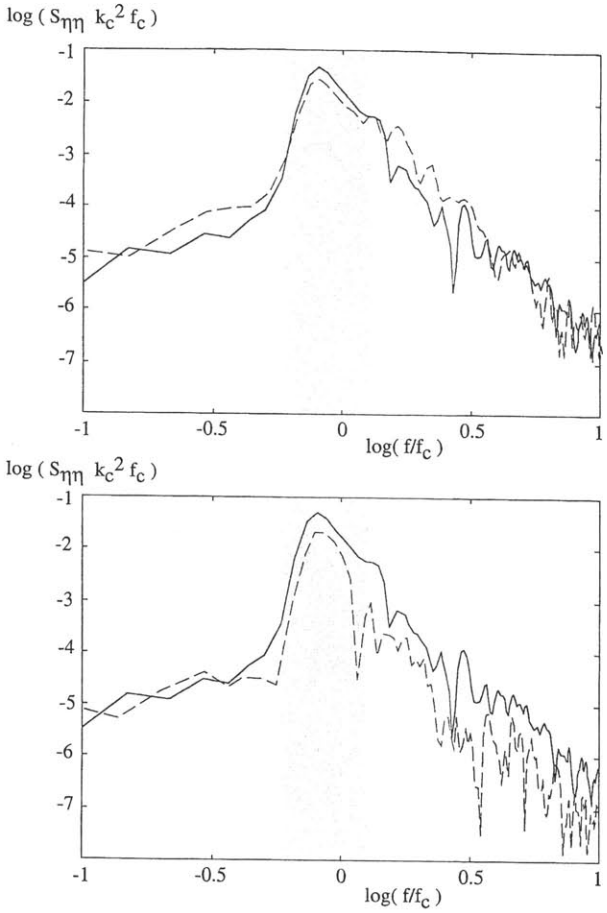

FIG. 10. Same as in Fig. 9 but for the short-crested plunging wave.

as recorded at the reference wave gauge, was identical. Finally, the input and higher frequency bands are shaded in dark and light gray, respectively.

The short-crested incipient wave spectra demonstrates the signature of intrawave energy transfer. Between y = 0 cm and y = 80 cm, the spectral energy within the higher frequency band increases (Fig. 9a) at the expense of the first harmonic band. Similar up-frequency shifts have been observed for focusing wave packets of different spectral shape (Rapp and Melville 1990; She et al. 1994). In addition, the up-frequency energy transfer, associated with the emergence of nonlinear behavior has been explored theoretically and numerically for unifrequency wave trains by McLean (1982). Thus, a similar signature has been observed for four different spectral shapes including both two-dimensional and, in this study, three-dimensional wave evolution.

Beyond the focusing point the energy content of the second frequency band, E_2, returns to its initial level (Fig. 9b), suggesting that the nonlinear interaction producing the up-frequency shift in energy is completely reversible. The reversibility of nonlinear wave–wave interactions was also noted by Rapp and Melville (1990) and by Baldock et al. (1996) who documented both spatial and temporal wave signal symmetry about a focal point for nonbreaking, two-dimensional wave packets. In contrast to the reversible evolution of E_2, the energy of the first harmonic band is not recovered after the focusing event, but exhibits a monotonic decrease. Since no breaking has occurred the steady loss is attributed to diffraction. Diffraction may also affect E_2 with losses proportional to those in E_1; that is, $\Delta E_2 \sim (ak)^2 \Delta E_1$. Using the spectra steepness, $ak_c = 0.35$, the drop in E_2 attributable to diffraction would be 1%, which represents 50% of the observed change, suggesting that diffraction may be important. However, the cycle of increasing and decreasing energy within the higher harmonic band is the same as that observed for a two-dimensional wave that would not be affected by diffraction (Rapp and Melville 1990; Baldock 1996). Thus, it remains unclear how diffraction and frequency focusing interplay.

The incipient wave spectra also indicates an increase in spectral energy below the peak frequency as the wave

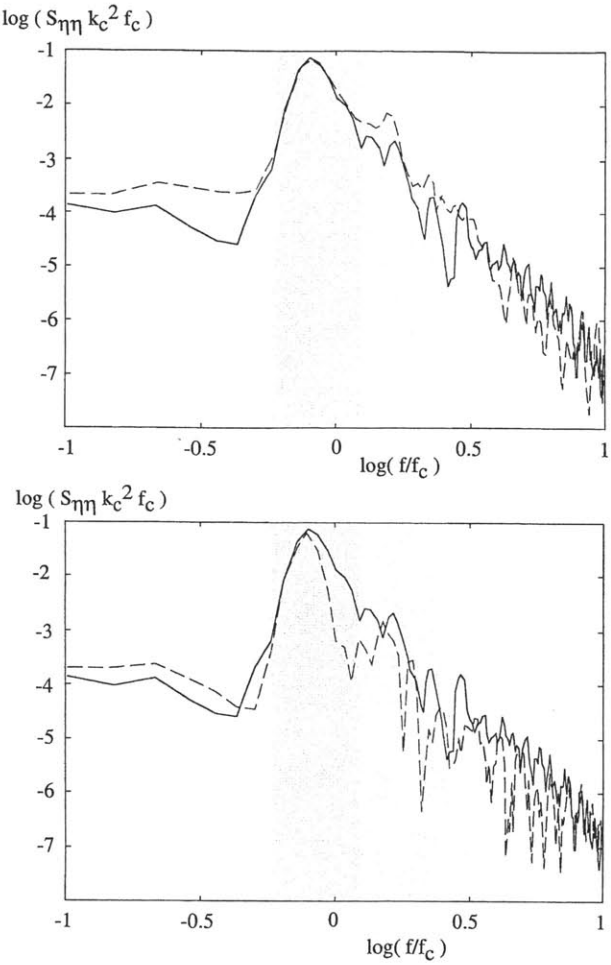

FIG. 11. Same as in Fig. 9 but for the two-dimensional plunging wave.

packet approaches the focal point. This reflects the generation of a forced wave (Fig. 9a). That the low-frequency signature is not apparent at the downstream station (y = 180 cm, Fig. 9b) indicated that the forced wave does not leave the test section within the time considered. A similar evolution was observed for two-dimensional incipient waves (Rapp and Melville 1990).

Up to the point of breaking the short-crested plunger evolves in parallel with the incipient wave packet (Figs. 9a and 10a). Specifically, E_2 increases while E_1 is diminished due to diffraction and up-frequency transfer. Growth of the forced wave is also weakly apparent in the lower frequencies. Beyond the focal point the plunger and incipient spectra diverge, with the plunger losing energy from both the first and second frequency bands. As with the incipient wave there is no expression of long wave or mean current energy in the low frequencies at the downstream station (Fig. 10b). This provides additional support for the assumption that within the time interval considered for analysis, mean currents generated by the breaking event do not pass the end of the test section.

To decipher the distribution of losses further, we consider the two-dimensional plunger. The two-dimensional plunger displays the same evolution in E_2, that is, an increase in energy density approaching the point of breaking and subsequent loss of this energy in the process of breaking (Fig. 11). The losses appear in the higher-frequency end of the first frequency band and in the second frequency band. Despite differences in the initial spectral shape, a similar distribution of breaking losses was reported in Rapp and Melville (1990), that is, breaking losses were taken from the higher-frequency end of the spectrum. Within the principle frequency band no losses occur below the peak frequency for the two-dimensional plunger (Fig. 11a). Comparison of the long- and short-crested plungers then suggests that losses below the peak frequency observed in the short-crested wave packet were due to diffraction alone.

The above observations document the signature of frequency focusing and breaking within the evolving surface displacement spectra. Of most interest is the evolution of E_2, which displays nearly identical signatures for both two- and three-dimensional waves. This can be more clearly demonstrated by isolating the evolution of E_2. Figure 12 depicts this evolution at three lateral positions (x = 0, 30, and 60 cm) and for conditions of incipient breaking, spilling, short-crested plunging, and two-dimensional plunging. The abscissa depicts the entire test section length, which includes two focal points, yk_c = 3.8 and yk_c = 10.2, at which the plunger and spiller occurred, respectively. As described previously, within a given wave packet the plunging breaker occurred one wave crest upstream of where the spilling breaker occurred under weaker wave conditions.

The incipient wave condition clearly reflects the two focusing positions. At each focusing position there is an increase in the second frequency band as the wave packet focuses and a subsequent decrease as the wave packet disperses. After each focusing event the energy of the higher-frequency band returns to its initial value, indicating periodic variation but no net loss. This pattern is repeated at each lateral position.

The spilling wave packet passes through the first focusing point (yk_c = 3.8) as an incipient wave, and then breaks (spilling) at the second focal point. This evolution is reflected in E_2. At the first focal point the wave spectra evolves in parallel to the incipient wave discussed above, whereas at the second focal point a net loss of energy results from the breaking. The net loss of energy diminishes moving away from the centerline, in particular between gauges 2 and 3 positioned at x = 30 and 60 cm, respectively.

The two- and three-dimensional plunging breakers are identical at both gauges 1 and 2, where the short-crested breaker was strongly plunging. In both cases the evolution of E_2 follows the incipient case up to the first focusing peak and then drops sharply, indicating the

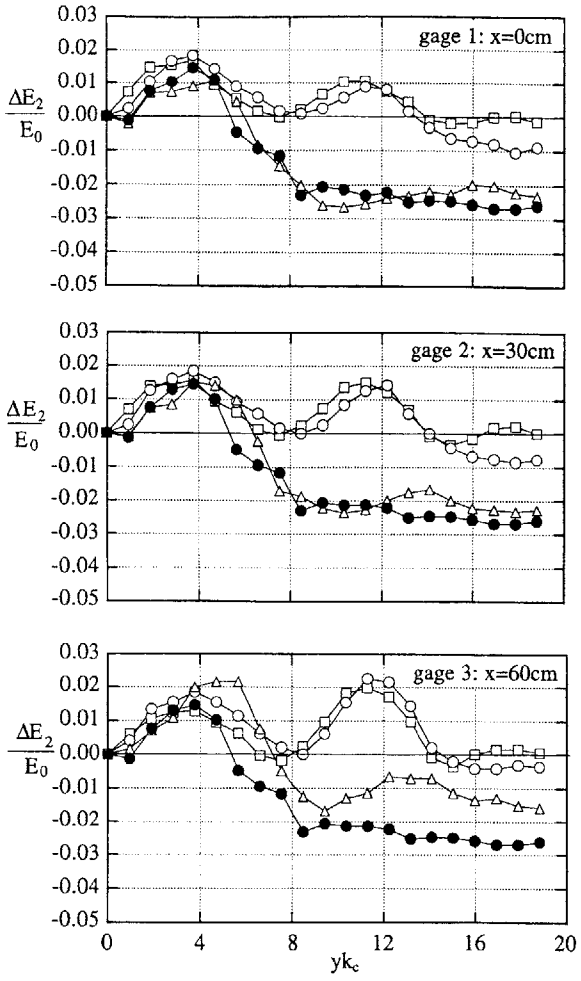

FIG. 12. Evolution of the second harmonic band for a short-crested incipient wave (open squares); a short-crested spilling wave (open circles); a short-crested plunging wave (open triangles); and a two-dimensional plunging wave (closed circles). The three graphs represent observations made at the centerline (a); x = 30 cm (b); and x = 60 cm (c). Here ΔE_2 represents the change in energy contained in the second harmonic frequency band; E_0 is the total initial wave energy within the wave packet.

breaking losses. At gauge 3 the breaking loss observed for the short-crested breaker is diminished relative to the laterally uniform breaker. This reflects the lateral variation in breaking intensity across the three-dimensional crest. Moving away from the centerline, losses from the three-dimensional plunger diminish and the signature evolves from a plunging wave (x = 0, 30 cm), to a spilling wave (x = 90 cm), and finally to a nonbreaking, incipient wave (x = 120 cm) (Fig. 13). The transitions between wave types suggested by the differences in E_2 evolution are consistent with photographic observations, an example of which is shown in Fig. 14. This suggests that higher harmonic evolution will provide a more robust indicator of breaking that is not influenced by wave directionality, as are both ε and ak_c. Finally, note that even when breaking occurs at the first

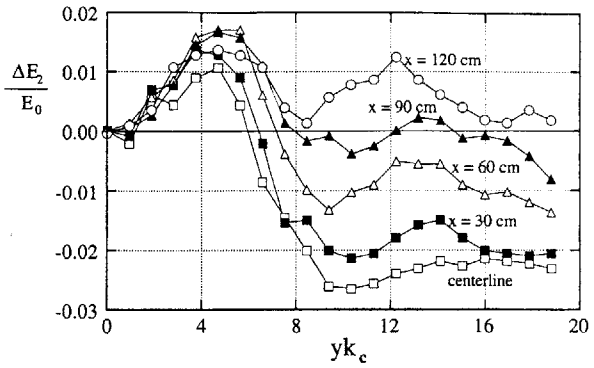

FIG. 13. Evolution of the second harmonic band for the short-crested plunging wave packet. Variation across the wave crest is captured by five lateral positions: (open squares) centerline, (closed squares) x = 30 cm, (open triangles) x = 60 cm, (closed triangles) x = 90 cm, and (open circles) x = 120 cm.

focal point, the second focal point is expressed in E_2. However, the second focus becomes less distinct and is shifted farther downstream as the breaking intensity increases, that is, closer to the centerline of the breaker (Fig. 13). These shifts suggest that the breaking event alters the subsequent wave evolution.

d. *Energy loss*

Following the procedure described in section 2e, the breaking losses is computed from the longitudinal variation in $\overline{\eta^2}$ (Fig. 15). In contrast to section 3c, $\overline{\eta^2}$ is now evaluated in a lateral averaged sense to eliminate the local effects of diffraction. The incipient wave indicates a nearly steady decline in wave energy (dashed) that results in a total loss of 6%, attributable to boundary layer losses (Fig. 15a). The predicted frictional loss (dot-dashed) for a laminar boundary layers is 3.6% (Hunt 1952). That the actual loss exceeds the predicted value is attributed to errors associated with the lateral integration of wave energy and with the neglect of higher-order terms.

The variance of both breaking waves follows the same decay up to yk_c = 2.8. At this point, about one-half wavelength upstream of breaking onset, the variance begins a steady decline, reflecting the conversion of wave potential energy to wave kinetic energy as the wave steepens (Rapp and Melville 1990). When the wave breaks this energy is lost and the variance does not return to the prebreaking value. The temporary rise in variance observed near yk_c = 12 reflects an oscillation in carrier wave steepness arising from wave packet evolution that affects the ratio of kinetic and potential energy. Similar oscillations were observed by Rapp and Melville (1990) in the postbreaking evolution of a two-dimensional wave packet. Within two carrier wavelengths the wave packet variance settles back to a nearly constant but reduced level.

Using the incipient case to delimit frictional losses,

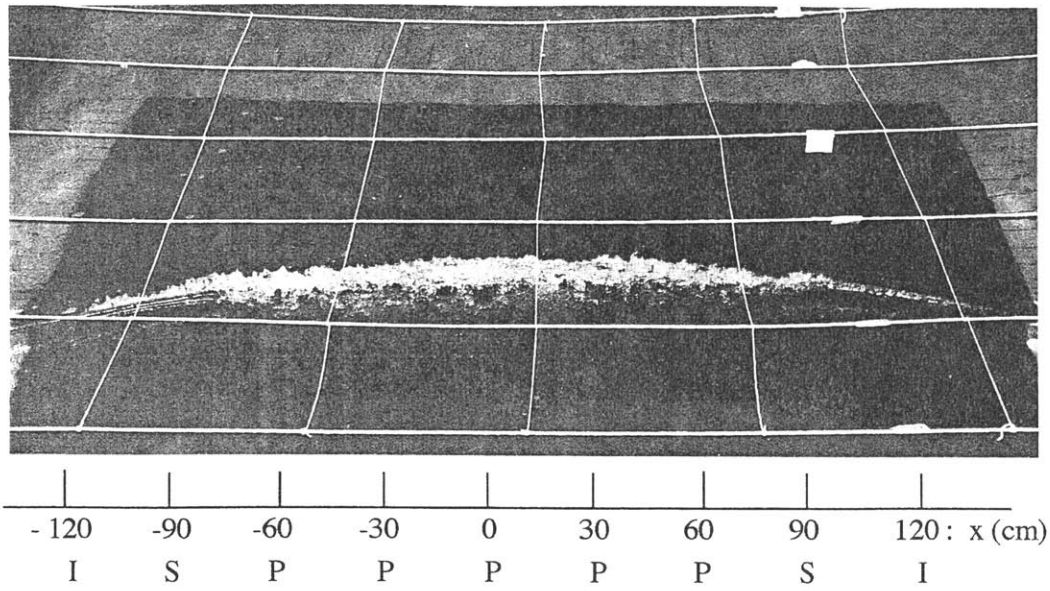

FIG. 14. Photograph of the breaking crest taken from behind the wave; that is, the crest is moving away from the camera. The rope grid (white lines) is positioned 30 cm above the still water surface and is used to determine the wave position and dimensions. The grid boxes are 50 cm × 50 cm. Because of limitations in positioning the camera, the line of sight is offset from the centerline. Using geometry to correct for parallax, the lateral position along the crest line are indicated across the bottom of the image.

the loss due to breaking alone may be estimated as the difference between the breaking and incipient cases (Fig. 15b). The two-dimensional plunger, $ak_c = 0.50$, loses 22 ± 1% of its initial energy to breaking. For a slightly higher steepness, $ak_c = 0.54$, the three-dimensional plunger incurs a laterally averaged loss of 10 ± 1%. This value, however, underestimates the intensity of the short-crested breaker because the lateral average includes crest length that is not breaking. A better comparison is made if the loss due to breaking is normalized only by the energy contained in the breaking crest at the onset to breaking. For the two-dimensional plunger the energy in the crest just prior to breaking is the same as the input energy, excluding viscous losses, and the breaking crest spans the entire test section, so the fractional loss reported above is appropriate. For the three-dimensional plunger the breaking crest is 2.2 ± 0.2 m, including the plunging and spilling regions, based on photographs and the evolution of higher-frequency energy E_2 (Fig. 13). Using the wave energy recorded at $y = 80$ cm to define the energy available in the breaking crest at the onset to breaking, the fractional loss of crest energy during breaking is 16 ± 1%. A smaller loss associated with the three-dimensional plunger is attributed to the fact that the breaking crest includes both plunging and spilling sections. Consistent with this, a 16% loss falls between the losses associated with two-dimensional spilling (10%) and plunging (25%) observed by Rapp and Melville (1990). The trend toward diminished breaking steepness (§3a) along with the diminished breaking severity with decreasing wave focus (conditions of diffraction) complements the observation of increasing breaking steepness and severity with increasing wave focus (She et al. 1994). These observations point out the importance of wave directionality in determining both the onset and severity of breaking events.

4. Summary

Combining observations from the present study with those of She et al. (1994) and Kolaini and Tulin (1995), we confirm that wave directionality affects both the onset and severity of breaking events. As wave directionality varies from negative focusing (diffraction) through planar wave crests to positive focusing, both the breaking crest-front steepness and the breaking severity increase monotonically. In addition, the range of limiting steepness ε observed between conditions of focusing and diffraction cover the range of observations made in the field (Kjeldsen and Myrhaug 1979), suggesting that field variability may be attributed to wave directionality.

The global, spectrum-based wave steepness ak_c is more robust than local wave shape parameters, but is also sensitive to wave-field directionality. In this study the limiting value for ak_c increased by a factor of 2 over a parameter range of $y_b/L_0 = 0$ to 50. While it is difficult to translate the experimental parameter, y_b/L_0, into a field parameter, the trend clearly suggests that ak_c will increase steadily with increasing angle of wave field divergence and that the onset of breaking may be delayed or even suppressed within a diverging wave field.

Finally, within the range of conditions considered in the present study, the effect of wave diffraction was

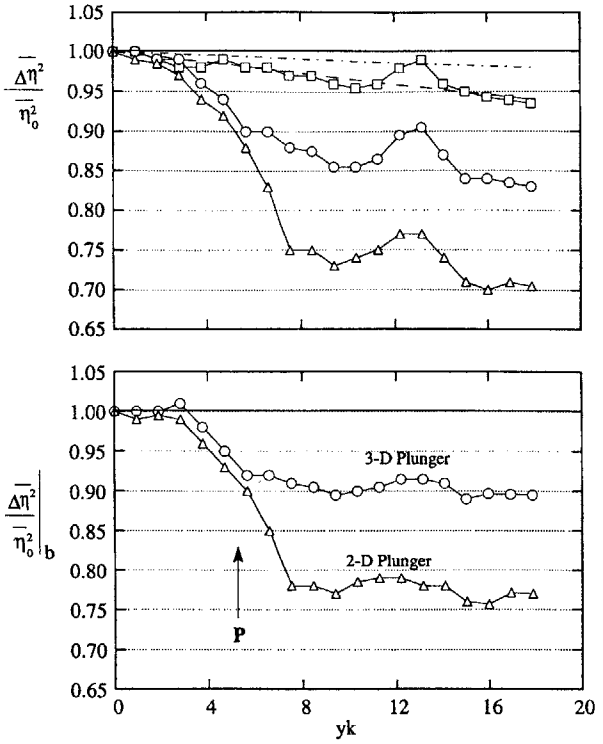

FIG. 15. (a: top) Longitudinal variation in laterally averaged wave packet energy. The lateral average is applied to eliminate the local effects of diffraction. The incipient wave (squares) indicates a nearly steady decline (dashed) that results in a total loss of 6%. The predicted boundary layer loss (dot-dashed) is 2.6%. The short-crested plunger (circles) and two-dimensional plunger (triangles) are also depicted. (b: bottom) Using the incipient case to characterize frictional losses, the loss due to breaking alone may be computed as the difference between the breaking and incipient cases. The resulting variation in wave energy for both the short-crested (circles) and two-dimensional plunger (triangles) is plotted.

only manifest strongly within the principal harmonics, such that the evolution of the higher harmonic bands were identical for two- and three-dimensional waves. In particular, an up-frequency energy shift marked the emergence of nonlinear behavior as the wave packet began to focus longitudinally. Beyond the focal point the up-frequency transfer was completely reversed, unless the wave broke, in which case the up-shifted energy was lost from the wave field. It is interesting to note that the lowest-frequency components did not contribute to the intrawave energy transfer or to the subsequent loss of wave energy that occurred during breaking. In addition, shifts in the breaking criteria ak_c observed with changes in spectral shape suggest that instability and breaking are promoted when a relatively greater contribution of wave energy resides in the higher frequencies (§3b, and Chaplin 1996). Together, the above observations suggest that the breaking process is largely controlled by the evolution of higher-frequency components. Thus, the evolution of a wave field parallels the evolution of a single-frequency wave train for which the development of higher-frequency components, in the form subwavelength modulations, is a precursor to breaking. The above discussions suggest that a breaking criteria based on the evolution of high-frequency components may be a more robust indicator for field application as it is insensitive to wave-field directionality.

Acknowledgments. Support for this work has been provided by ONR Contract N00014-94-1-0610. We also thank Ziad Zakharia for his assistance with the experimental work, and Ole Madsen and Chiang Mei for their helpful editorial comments.

REFERENCES

Baldock, T., C. Swan, and P. Taylor, 1996: A laboratory study of nonlinear surface waves on water. *Philos. Trans. Roy. Soc. London,* **452A,** 649–676.

Banner, M., and O. M. Phillips, 1974: On the incipient breaking of small scale waves. *J. Fluid Mech.,* **77,** 825–842.

Benjamin, T., and J. Feir, 1967: The disintegration of wave trains in deep water. *J. Fluid Mech.,* **27,** 373–397.

Blanchard, D., and A. Woodcock, 1980: The production, concentration and vertical distribution of the sea-salt aerosol. *Ann. N.Y. Acad. Sci.,* **338,** 330–347.

Bonmarin, P., 1989: Geometric properties of deep water breaking waves. *J. Fluid Mech.,* **209,** 405–433.

Bryan, K., and M. Spelman, 1985: The ocean's response to a CO_2-induced warming. *J. Geophys. Res.,* **90,** 11 678–11 688.

Chan, E. S., and W. K. Melville, 1988: Deep water plunging wave pressure on a vertical plane wall. *Proc. Roy. Soc. London,* **417A,** 95–131.

Chaplin, J., 1996: On frequency-focusing unidirectional waves. *Int. J. Offshore Polar Eng.,* **6,** 131–137.

Csanady, G., 1990: The role of breaking wavelets in air–sea gas transfer. *J. Geophys. Res.,* **95,** 749–759.

Cummins, W., 1962: The impulse–response function and ship motion. *Schiffstechnik Forschungsh. Schiffbau Schiffsmaschineubau,* **9,** 101–109.

Davis, M., and E. Zarnick, 1964: Testing ship models in transient waves. *Proc. Fifth Symp. on Naval Hydrodynamics,* Washington, DC, Office of Naval Research, 509–540.

Dawson, T H., D. L. Kriebel, and L. A. Wallendorf, 1993: Breaking waves in laboratory-generated JONSWAP seas. *Appl. Ocean Res.,* **13,** 85–93.

Dean, R., and R. Dalrymple, 1984: *Water Wave Mechanics for Engineers and Scientists.* Prentice-Hall, 174–175.

Duncan, J., 1981: An experimental investigation of breaking waves produced by a towed hydrofoil. *Proc. Roy. Soc. London,* **377A,** 331–348.

——, 1983: The breaking and non-breaking wave resistance of a two-dimensional hydrofoil. *J. Fluid Mech.,* **126,** 507–520.

Gargett, A., 1989: Ocean turbulence. *Annu. Rev. Fluid Mech.* **21,** 419–451.

Greenhow, M., and T. Vinje, 1982: A theoretical and experimental study of the capsize of Salter's Duck in extreme waves. *J. Fluid Mech.,* **118,** 221–239.

Havelock, T., 1918: Periodic, irrotational waves of finite height. *Proc. Roy. Soc. London,* **95A,** 38–56.

Hunt, J., 1952: Viscous damping of waves over an inclined bed in a channel of finite width. *Houille Blanche,* **6,** p. 836.

Johnson, B., and R. Cooke, 1979: Bubble populations and spectra in coastal waters: A photographic approach. *J. Geophys. Res.,* **84,** 3761–3766.

Kjeldsen, S. P., and D. Myrhaug, 1980: Wave–wave interactions, current–wave interactions and resulting extreme waves and breaking waves. *Proc. 17th Conf. on Coastal Engineering,* ASCE, Sydney Australia, 2277–2303.

Koga, M., 1982: Bubble entrainment in breaking wind waves. *Tellus,* **34,** 481–498.

Kolaini, A., and M. Tulin, 1995: Laboratory measurements of breaking inception and postbreaking dynamics of steep short-crested waves. *Int. J. Offshore Polar Eng.,* **5,** 212–218.

Le Mehaute, B., 1986: On the highest periodic short-crested wave. *J. Waterway, Port, Coastal Ocean Eng.,* **112,** 320–330.

Loewen, M. R., and W. K. Melville, 1991: Microwave backscatter and acoustic radiation from breaking waves. *J. Fluid Mech.,* **224,** 601–623.

Longuet-Higgins, M. S., 1969: On wave breaking and equilibrium spectrum of wind. *Proc. Roy. Soc. London,* **310A,** 151–159.

——, 1985a: Bifurcation in gravity waves. *J. Fluid Mech.,* **151,** 457–475.

——, 1985b: Accelaration in steep gravity waves. *J. Phys. Oceanogr.,* **15,** 1570–1579.

——, 1986: Eulerian and Lagrangian aspects of surface waves *J. Fluid Mech.,* **173,** 683–707.

McLean, J., 1982: Instabilities of finite-amplitude gravity waves. *J. Fluid Mech.,* **114,** 315–330.

Mei, C. C., 1983: *The Applied Dynamics of Ocean Surface Waves.* Wiley, 387–390.

Melville, W. K., 1982: The instability and breaking of deep-water waves. *J. Fluid Mech.,* **115,** 163–185.

——, 1996: Wave breaking in air–sea interaction. *Annu. Rev. Fluid Mech.,* **28,** 279–321.

——, and R. J. Rapp, 1988: The surface velocity field in steep and breaking waves. *J. Fluid Mech.,* **189,** 1–22.

Michell, J. H., 1893: On the highest waves in water. *Philos. Mag., Ser. 5,* **365,** 430–437.

Mitsuyasu, H., 1985: A note on the momentum transfer from wind waves. *J. Geophys. Res.,* **90,** 3343–3345.

Myrhaug, D., and E. Dahle, 1994: Ship capsize in breaking waves. *Fluid Structure Interaction in Offshore Engineering,* J. K. Chakrabarti, Ed., Computational Mechanics Publication, 43–84.

Ochi, M. K., and C. H. Tasi, 1983: Prediction of occurrence of breaking waves in deep water. *J. Phys. Oceanogr.,* **13,** 1482–1492.

Penney, W., and A. Price, 1952: Part II. Finite periodic stationary gravity waves in a perfect liquid. *Philos. Trans. Roy. Soc. London,* **244A,** 254–284.

Phillips, O. M., 1958: The equilibrium range in spectrum of wind-generated wave. *J. Fluid Mech.,* **4,** 89–99.

——, 1977: *The Dynamics of the Upper Ocean.* Cambridge University Press, 3–4.

Ramberg, S. E., and O. M. Griffin, 1987: Laboratory study of steep and breaking deep water waves. *J. Waterway, Port, Coastal Ocean Eng.,* **113,** 493–507.

Rapp, R. J., and W. K. Melville, 1990: Laboratory measurements of deep water breaking waves. *Philos. Trans. Roy. Soc. London,* **331A,** 735–780.

Rosengaus-Moshinsky, M., 1987: Experimental study of wave-generated bedforms and resulting wave attenuation. Ph.D. thesis, Massachusetts Institute of Technology, 71–94.

She, K., C. Greated, and W. Easson, 1994: Experimental study of three-dimensional wave breaking. *J. Waterway, Port, Coastal Ocean Eng.,* **120,** 20–36.

Snyder, R., L. Smith, and R. Kennedy, 1983: On the formation of whitecaps by a threshold mechanism. Part III: Field experiment and comparison with theory. *J. Phys. Oceanogr.,* **13,** 1505–1518.

Stokes, G., 1880: Supplement to a paper on the theory of oscillatory waves. *Math. Phys. Papers,* **1,** 314–326.

Su, M. Y., 1982: Three-dimensional deep-water waves, Part 1: Experimental measurements of skew and symmetric wave pattern. *J. Fluid Mech.,* **124,** 73–108.

——, and A. Green, 1985: Wave breaking and nonlinear instability coupling. *The Ocean Surface: Wave Breaking, Turbulent Mixing, and Radio Probing,* Y. Toba and H. Mitsuyasu, Eds., Kluwer Academic, 31–38.

——, M. Bergin, P. Marler, and R. Myrick, 1982: Experiment on nonlinear instabilities and evolution of steep gravity-wave trains. *J. Fluid Mech.,* **124,** 45–72.

Taylor, G. I., 1953: An experimental study of standing wave. *Proc. Roy. Soc. London,* **218A,** 44–59.

Thorpe, S., 1993: Energy loss by breaking waves. *J. Phys. Oceanogr.,* **23,** 2498–2502.

——, 1995: Dynamical process of transfer at the sea surface. *Progress in Oceanography,* Vol. 35, Pergamon, 315–352.

Tulin, M. P., and J. Li, 1992: On the breaking of energetic waves. *Int. J. Offshore Polar Eng.* **2,** 46–53.